









Review

Linking Remote Sensing and Geodiversity and Their Traits Relevant to Biodiversity—Part I: Soil Characteristics

Angela Lausch ^{1,2,*} , Jussi Baade ³ , Lutz Bannehr ⁴, Erik Borg ^{5,6}, Jan Bumberger ⁷, Sabine Chabrilliat ⁸ , Peter Dietrich ⁷, Heike Gerighausen ⁹, Cornelia Glässer ¹⁰, Jorg M. Hacker ¹¹, Dagmar Haase ^{1,2} , Thomas Jagdhuber ¹² , Sven Jany ¹³, András Jung ¹⁴ , Arnon Karnieli ¹⁵ , Roland Kraemer ² , Mohsen Makki ², Christian Mielke ⁸, Markus Möller ¹⁶ , Hannes Mollenhauer ⁷, Carsten Montzka ¹⁷ , Marion Pause ¹⁸ , Christian Rogass ⁸, Offer Rozenstein ¹⁹, Christiane Schmullius ³, Franziska Schrodtt ²⁰, Martin Schrön ⁷ , Karsten Schulz ²¹ , Claudia Schütze ²², Christian Schweitzer ²³, Peter Selsam ⁷, Andrew K. Skidmore ^{24,25} , Daniel Spengler ⁸ , Christian Thiel ²⁶ , Sina C. Truckenbrodt ^{3,26} , Michael Vohland ²⁷ , Robert Wagner ²⁸ , Ute Weber ²², Ulrike Werban ⁷ , Ute Wollschläger ²⁹, Steffen Zacharias ⁷ , and Michael E. Schaepman ³⁰ 

- ¹ Department Computational Landscape Ecology, Helmholtz Centre for Environmental Research–UFZ, Permoserstr. 15, D-04318 Leipzig, Germany; dagmar.haase@geo.hu-berlin.de
- ² Geography Department, Humboldt University Berlin, Unter den Linden 6, D-10099 Berlin, Germany; roland.kraemer@geo.hu-berlin.de (R.K.); makki@hu-berlin.de (M.M.)
- ³ Institut of Geography, Department of Remote Sensing, Friedrich Schiller University Jena, Loebdergraben 32, D-07743 Jena, Germany; jussi.baade@uni-jena.de (J.B.); c.schmullius@uni-jena.de (C.S.); sina.truckenbrodt@uni-jena.de (S.C.T.)
- ⁴ Department of Architecture, Facility Management and Geoinformation, Institut for Geoinformation and Surveying, Bauhausstraße 8, D-06846 Dessau, Germany; l.bannehr@afg.hs-anhalt.de
- ⁵ German Aerospace Center-DLR, German Remote Sensing Data Center–DFD, Kalkhorstweg 53, D-17235 Neustrelitz, Germany; erik.borg@dlr.de
- ⁶ University of Applied Sciences Neubrandenburg, Brodaer Strasse 2, D-17033 Neubrandenburg, Germany
- ⁷ Department Monitoring and Exploration Technology, Helmholtz Centre for Environmental Research–UFZ, Permoserstr. 15, D-04318 Leipzig, Germany; jan.bumberger@ufz.de (J.B.); peter.dietrich@ufz.de (P.D.); hannes.mollenhauer@ufz.de (H.M.); martin.schroen@ufz.de (M.S.); peter.selsam@ufz.de (P.S.); ulrike.werban@ufz.de (U.W.); steffen.zacharias@ufz.de (S.Z.)
- ⁸ Helmholtz Center Potsdam, German Research Center for Geosciences, Telegrafenberg, D-14473 Potsdam, Germany; chabri@gfz-potsdam.de (S.C.); christian.mielke@gfz-potsdam.de (C.M.); rogass@gfz-potsdam.de (C.R.); daniel.spengler@gfz-potsdam.de (D.S.)
- ⁹ Federal Research Centre for Cultivated Plants, Institute for Crop and Soil Science, Julius Kühn-Institut (JKI), Bundesallee 69, D-38116 Braunschweig, Germany; heike.gerighausen@julius-kuehn.de
- ¹⁰ Department of Remote Sensing, Martin Luther University Halle-Wittenberg, Von-Seckendorff-Platz 4, D-06120 Halle, Germany; cornelia.glaesser@geo.uni-halle.de
- ¹¹ Airborne Research Australia, Parafield Airport, SA 5106 and Flinders University, College of Science and Engineering, Adelaide, SA 5000, Australia; jorg.hacker@airborneresearch.org.au or jmh@flinders.edu.au
- ¹² German Aerospace Center (DLR) Microwaves and Radar Institute, Oberpfaffenhofen, D-82234 Wessling, Germany; thomas.jagdhuber@dlr.de
- ¹³ MILAN Geoservice GmbH, Zum Tower 4, D-01917 Kamenz, Germany; s.jany@milan-geoservice.de
- ¹⁴ Technical Department, Szent István University, Villányi út 29-43, 1118 Budapest, Hungary; jung.andras@kertk.szie.hu
- ¹⁵ The Remote Sensing Laboratory, Jacob Blaustein Institutes for Desert Research, Ben Gurion University of the Negev, Sede-Boker Campus, Sede Boger 83990, Israel; karnieli@bgu.ac.il
- ¹⁶ Federal Research Centre for Cultivated Plants, Institute for Strategies and Technology Assessment, Julius Kühn Institute (JKI), Stahnsdorfer Damm 81, D-14532 Kleinmachnow, Germany; markus.moeller@julius-kuehn.de
- ¹⁷ Forschungszentrum Jülich GmbH, Institute of Bio- and Geoscience, Agrosphere (IBG-3), Wilhelm-Johnen-Str., D-52428 Jülich, Germany; c.montzka@fz-juelich.de

- ¹⁸ Institut of Photogrammetry and Remote Sensing, Technical University Dresden, Helmholtzstr. 10, D-01061 Dresden, Germany; marion.pause@tu-dresden.de
- ¹⁹ Institute of Soil, Water and Environmental Sciences, Agricultural Research Organization, Volcani Center, HaMaccabim Road, P.O.B 15159, Rishon LeTsiyon 7528809, Israel; offerr@volcani.agri.gov.il
- ²⁰ University of Nottingham, School of Geography, University Park, Nottingham NG7 2RD, UK; franziska.schrodt1@nottingham.ac.uk
- ²¹ Institute for Hydrology and Water Management, University of Natural Resources and Life Sciences, Vienna, Muthgasse 18, 1190 Vienna, Austria; karsten.schulz@boku.ac.at
- ²² Computational Hydrosystems Helmholtz Centre for Environmental Research–UFZ, Permoserstr. 15, D-04318 Leipzig, Germany; claudia.schuetze@ufz.de (C.S.); ute.weber@ufz.de (U.W.)
- ²³ German Environment Agency, Wörlitzer Platz 1, D-06844 Dessau Roßlau, Germany; christian.schweitzer@uba.de
- ²⁴ Faculty of Geo-Information Science and Earth Observation (ITC), University of Twente, P.O. Box 217, AE 7500 Enschede, The Netherlands; a.k.skidmore@utwente.nl
- ²⁵ Department of Earth and Environmental Science, Macquarie University, Sydney, NSW 2109, Australia
- ²⁶ DLR Institute of Data Science, Mälzerstraße 3, D-07743 Jena, Germany; christian.thiel@dlr.de
- ²⁷ Geoinformatics and Remote Sensing, Institute for Geography, Leipzig University, Johannisallee 19a, D-04103 Leipzig, Germany; michael.vohland@uni-leipzig.de
- ²⁸ Faculty of Mechanical Engineering and Marine Technology, Chair of Ocean Engineering, University of Rostock, Albert-Einstein-Straße 2, D-18059 Rostock, Germany; robert.wagner3@uni-rostock.de
- ²⁹ Department Soil System Science, Helmholtz Centre for Environmental Research–UFZ, Theodor-Lieser-Str. 4, D-06120 Halle, Germany; ute.wollschlaeger@ufz.de
- ³⁰ Remote Sensing Laboratories, Department of Geography, and University Research Priority Program on Global Change and Biodiversity, University of Zurich–Irchel, Winterthurerstrasse 190, CH-8057 Zurich, Switzerland; michael.schaepman@geo.uzh.ch
- * Correspondence: angela.lausch@ufz.de; Tel.: +49-341-235-1961; Fax: +49-341-235-1939

Received: 29 August 2019; Accepted: 1 October 2019; Published: 11 October 2019



Abstract: In the face of rapid global change it is imperative to preserve geodiversity for the overall conservation of biodiversity. Geodiversity is important for understanding complex biogeochemical and physical processes and is directly and indirectly linked to biodiversity on all scales of ecosystem organization. Despite the great importance of geodiversity, there is a lack of suitable monitoring methods. Compared to conventional in-situ techniques, remote sensing (RS) techniques provide a pathway towards cost-effective, increasingly more available, comprehensive, and repeatable, as well as standardized monitoring of continuous geodiversity on the local to global scale. This paper gives an overview of the state-of-the-art approaches for monitoring soil characteristics and soil moisture with unmanned aerial vehicles (UAV) and air- and spaceborne remote sensing techniques. Initially, the definitions for geodiversity along with its five essential characteristics are provided, with an explanation for the latter. Then, the approaches of spectral traits (ST) and spectral trait variations (STV) to record geodiversity using RS are defined. LiDAR (light detection and ranging), thermal and microwave sensors, multispectral, and hyperspectral RS technologies to monitor soil characteristics and soil moisture are also presented. Furthermore, the paper discusses current and future satellite-borne sensors and missions as well as existing data products. Due to the prospects and limitations of the characteristics of different RS sensors, only specific geotraits and geodiversity characteristics can be recorded. The paper provides an overview of those geotraits.

Keywords: geodiversity; geotraits; abiotic diversity; abiotic spectral traits; remote sensing; earth observation; soil characteristic; soil moisture; land surface temperature

1. Introduction

Biodiversity or biotic diversity is the “variability among living organisms from all sources including, among others, terrestrial, marine, and other aquatic ecosystems and the ecological complexes of which they are part; this includes diversity within species, between species, and of ecosystems” (Convention on Biological Diversity-CBD, Article 2, www.cbd.int). It encompasses the diversity of living organisms on different levels of biological organization, which ranges from the molecular level, to the genetic, individual, and species level to populations, communities, biomes, ecosystems, and landscapes is described by five essential characteristics — the phyllo-, taxonomic-, structural, functional, and trait-diversity [1–3]. Biodiversity is essential for ecosystems and their services to function properly, as well as to ensure their resilience [4]. Rapid global change, as well as increased human intervention in ecosystems, are changing biodiversity and ecosystem functions, leading to the degradation of species habitats at an alarming rate and are considered to be the main reasons for disturbances and loss of biodiversity [5]. The consequences are dramatic changes and disturbances to all entities of the biotic and abiotic habitat, starting with epigenetic changes, shifts in traits, and disturbances to biotic and abiotic species communities as far as detrimental changes to entire ecosystems. To better understand the effects of impacts of natural and human disturbances such as land-use intensity or urbanization on ecosystems, it is crucial to know how intra- and interspecific interactions of organisms with one another and their interactions with the abiotic environment control the processes and functions of ecosystems [6].

A major breakthrough in the understanding of ecology was the growing realization that ecosystems consist of both above-ground and below-ground subsystems. The feedback between these two subsystems plays a crucial role in regulating the diversity of the community structure and the functioning of the entire ecosystem [7,8]. Interactions and feedback mechanisms between the biosphere and the geosphere thus play a fundamental role in regulating ecosystem responses, processes, and functions to anthropogenic and global changes and disturbances [6].

Biosphere–geosphere interactions and feedback mechanisms are complex, multidimensional, and mostly non-linear, and vary depending on the spatio-temporal scale on which they are acting [9]. In fact, there are numerous examples of interactions between abiotic and biotic components and interactions on all spatio-temporal scales starting from genes, to the field [10] and regional scale [11], up to landscapes [12]. Geo-drivers and plant traits, for example, lead to characteristic landscape-scale patterns in soil microbial communities [13]. Furthermore, there are strong ecological links between the above-ground and below-ground interfaces of soil biota, plants, and their processes and functions [9,14] or the diversity–function relationships of soil biodiversity and carbon cycling in the soil–plant–atmosphere system [15]. Plants above- and below-ground components respond to stress, disturbances, and the limitations of geo-factors by changing multiple aspects of their plant traits such as biomass allocation, morphology, physiology, or the architecture of plant traits [16,17]. Plants, for example, adapt phenotypically to different light and nutrient conditions to efficiently use these resources. Various abiotic factors such as solar radiation, temperature, water, surface characteristics, and soil conditions influence the richness, abundance, and diversity of plants and thus animal species [18–20]. Land surface temperature (LST) is a key variable for explaining energy and water vapor exchange at the biosphere–atmosphere interface [21]. Water characteristics and eutrophication processes in water bodies also influence biodiversity in the short and long term [22].

Studies have explained the strong link between the leaf traits of plants, climate, and soil measurements of nutrient fertility [23]. Changes in biotic and abiotic interactions may lead to changes in plant communities [24]. In this way, abiotic ecosystem properties and the environmental gradients of climate, topography, soil properties [25–27], or land-use intensity [1,28] and urbanization [2] interact with plants and communities [29], causing variations in the structural, physiological, and functional traits in species, between communities, and biomes. A good example for the strong link between biotic and abiotic interactions are the plant functional types such as the CSR-strategy types (competitor-C, stress tolerator-S, ruderal-R) [25]. Their functional traits alter as a consequence of the adaptation to changes from abiotic conditions caused by land-use intensity or land management strategies. Therefore, plant functional types are dependent on the interaction of abiotic ecosystem properties as well as their survival strategies assigned to groups of plant species with common functional traits [30,31].

Global change not only has a direct effect on biodiversity, distribution, and incidence, but also an indirect effect through the interactions with the geosystems of individual plant species and communities [32–34]. Although ecosystems and biodiversity always had to deal with climate change, it is important to note that the change of air temperature has been faster over the last 10,000 years than in any other recent geological time scales [35]. Global warming and increase in land surface temperature (LST) can lead to an enormous increase in surface water warming rates and phytoplankton biomass in large lakes [36,37]. However, both studies also show how complex and sometimes counterintuitive results can be, if a combination of different geo-variables like climate, local characteristics of water morphology, and the trophic state of water are not included in the assessment of surface water warming [37] or increase in chlorophyll-a concentration as a proxy for phytoplankton biomass [36]. Furthermore, based on pollen counts, it has been demonstrated how the occupation of niches, the distribution, and the migration behavior of plant species have changed as a result of climate change [38]. For forest species in the eastern United States, Fei et al. [39] showed how long-term stress due to climate change and changes in moisture availability led to species divergences in spatial distribution and changed the preference of other forest species' ecological niches. In their study, evergreen trees primarily migrated northwards, whereas deciduous trees moved to the west. Deciduous trees such as oaks and sycamores reacted more sensitively to changes in water availability, whereas they were less sensitive to temperature changes. This indicates that reactions to stress are species-specific [39].

The Nature Conservancy, one of the world's leading conservation organizations, has set the goal of "Conserving nature's stage" [40]. According to that, biodiversity can only be protected by focusing on the maintenance of abiotic conditions, stress, and disturbances, which cannot be separated from biodiversity. In the face of rapid global climate change [41], the increase in land-use intensity [42], and resulting species homogenization [43] as well as increasing urbanization [44], there is a strong necessity for biodiversity research to develop robust methods and models that can monitor, describe, and predict biodiversity and its interactions with abiotic compartments in space and time, with the aim of predicting and responding in a timely manner to changes or disruptions in ecosystem functions and services [45,46]. Given the functional importance of geodiversity and patterns of geomorphology, geology, soil, surface, water, or atmosphere for biodiversity, and the resilience of the ecosystem as a whole, there are enormous gaps and a mismatch in knowledge and monitoring of geodiversity, traits, and their patterns from the local to the global scale [47].

Remote sensing (RS) sensors that are mounted on versatile platforms can record numerous geo-characteristics from the local to the global scale, repeatedly and with different spectral and spatial detail. There are extensive reviews for mapping the properties of land surfaces and their changes [48], soil characteristics [49], and soil moisture [50,51], for monitoring land surface temperature [52] or the diversity of water characteristics and water quality [53,54]. Due to increased open access to data archives such as the Landsat archive [55,56] and the archives hosting the data of the EUs Copernicus Programm including the data of the Sentinel satellites and their predecessors, as well as open software and cloud computing services [57], the potential of RS information to record geo- and biodiversity has improved tremendously [58–60]. On the other hand, there are currently no clear guidelines as to

which RS approaches are suitable for monitoring geo-variables. The objectives of this review paper are therefore:

- Discuss approaches to monitor geodiversity and its traits (geotraits) with RS,
- Define geodiversity and its characteristics,
- Explain the concepts of spectral traits (ST) and the spectral trait variation (STV) approach applicable for monitoring issues,
- Present the state-of-the-art technologies and capabilities of monitoring geodiversity and traits remotely, including: Soil characteristics (mineralogical characterization, pedology, and soil moisture) with different RS sensors, and
- Provide a concise overview of those geo-traits that can be monitored using RS.

2. Understanding Geodiversity

Gray [61] defined “geodiversity” as the diversity of soil, geological, and geomorphological characteristics and the processes that lead to these characteristics. Other definitions of geodiversity integrate elements and characteristics of the lithosphere, the atmosphere, the hydrosphere, and the cryosphere, as well as their processes and interactions within and between the geo-components that are directly and indirectly related to biodiversity [62–64].

Geodiversity in this article is defined as the range and variability of geo-components and their intraspecific and interspecific interactions on all levels of organization of their geo-components. Geodiversity comprises components of the atmospheric, the terrestrial, the marine and aquatic ecosystems, and the ecological complexes to which they belong. Geodiversity is described by five characteristics that appear on all levels of organization and interact with each other. These are (see also Figures 1 and 2):

- (I) Geo-genesis diversity - GGD (which is described by the geo-genesis concept - GGC) represents the diversity of the length of evolutionary pathways, linked to a given set of geo-taxa. Therefore, geo-taxa sets that maximize the accumulation of geo-functional diversity are identified.
- (II) Geo-taxonomic diversity - GTD (which is described by the geo-taxonomic concept, GTaxC) - is the diversity of geo-components that differ from a taxonomic perspective.
- (III) Geo-structural diversity - GSD (which is described by the geo-structural concept, GSC) - is the diversity of composition or configuration of 2D to 4D geo-components.
- (IV) Geo-functional diversity - GFD (which is described by the geo-functional concept, GFC) - is the diversity of geo-functions and processes as well as their intra- and inter-specific interactions.
- (V) Geo-trait diversity - GTD (which is described by the geo-trait concept, GTC) - represents the diversity of biogeochemical, bio-/geo-optical, chemical, physical, morphological, structural, textural, or functional characteristics of geo-components that affect, interact with, or are influenced by the geo-genesis diversity, the geo-taxonomic diversity, the geo-structural diversity, or the geo-functional diversity.

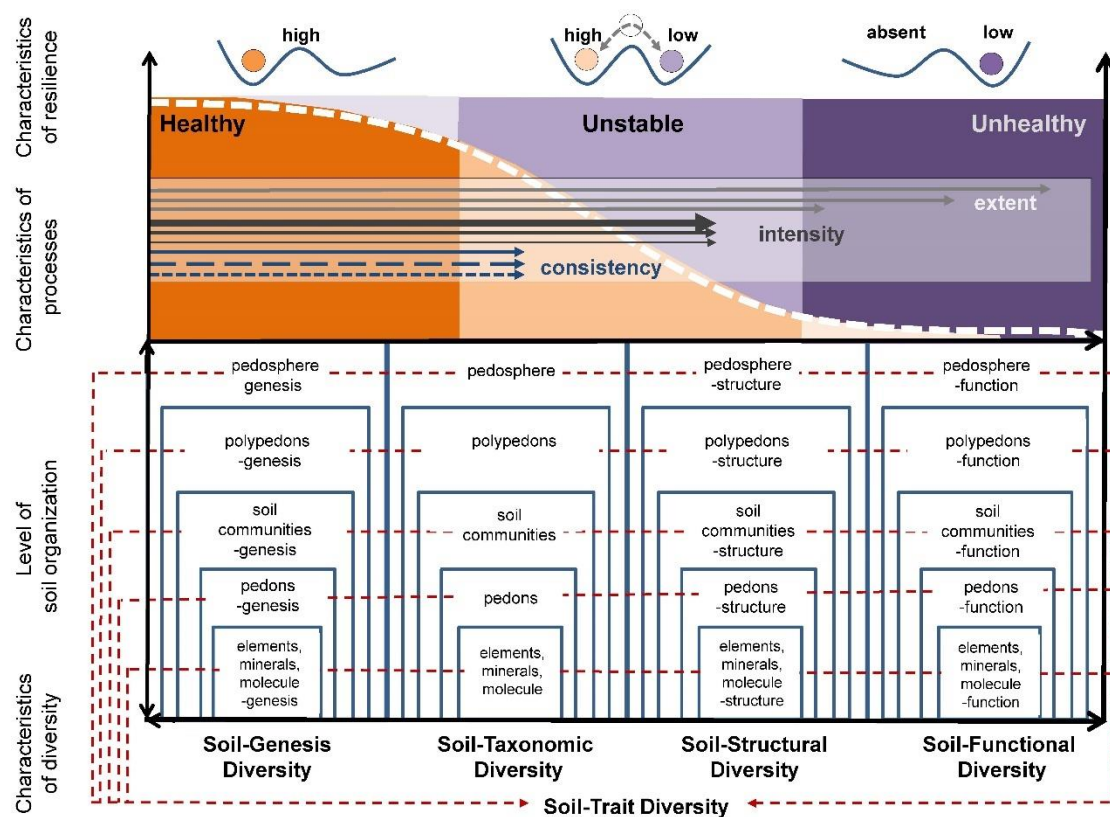


Figure 1. Five characteristics of soil diversity: Soil diversity as part of geodiversity can be described under five characteristics: Soil-genesis diversity, soil-taxonomic diversity, soil-structural diversity, soil-functional diversity, and soil-trait diversity. All of the characteristics involve different levels of soil organization from elements, minerals, molecules, pedons, soil communities, polypedons, up to pedosphere. Different characteristics of the processes (the extent, process intensity, process consistency, resilience, and their characteristics) influence the resilience of soil and ecosystem health (modified after Lausch et al. [57]).

3. Approach for Monitoring Geodiversity by RS

There are two main methods to monitor geodiversity, (i) in-situ or field-based monitoring and (ii) RS. The in-situ approach refers to the direct quantitative and qualitative observation of the environmental spheres (pedosphere, lithosphere, atmosphere, hydrosphere, and cryosphere) either by direct measurements or by laboratory analysis of samples taken directly (destructive) in the environment. By contrast, RS approaches enable a non-destructive monitoring of the geo-characteristics without direct contact. The distance between the sensor and the object can range from a few millimeters to thousands of kilometers, enabling the coverage of diverse scales. In the RS case, the sensors are mounted or integrated onto platforms and can be used at many different scales. RS can be used in the laboratory (e.g., spectro-radiometers), in the field on the ground (e.g., Gamma Ray spectrometry and GPR-ground-penetrating RADAR) to sense features of the Earth's subsurface, or be hand-held or tower-mounted spectro-radiometers or thermal IR sensors (close-range RS techniques). A large range of sensors is airborne (mounted on UAV, in microlights, gyrocopters, or airplanes), or spaceborne (mounted on satellites, space shuttles). The scope of this review paper focuses on the state-of-the-art in monitoring geodiversity and traits using airborne and spaceborne RS sensors and approaches.

RS is capable of monitoring some geotraits and geotrait variations based on the principles of image spectroscopy across the electromagnetic spectrum from ultraviolet light to microwaves. Geo-traits can be directly or indirectly recorded using RS techniques in the time and space domains. Yet, in contrast to in-situ observations, RS approaches are not able to record all geotraits and geotrait variations of the

entities in geodiversity [57] (Figure 2). The geotraits that can be monitored using RS techniques are therefore called spectral traits (ST) and the changes to the spectral traits are referred to as spectral trait variations (STV). Consequently, the related RS approaches are referred to as the remote sensing–spectral traits and –spectral trait variations–concept (RS-SV/STV-C), respectively (Figure 2).

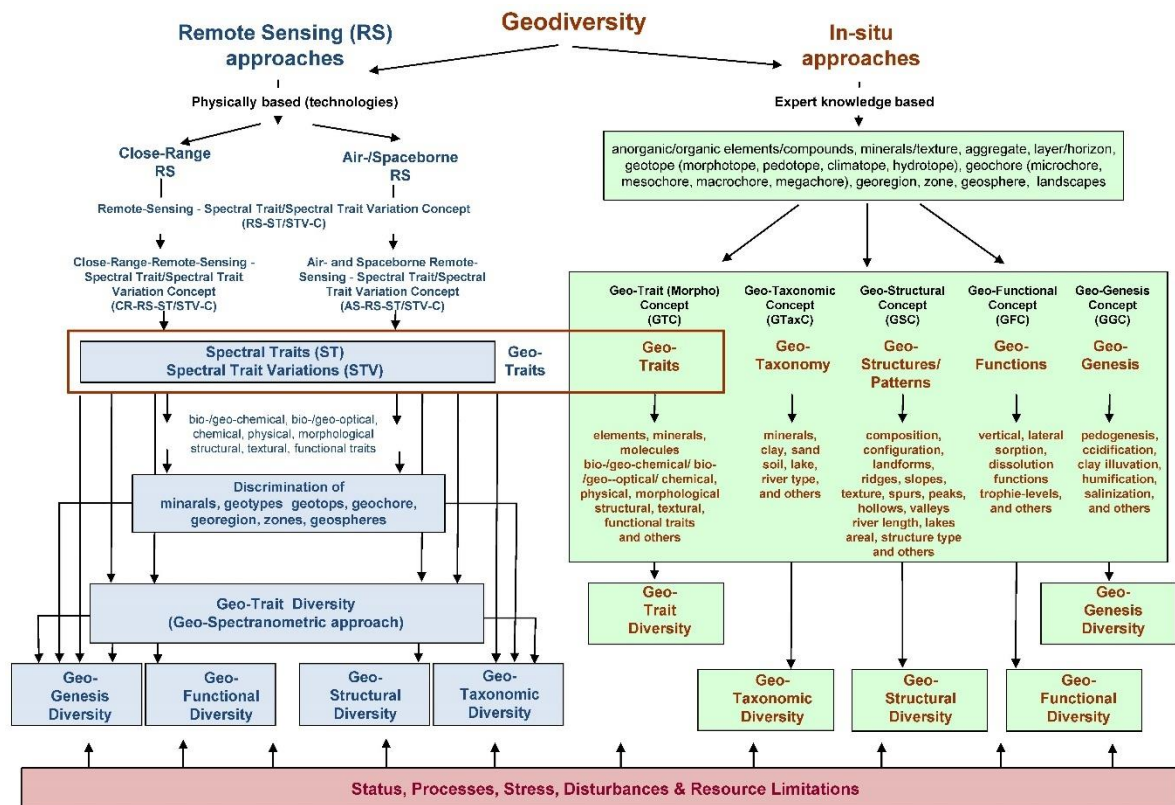


Figure 2. In-situ and remote sensing approaches to monitor geodiversity and their characteristics by remote sensing and in-situ approaches (modified after Lausch et al. [57]).

4. Trends in Air- and Spaceborne RS for Assessing Soil Characteristics

This section provides an overview of the state-of-the-art for assessing and monitoring geodiversity and traits using airborne (UAV, airplanes) and spaceborne (satellite) RS sensors and approaches (Figure 3). We present different technologies such as RADAR (radio detection and ranging) LiDAR, thermal, multispectral, and hyperspectral sensors that are deployed to record geodiversity and traits. We discuss current and future satellite-borne sensors and missions as well as existing data products that allow the respective geo-compartments to be monitored.



Figure 3. Different air- and spaceborne remote sensing platforms for assessing geodiversity and geotraits, (a) unmanned aerial vehicles (UAV, or drone), (b) micro-light-gravity-controlled (c) gyrocopter-micro-light helicopter, (d, top) Ecodemona, (d, bottom) Cessna, (e) satellite.

4.1. Characterization of Soil Diversity and Soil Traits by RS

4.1.1. Mineralogical Characterization by RS

Biodiversity is strongly linked to the prevailing geological and soil characteristics, since bedrock and unconsolidated rock often determines the prevailing pedological and morphological conditions, which not least influence the distribution of animal and plants species, populations, and communities [6,65]. Therefore, mineralogy and soil properties play important roles in determining the ecology of an area through their contribution to the formation of soils and their influence on relief. Both factors can influence local climatic conditions, water availability, and thus the vegetation type and structure. In addition, geology will determine different landforms such as limestone karst, cliffs, and escarpments, which offer a range of different habitats and thus are key to the distribution of flora and fauna.

Space- and air-borne multi- and hyperspectral sensor data can significantly contribute to an area-wide understanding of land cover patterns and vegetation distribution and their changes, which can ultimately alter biodiversity on all spatial scales [48]. Comprehensive overviews of how image spectroscopy has aided the characterization and mapping of soil mineral composition are provided by Mulder et al. [66] and Wulf et al. [49]. Key characteristic surface mineralogical properties, which can be derived from optical RS data in the visible (VIS, $\lambda = 0.4\text{--}0.7\ \mu\text{m}$), near infrared (NIR, $\lambda = 0.7\text{--}1.0\ \mu\text{m}$), and short-wave thermal infrared (SWIR, $\lambda = 1.0\text{--}2.5, 5\text{--}14\ \mu\text{m}$) are clay, sand, carbonate, silicate, sulphate, or iron content (see Table 1). They can be mapped using imaging spectroscopy, for example, with the airborne visible/infrared imaging spectrometer (AVIRIS; [49,67,68]). To access the characteristic absorption features, hyperspectral data are required, which limits the applicability of RS for this issue. EO-1 Hyperion (= Earth Observing-1 Hyperion; [69]) has been the only operational spaceborne imaging spectrometer to date that covers the full spectral range, including the short-wave infrared region for $\lambda > 2\ \mu\text{m}$. Hyperion data were used, for example, to map iron-bearing minerals on tailings, dams, and areas affected by mining in South Africa (Figure 4; [70]). The surface cover of a platinum mine tailings facility was characterized with the United States geological survey (USGS) material identification and characterization algorithm (MICA; [71]) that analyzes the characteristic mineral absorption (Figure 4a). Complementary, the characteristic absorption feature of iron-bearing pyroxenes around $\lambda = 900\ \text{nm}$ was deployed to trace these minerals over a wider area by applying the three-point band depth index “iron feature depth” (IFD) to the multispectral data of Landsat-8 OLI [72]. Figure 4 shows the results of this approach, illustrating the close match to the hyperspectrally mapped iron bearing surface cover types shown in Figure 4a. Further capabilities to map iron were opened with the launch of the Sentinel-2 satellites [73], since the multispectral instrument (MSI) covers important iron absorption features [74]. Another example for the use of Hyperion data is the detection and quantification of different salt types that is combined with the detection of stable and dynamic areas at the surface of a Namibian salt pan on the basis of a 30-year-long Landsat time series [75]. The combination of multispectral time-series for monitoring dynamic processes with hyperspectral observations for soil and sediment characterization enabled the extraction of new knowledge on the salt pan crust development.

Further rock forming and soil mineral contents that are featureless in the VIS-NIR-SWIR can be retrieved from the thermal infrared (TIR, $\lambda = 8\text{--}14\ \mu\text{m}$), where carbonate, clay, quartz, feldspars, olivines, pyroxenes, and micas possess diagnostic spectral features [76]. For instance, the previous advanced spaceborne thermal emission and reflection radiometer (ASTER; [77]) was equipped with six and five bands in the SWIR and TIR region, respectively, and allowed for the (qualitative) mapping of clay minerals (illite, kaolinite), sulfate minerals (alunite), carbonate minerals (dolomite, calcite), iron oxides (goethite, hematite), or silica (quartz), which allowed modifications in facies (propylitic, argillic, etc.; [78]) to be monitored. Furthermore, mineral and lithology mapping was successfully enabled by multispectral TIR sensors like the airborne thermal infrared multispectral scanner (TIMS) [79,80].

Currently, there is no spaceborne hyperspectral TIR sensor available. With the future surface biology and geology (SBG) mission, the mapping of more minerals will be enabled, due to the larger number of bands in the VIS-NIR-SWIR-TIR region and the broad swath-width, which will allow for

more levels of information from complementary spectral regions in a synergistic fashion. Silicate minerals, for instance, demonstrate a distinct emittance minimum caused by fundamental Si–O stretching vibrations occurring near $\lambda = 10 \mu\text{m}$. Quartz and feldspar have emittance minima at shorter wavelengths ($\lambda = 9.3$ and $10 \mu\text{m}$, respectively) than sheet silicates such as muscovite ($\lambda = 10.3 \mu\text{m}$) or chain silicates such as the amphibole minerals ($\lambda = 10.7 \mu\text{m}$; [81]). Carbonates have features associated with CO_3 internal vibrations both at $\lambda = 11.4$ and $14.3 \mu\text{m}$ due to C–O bending modes [82]. Sulfate minerals on the other hand have an intense feature near to $\lambda = 8.7 \mu\text{m}$ caused by fundamental stretching motions [83]. The thermal range of the spectrum has been demonstrated to be very important for an improved determination of sand, clay, and organic carbon content in soils [84,85]. In addition to mineral mapping, the SBG mission should provide important information for soil textural and mineralogical characterization, for example, for sandy soils that are common in semi-arid landscapes.

Currently, several TIR hyperspectral airborne sensors are deployed for geological and soil mapping, including the spatially enhanced broadband array spectrograph system (SEBASS; [86,87]), the airborne hyperspectral scanner (AHS; [88]), AisaOWL [89–91], the thermal airborne spectrographic imagery (TASI; [92]), and the hyperspectral camera HyperCam [93]. In summary, hyperspectral RS allows for the discrimination of similar minerals with spectrally adjacent absorption features. Calcite–dolomite ratios, for example, were mapped in the SWIR using the GER 63-channel imaging spectrometer data (GERIS; [94]) and by SEBASS in the TIR [95]. This type of information can thus be used to monitor and quantify the surface mineralogy that has an impact on biodiversity, from local to global scales.

Geologists have been using RS data since the introduction of RS technology to describe the status as well as the processes of the geology, geo-chemistry, and mineralization of an area, which are the basis of geological mapping, for structural interpretations, and for mineral resource mapping [96,97]. Due to the scope and manifold applications of RS for geological investigations, reference is only made to central work on this subject [78].

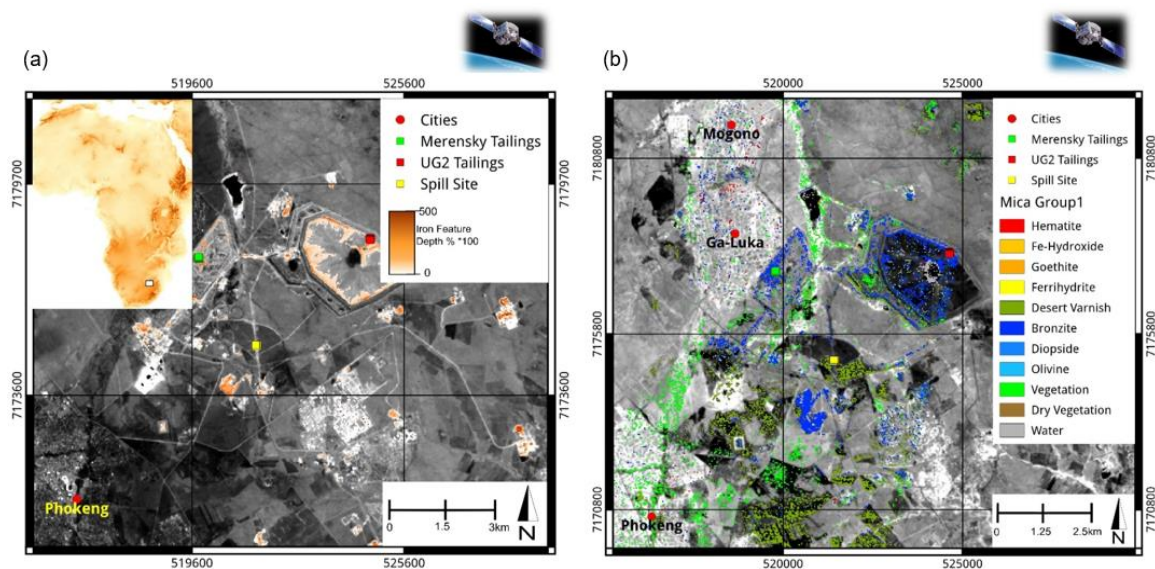


Figure 4. Geological classification: (a) Expert system result showing mineral and material abundance in the Platinum mining area near Rustenburg (USGS MICA) from EO-1 Hyperion data; expert system result overlaid with Landsat-8 OLI near-infrared channel. (b) Iron feature depth result calculated from Landsat-8 OLI data in the Platinum mining area near Rustenburg (USGS MICA). Expert system result overlaid with Landsat-8 OLI short-wave infrared channel. Inset map of the topography of Africa from ETOPO-1 data (data provided with the courtesy of NOAA). White rectangle outlines the areas that are most affected by mining activity in South Africa. (from Mielke et al. [98]).

4.1.2. Pedology

Soil is the uppermost, weathered layer of the Earth's crust. It is a complex matrix at the interface of the lithosphere, biosphere, hydrosphere, and atmosphere governed by different site-specific characteristics. Soil provides the basis for plant growth, which among others is controlled by the physical, chemical, and biological properties of the soil. Soil-related factors like nutrient availability, carbon content, or soil structure affect biodiversity on the one hand, but biodiversity also determines the spatial soil heterogeneity on the other hand [48,99]. As a consequence, there are strong interactions between biodiversity and soil characteristics.

Soil traits can be monitored by RS approaches either directly (from bare soil, (Figure 4, Figure 5, and Table 1) or indirectly, i.e., through vegetation as a sensor or proxy of soil characteristics [48,100]). Thus, direct or indirect indicators derived from remotely sensed satellite or airborne data have been proven to be important for the prediction of soil variables, classes, or processes [101]. They are used in different digital soil mapping approaches, which combine soil-related factors or which are based on environmental similarities or correlations [102].

Following comprehensive reviews of remotely sensed variables for digital soil mapping [48,103–105], remotely sensed indicators can be distinguished according to their spatio-temporal resolution or the respective sensor properties, which can refer to active or passive systems. Active systems like RADAR, LiDAR, or SONAR (sound navigation and ranging) are mainly used to detect surface properties or to estimate soil moisture content (see also chapter 4.3; [106]). Passive systems relate to reflectances and emitted radiation using the VIS-NIR-SWIR, the far-infrared, and the microwave region. Direct reflectances of bare soils enable the prediction of top-soil variables like soil texture, soil organic carbon, iron content, or heavy metals in plants as well as soil salinity or carbonates, the classification of soil types, or even hydraulic properties [107,108]. Since soils are mostly covered by vegetation, spatio-temporal variations in vegetation indices can also help to predict soil properties [109].

Imaging spectroscopy for mapping soil characteristics in the VIS-NIR-SWIR domain emerged at the beginning of the 21st century [110,111]. It builds upon many years of extensive research in soil spectroscopy under laboratory conditions (e.g., [111]), which revealed quantitative and qualitative relationships between the spectral signal and the chemical and physical properties of soils [112]. Castaldi et al. [113] recently showed that narrowband, hyperspectral imagers provide significantly higher potential for the quantitative estimation of soil variables compared to multispectral sensors because broadband instruments cannot resolve diagnostic spectral features of the soil spectrum. On the other hand, recent works show the potential of the Sentinel-2 sensor for soil organic carbon mapping [99,113]. For both laboratory and imaging spectroscopy, mostly non-parametric regression algorithms are applied [114]. Focusing on single mineral absorption features has been proven to be less successful due to the complex nature of soil [115]. Although automatic methods such as the HYSOMA (hyperspectral soil mapper) algorithms [116] are based on the direct analyses of the spectral signal, they proved to be more generic and have the potential to be transferable to the regional–global scale [117,118].

Compared to in-situ approaches, there are several items that make the remote spectroscopy of soils challenging. Firstly, optical RS captures only the properties of the uppermost centimeters of the top-soil and cannot provide information about the entire soil body. Secondly, atmospheric effects and sensor constraints [119], soil moisture contents [120], soil roughness, or soil surface coverage by vegetation or plant residues [117] can interfere with the spectral signal [121].

Vegetation cover is a major challenge in RS aided soil trait estimation in many parts of the world. Ouerghemmi et al. [122] reported that prediction errors increased progressively as vegetation cover exceeded 5% to 10%. The majority of hyperspectral studies therefore focus on bare soils accepting that a noticeable amount of cultivated area cannot be mapped instantly. The associated limitations can be reduced, either by the multi-temporal stacking of soil maps [123], pixel compositing [124], or by applying advanced algorithms to correct for the impact of vegetation [125] and soil moisture [126]. Beyer et al. [127] for example, suggested calculating a residual soil signature to reduce the influence of

non-soil materials. Another strategy for areas with permanent vegetation may be to infer information on the underlying soil by exploring the spectral signal of the vegetation itself [128,129]. In this indirect approach, vegetation traits are used as indicators for the status or changes of soil traits [100].

Irrespective of the limitations of imaging spectroscopy, its potential to provide quantitative and qualitative soil information is demonstrated by several studies: Ben-Dor et al. [130] were some of the first to apply hyperspectral image data from the DAIS 7915 airborne scanner for the mapping of soil characteristics of clayey soils in Israel. They obtained reliable predictions for soil moisture, soil salinity (electrical conductivity), soil saturated moisture, and organic matter content, disclosing the spatial distribution of soil properties in the study area. Selige et al. [131] estimated the percentage of soil organic carbon, total nitrogen, sand, and clay of agricultural fields on a test site in East Germany from image data of the Australian HyMap sensor. Vohland et al. [132] used HyMap data to estimate soil organic carbon and, as a sub-fraction, microbial biomass-carbon for agricultural soils. The soil organic carbon content has also been explored in several other studies, for example by Stevens et al. [118] on Central European croplands in Luxembourg using the airborne hyperspectral scanner AHS-160 or by Castaldi et al. [113], who analyzed data from the airborne prism experiment (APEX) acquired in Belgium and Luxembourg. Deploying the Aisa/DUAL system, Kanning et al. [133] estimated soil organic carbon (SOC) [134] and the soil particle fraction sand, silt, and clay. Furthermore, Paz-Kagan et al. [135] developed a spectral soil quality index (SSQI) using airborne imaging spectroscopy. Selige et al. [131] and Vohland et al. [132] showed that nitrogen (an essential nutrient for plant growth) can be estimated by imaging spectroscopy. Further studies on nitrogen have been conducted under standardized conditions in the laboratory [136]. Imaging spectroscopy can also provide some insights into the pedogenesis processes, land degradation, and erosion processes by mapping the iron content as shown by [137], or by direct mineralogical mapping in association with erosion and deposition stages [138]. Applications on soil crust mapping were also successful for physical crust [139] and biological crust discrimination in the laboratory and the field [140], although at the imagery scale these applications are still challenging and scarce.

In terms of multi-spectral imagery provided by satellite sensors, a multitude of approaches have been successfully applied using sets of environmental covariates over recent decades [48]. With the increased spatio-temporal availability of remotely-sensed imagery and other auxiliary data such as digital elevation models, “digital soil mapping has shifted from a research phase into operational use” [102]. Since RS imagery is affected by different atmospheric conditions and soil moisture variations on image acquisition dates, the transferability of digital soil mapping solutions remains a key challenge [141]. To this end, the derivation of indicators based on the analysis of multi- (three or more images) or hyper-temporal imagery (e.g., images for one or many years; [105]) may be useful. Multi- or hyper-temporal image data can be obtained from satellite image archives [142] or be generated by applying data fusion algorithms [143]. Maynard and Levi [105] for example, were able to show that hyper-temporal time series of a vegetation index based on Landsat imagery enable typical and temporally stable spectral fingerprints to be derived, which significantly increased the prediction accuracy of soil texture. Especially in agricultural regions, multi- and hyper-temporal imagery enables bare soil areas to be detected at different time steps. As a result, regional [144] and even national bare soil composites [145,146] can be created and used for soil mapping parameterization.

Blasch et al. [147] applied multi-temporal RapidEye composites to predict spatial variations in soil organic matter (SOM). Multi-temporal Landsat image composites have also been used by Dematte et al. [148] in order to perform soil texture classification. Since soil-related indicators based on multi- and hyper-temporal time series or composites are less affected by atmospheric conditions and soil moisture variations, they can be considered as a key for the automatic and operational derivation of standardized soil mapping products. Standardization means that all steps of geodata processing are reproducible, harmonized protocols are applied, and that the soil mapping products are evaluated by accuracy metrics [149]. This concerns both digital soil mapping parameterization and the provision of scale-specific harmonized and representative training samples [150,151].

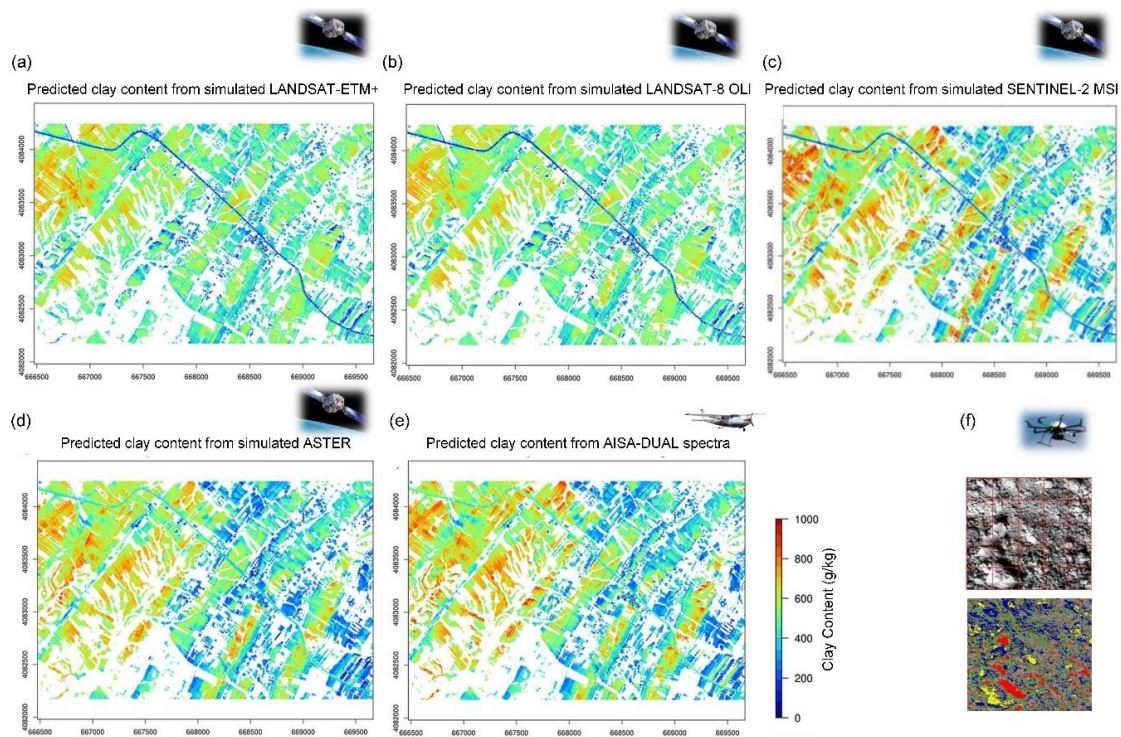


Figure 5. Maps of clay content over the Kamech catchment predicted from the PLSR (partial least squares regression) models using spectral configurations from (a) LANDSAT-7 ETM+, (b) LANDSAT-8 OLI, (c) SENTINEL-2 MSI, (d) ASTER, (e) AISA-DUAL (from Gomez et al. [68], License Number 4582290225360; (f) soil texture and soil microstructures derived from hyperspectral video camera–Cubert (from Jung et al. [136]).

The RS-aided derivation of soil characteristics and soil traits shown in Table 1 and Figure 6 shows the enormous number of current and future space-based RS missions and satellites for monitoring soil characteristics and traits with information about the mission status, according to the CEOS database (Committee on Earth Observation Satellites).

Table 1. Remote sensing (RS)-aided derived soil characteristics and soil traits.

Mission/Sensor/ Platform	Sensor Type	Spectral Resolution Spectral Bands/Frequency	Spatial Resolution [m]	References
UAV ¹ Airborne ² Spaceborne ³				
Clay Content				
Landsat 5 TM ³ Landsat 7 ETM+ ³	Multispectral/TIR	0.45–12.5 μm/8	L5:30/120 L7:30/60	[68]
Landsat 8 OLI/TIRS ³	Multispectral/TIR	0.43–2.3 μm/8 10.6–12.51 μm/2	30/100	[68]
Terra ASTER ³	Multispectral/TIR	0.52–9.2 μm/9 8.12–11.65 μm/5	30/90	[68,80,85]
Sentinel-2 MSI ³	Multispectral	0.40–3.0 μm/13	10/20/60	[68]
IKONOS OSA ³	Multispectral	0.45–0.85 μm/4	4	[152]
AHS ²	Hyperspectral	0.43–12.7 μm/~80	~2	[88]
AisaDUAL ²	Hyperspectral	0.40–2.45 μm/~200–400	~1–5	[68,151]
AisaOWL ²	Hyperspectral Longwave Infrared (LWIR)	7.7–12.0 μm/~100	~2	[89,90]
AVNIR ²	Hyperspectral	0.43–1.01 μm/~60	~1.20	[153]
AVIRIS ²	Hyperspectral	0.37–2.45 μm/~200	~18	[67,154]
DAIS-7915 ²	Hyperspectral	0.40–2.50 μm/~72	~8	[130]
EnMAP ² (simulated)	Hyperspectral	0.42–2.45 μm/~250	30	[155]
HyMAP ²	Hyperspectral	0.45–2.48 μm/~125	~5	[84,115–117,123, 131,156]

Table 1. Cont.

Mission/Sensor/ Platform UAV ¹ Airborne ² Spaceborne ³	Sensor Type	Spectral Resolution Spectral Bands/Frequency	Spatial Resolution [m]	References
Clay Content				
HySpex ²	Hyperspectral	0.40–2.45 μm /~200–400	~1–5	[157]
HyperSpecTIR ²	Hyperspectral	0.40–2.45 μm /~178	~2.5	[158]
TASI-600 ²	Thermal Airborne Spectrographic Imager	8.0–11.4 μm /~32	~1–5	[84,85]
SEBASS ²	Hyperspectral Thermal Infrared (TIR) Sensor	2.5–13.5 μm /~260	~2	[87,95]
Cubert UHD 185 ¹	Hyperspectral	0.45–0.95 μm /~125	~ 0.2–0.5	[95]
Silt Content				
AisaDUAL ²	Hyperspectral	0.40–2.45 μm /~200–400	~1–5	[133]
HyperSpecTIR ²	Hyperspectral	0.40–2.45 μm /~178	~2.5	[158]
Sand Content				
EO-1 Hyperion ³	Hyperspectral	0.40–2.50/242 μm /220	30	[159]
AisaDUAL ²	Hyperspectral	0.40–2.45 μm /~200–400	~1–5	[133]
HyMAP ²	Hyperspectral	0.45–2.48 μm /~125	~5	[84]
HyperSpecTIR ²	Hyperspectral	0.40–2.45 μm /~178	~2.5	[158]
TASI-600 ²	Thermal Airborne Spectrographic Imager	8.0–11.4 μm /~32	~1–5	[84]
Carbonate Content				
Terra ASTER ³	Multispectral/TIR	0.52–9.2 μm /9 8.12–11.65 μm /5	30/90	[76,79,80,85]
AVIRIS ²	Hyperspectral	0.37–2.45 μm /~200	~18	[67]
HySpex ²	Hyperspectral	0.40–2.45 μm /~200–400	~1–5	[115,116]
HyMAP ²	Hyperspectral	0.45–2.48 μm /~125	~5	[117,156,160]
HyperSpecTIR ²	Hyperspectral	0.40–2.45 μm /~178	~2.5	[158]
AisaOWL ²	Hyperspectral Longwave Infrared (LWIR)	7.7–12.0 μm /~100	~2	[89]
SEBASS ²	Hyperspectral Thermal Infrared (TIR) Sensor	2.5–13.5 μm /~260	~2	[86,87,95]
Iron Content				
Terra ASTER ³	Multispectral/TIR	0.52–9.2 μm /9 8.12–11.65 μm /5	30/90	[76]
Sentinel-2 MSI ³	Multispectral	0.40 3.0 μm /13	10/20/60	[76]
EnMAP ² (simulated)	Hyperspectral	0.42–2.45 μm /~250	30	[155]
CASI ²	Hyperspectral	0.40–1.0/ 48	~3	[137]
HyMAP ²	Hyperspectral	0.45–2.48 μm /~125	~5	[98,117,155]
HySpex ²	Hyperspectral	0.40–2.45 μm /~200–400	~1–5	[98,155]
HyperSpecTIR ²	Hyperspectral	0.40–2.45 μm /~178	~2.5	[158]
ROSIS ²	Hyperspectral	0.42–0.87/ 115	~2	[161]
TASI-600 ²	Thermal Airborne Spectrographic Imager	8.0–11.4 μm /~32	~1–5	[84]
Heavy metals (in plants and vegetation)				
HyMAP ²	Hyperspectral	0.45–2.48 μm /~125	~5	[162]
Silicate Content				
Terra ASTER ³	Multispectral/TIR	0.52–9.2 μm /9 8.12–11.65 μm /5	30/90	[76,80]
AHS ²	Hyperspectral	0.43–12.7 μm /~80	~2	[88]
AisaOWL ²	Hyperspectral Longwave Infrared (LWIR)	7.7–12.0 μm /~100	~2	[89,91]
HyMAP ²	Hyperspectral	0.45–2.48 μm /~125	~5	[84]
SEBASS ²	Hyperspectral Thermal Infrared (TIR) Sensor	2.5–13.5 μm /~260	~2	[86,87,95]
TASI-600 ²	Thermal Airborne Spectrographic Imager	8.0–11.4 μm /~32	~1–5	[85]
Sulphate Content				
Terra ASTER ³	Multispectral/TIR	0.52–9.2 μm /9 8.12–11.65 μm /5	30/90	[80]
AisaOWL ²	Hyperspectral Longwave Infrared (LWIR)	7.7–12.0 μm /~100	~2	[89]
AisaFENIX ²	Hyperspectral	0.40–2.45 μm /~200–400	~1–5	[90]
AVIRIS ²	Hyperspectral	0.37–2.45 μm /~200	~18	[67]
SEBASS ²	Hyperspectral Thermal Infrared (TIR) Sensor	2.5–13.5 μm /~260	~2	[87,95]
Granitoid Classification				
TASI-600 ²	Thermal Airborne Spectrographic Imager	8.0–11.4 μm /~32	~1–5	[92]
Further Elements: (Chemometric diversity of soil)				
Aluminium (AL), Potassium (K), Calcium (Ca), Magnesium (Mg), Manganese (Mn), Zinc (Zn), (Ni)				
HyperSpecTIR ²	Hyperspectral	0.40–2.450 μm /~178	2.5	[158]
HyMAP ²	Hyperspectral	0.45–2.48 μm /~125	~5	[131,132]

Table 1. Cont.

Mission/Sensor/ Platform UAV ¹ Airborne ² Spaceborne ³	Sensor Type	Spectral Resolution Spectral Bands/Frequency	Spatial Resolution [m]	References
Soil Organic Carbon (SOC)				
Terra ASTER ³	Multispectral/TIR	0.52–9.2 $\mu\text{m}/9$ 8.12–11.65 $\mu\text{m}/5$	30/90	[163]
Sentinel-2 MSI ³	Multispectral	0.40–3.0 $\mu\text{m}/13$	10/20/60	[164]
EO-1 Hyperion ³	Hyperspectral	0.40–2.50/242 $\mu\text{m}/196$	30	[115]
AHS ²	Hyperspectral	0.43–12.7 $\mu\text{m}/\sim 80$	~ 2	[118]
AisaDUAL ²	Hyperspectral	0.40–2.45 $\mu\text{m}/\sim 200\text{--}400$	$\sim 1\text{--}5$	[133]
APEX ²	Hyperspectral	0.40–2.50 $\mu\text{m}/\sim 320$	$\sim 1\text{--}3$	[113]
AVNIR ²	Hyperspectral	0.43–1.01 $\mu\text{m}/\sim 60$	~ 1.20	[153]
DAIS-7915 ²	Hyperspectral	0.40–2.50 $\mu\text{m}/72$	8	[130]
EnMAP ² (simulated)	Hyperspectral	0.42–2.45 $\mu\text{m}/\sim 250$	30	[155]
HyMAP ²	Hyperspectral	0.45–2.48 $\mu\text{m}/\sim 125$	~ 5	[84,123,127,131, 132,165]
TASI-600 ²	Thermal Airborne Spectrographic Imager	8.0–11.4 $\mu\text{m}/\sim 32$	$\sim 1\text{--}5$	[84]
Soil Organic Matter (SOM)				
HyMAP ²	Hyperspectral	0.45–2.48 $\mu\text{m}/\sim 125$	~ 5	[84]
TASI-600 ²	Thermal Airborne Spectrographic Imager	8.0–11.4 $\mu\text{m}/\sim 32$	$\sim 1\text{--}5$	[84]
HyperSpecTIR ²	Hyperspectral	0.40–2.45 $\mu\text{m}/\sim 178$	~ 2.5	[158]
Total Nitrogen				
HyMAP ²	Hyperspectral	0.45–2.48 $\mu\text{m}/\sim 125$	~ 5	[131,132]
Microbial Biomass C (MBC)				
HyMAP ²	Hyperspectral	0.45–2.48 $\mu\text{m}/\sim 125$	~ 5	[132]
Hot Water Extractable C (HWEC)				
HyMAP ²	Hyperspectral	0.45–2.48 $\mu\text{m}/\sim 125$	~ 5	[132]
pH -Soil				
HyperSpecTIR ²	Hyperspectral	0.40–2.45 $\mu\text{m}/\sim 178$	~ 2.5	[158]
Salinity (EC)				
Landsat 5 TM ³ Landsat 7 ETM+ ³	Multispectral/TIR	0.45–2.3 $\mu\text{m}/6$ 10.4–12.5 $\mu\text{m}/1$	L5:30/120 L7:30/60	[166,167]
Landsat 8 OLI/TIRS ³	Multispectral/TIR	0.43–2.3 $\mu\text{m}/8$ 10.6–12.51 $\mu\text{m}/2$	30/100	[168]
Sentinel-2 MSI ³	Multispectral	0.40–3.0 $\mu\text{m}/13$	10/20/60	[169]
HyMAP ²	Hyperspectral	0.45–2.48 $\mu\text{m}/\sim 125$	~ 5	[130,170]
AIRSAR TOPSAR ²	Microwave	P-, L-bands (full polarimetric), C-band (VV polarization)		[171]
JERS-1 ³	Microwave	L-band (23 cm)-HH pol		[171]
Cation-Exchange Capacity (CEC)				
HyMAP ²	Hyperspectral	0.45–2.48 $\mu\text{m}/\sim 125$	~ 5	[117,139]
Soil crust (physical, biological crust)				
Landsat 5 TM ³ Landsat 7 ETM+ ³	Multispectral/TIR	0.45–2.3 $\mu\text{m}/6$ 10.4–12.5 $\mu\text{m}/1$	L5:30/120 L7:30/60	[172]
AISA-EAGLE ²	Hyperspectral	0.42–0.89 $\mu\text{m}/\sim 30$	~ 3	[173]
DAIS-791 ²	Hyperspectral	0.50–2.50 $\mu\text{m}/\sim 72$	$\sim 1\text{--}3$	[174]
CASI ²	Hyperspectral	0.42–0.95 $\mu\text{m}/\sim 36$	~ 1	[175]
Soil surface roughness				
TerraSAR-X/TanDEM-X ³	X-band	9.63 GHz		[176]
Sentinel-1 ³	C-band	5.3 GHz		[177]
PLMR ² InfraTec thermal imager ² AISA-EAGLE ²	L-band microwave radiometer / TIR/ Hyperspectral	1.26 GHz 7.5–14 μm 0.42–0.89 $\mu\text{m}/\sim 30$	$\sim 3\text{--}5$	[178]
Riegl-LMS-Q560 full-waveform 2D laser scanner-LiDAR ²	LiDAR	240 KHz		[179]
RGB-Camera-UAV ¹	Photogrammetry		$\sim 1\text{--}4\text{mm}$	[180]
Soil texture, sediment texture				
Landsat 5 TM ³ Landsat 7 ETM+ ³	Multispectral/TIR	0.45–2.3 $\mu\text{m}/6$ 10.4–12.5 $\mu\text{m}/1$	L5:30/120 L7:30/60	[166]
Landsat 8 OLI/TIRS ³	Multispectral/TIR	0.43–2.3 $\mu\text{m}/8$ 10.6–12.51 $\mu\text{m}/2$	30/100	[159]
Terra ASTER ³	Multispectral/TIR	0.52–9.2 $\mu\text{m}/9$ 8.12–11.65 $\mu\text{m}/5$	30/90	[181]

Table 1. Cont.

Mission/Sensor/ Platform UAV ¹ Airborne ² Spaceborne ³	Sensor Type	Spectral Resolution Spectral Bands/Frequency	Spatial Resolution [m]	References
Sentinel-2 MSI ³	Multispectral	0.40–3.0 μm/13	10/20/60	[159]
EO-1 Hyperion ³	Hyperspectral	0.40–2.50/242 μm/220	30	[159]
HyMAP ²	Hyperspectral	0.45–2.48 μm/~125	~5	[117,123]
EnMAP ² (simulated)	Hyperspectral	0.42–2.45 μm/~250	30	[155,159]
AisaDUAL ²	Hyperspectral	0.40–2.45 μm/~200–400	~1–5	[182]
Sediment dynamic				
EO-1 Hyperion ³	Hyperspectral	0.40–2.50/242 μm/220	30	[75]
Terra/Aqua MODIS ³	Multispectral/TIR	0.41–14.34 μm/36	250/500/1km	[183]
Land degradation				
Terra/Aqua MODIS ³	Multispectral/TIR	0.41–14.34 μm/36	250/500/1km	[184]
Soil erosion				
Landsat 5 TM ³ Landsat 7 ETM+ ³	Multispectral/TIR	0.45–2.3 μm/6 10.4–12.5 μm/1	L5:30/120 L7:30/60	[185]
Landsat 8 OLI/TIRS ³	Multispectral/TIR	0.43–2.3 μm/8 10.6–12.51 μm/2	30/100	[186]
Sentinel-1 ³	C-band	5.3 GHz		[177]
UAV¹				
Lumix DMC-LX3 (Panasonic); Sony NEX 5N (Sony)	Photogrammetry	2 & 4 μm	2–4 mm	[187]
Desertification processes				
Landsat 8 OLI/TIRS ³	Multispectral/TIR	0.43–2.3 μm/8 10.6–12.51 μm/2	30/100	[188]
Spectral Soil Quality Index (SSQI)				
AisaDUAL ²	Hyperspectral	0.40–2.45 μm/~200–400	~1–5	[135]

Sensor is used on the RS platform: UAV¹ - unmanned aerial vehicles (UAV); airborne² – airborne RS platform; spaceborne³ – spaceborne RS platform.

See Chabrillat et al. [121] for a recent review of the potential of upcoming spaceborne hyperspectral imagery for global soil mapping and monitoring. Table 2 provides an overview of the recent and future spaceborne hyperspectral missions with their sensor characteristics deriving soil characteristics and traits.

Table 2. Current and future important spaceborne hyperspectral missions with their sensor characteristics deriving soil characteristics and their traits (modified after [189]).

Mission/ Sensor	Organisation (Country)	Spatial Resolution [m]	Swath at Nadir [km]	Spectral Resolution [μm]	Number of Bands	Spectral Resolution [nm @FWHM]	Launch Year	Reference
Missions Currently in Orbit								
Hyperion	NASA (USA)	30	7.65	0.37–2.57	242	10	2000	[69]
CHRIS	ESA (UK)	17/34	13 (nominal)	0.40–1.05	18/63	5.6–32.9	2001	[190]
HJ-1A	CAST (China)	100	≥50	0.45–0.95	110–128	5	2008	[191]
HySI	ISRO (India)	506	129.5	0.45–0.95	64	~10	2008	[192]
HICO	NASA/ONR (USA)	90	42	0.35–1.08	128	5.7	2009	[193]
Missions under construction								
GISAT	ISRO (India)	500	NA	NA	210	NA	2019	[194]
PRISMA	ASI (Italy)	30	30	0.40–2.50	237	~12	2019	[195]
HISUI	METI (Japan)	30	15	0.40–2.50	185	10 (VNIR) 12.5 (SWIR)	2019	[196]
EnMAP	DLR/GFZ (Germany)	30	30	0.42–2.45	218	5/10 (VNIR) 10 (SWIR)	2020	[197]
Missions in the planning stage								
FLORIS/FLEX	ESA	300	100–150	0.50–0.78	NA	0.3–3.0	2022	[198,199]
HYPXIM-P	CNES (France)	8	16	0.40–2.50	>200	≤10	In study	[200]
HyspIRI	NASA (USA)	60	145	0.38–2.50	>200	10	2025	[129]
CHIME	ESA	20–30	NA	0.40–2.50	>200	10	2025	[201,202]
SHALOM	ISA/ASI (Israel/Italy)	10/5	10	0.40–2.50	200	10	2022	[203]

Table 3 provides an overview of current and future important missions of the Copernicus program – Sentinel satellites monitoring geodiversity and their traits developed by ESA. For more information about the sensor characteristics of the Sentinel Satellites, see also Malenovský et al. [204].

Table 3. Current and future important missions of the Copernicus program – Sentinel satellites for derivation of geodiversity and their traits developed by ESA.

Sentinel Satellite	Sensor Type		Link	Spatial Resolution	Launch Time
S-1	RADAR	land and ocean monitoring, ice mapping, ground movements	https://www.esa.int/Our_Activities/Observing_the_Earth/Copernicus/Sentinel-1	5–20 m	S-1A–2014 S-1B–2016 S-1C–2022 S-1D–2028
S-2	Multi-spectral	land monitoring, land cover/land use, vegetation, soil and water cover, inland waterways, and coastal areas	https://www.esa.int/Our_Activities/Observing_the_Earth/Copernicus/Sentinel-2	10–60 m	S-2A–2015 S-2B–2017 S-2C–2022 S-2D–2029
S-3	RADAR and multispectral	land- and ocean monitoring, sea-surface topography, sea- and land-surface temperature, ocean color, land color	https://www.esa.int/Our_Activities/Observing_the_Earth/Copernicus/Sentinel-3	300–1000 m	S-3A–2016 S-3B–2018 S-3C–2023 S-3D–2029
S-4	Atmospheric sensors optical, geo-stationary	atmospheric monitoring Air quality (O3, NO2, SO2)			S-4A–2022 S-4B–2032
S-5	Atmospheric sensors optical	air quality (O3, NO2, SO2, HCHO, CO, CH4)			S-5A–2013 S-5B–2030 S-5B–2037
S-5P Sentinel-5 Precursor	Atmospheric sensors optical	air quality (O3, UV)	https://www.esa.int/Our_Activities/Observing_the_Earth/Copernicus/Sentinel-5P	7 × 3.5 km	S-5-2017
S-6	RADAR-Altimeter	global sea-surface height, primarily for operational oceanography and for climate studies			S-6A–2020 S-6B–2025

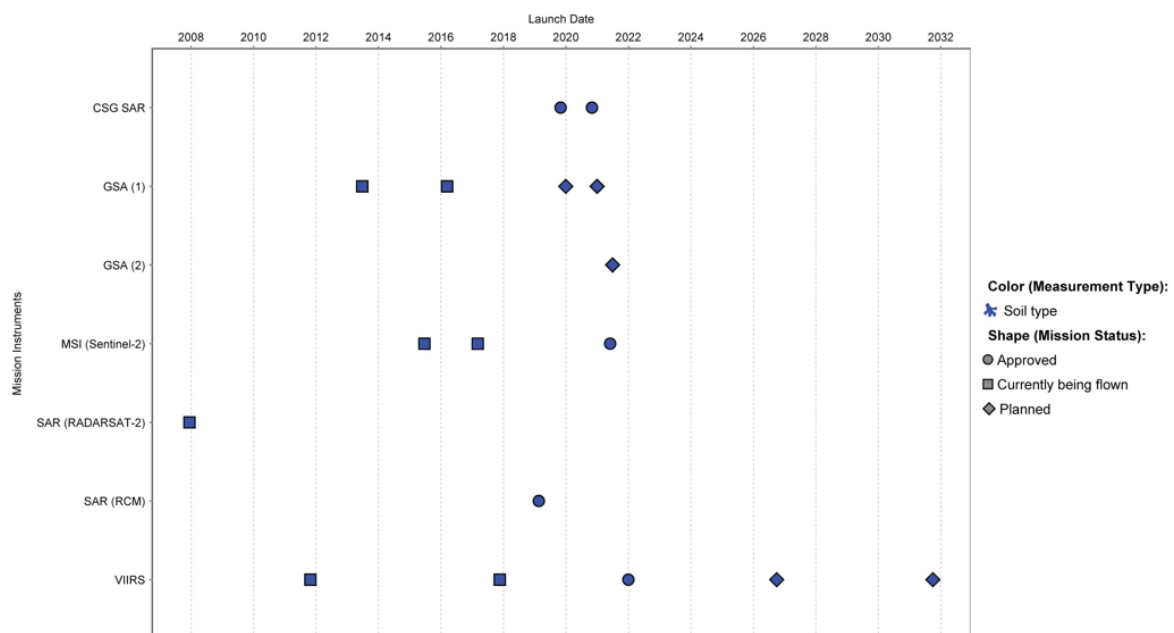


Figure 6. Current and future RS missions and RS satellites for monitoring soil characteristics with information about the mission status, extracted from the CEOS database (Committee on Earth Observation Satellites) [205].

Table 4 gives a selection of RS-aided data products of soil characteristics.

Table 4. Selection of RS-aided data products of soil characteristics.

Data Products	Scale	Link	References
State Soil Geographic (STATSGO) database	Global	https://gcmd.nasa.gov/KeywordSearch/Metadata.do?Portal=idn_ceos&KeywordPath=%5BKeyword%3D%27USDA%27%5D&OrigMetadataNode=GCMD&EntryId=MSU0035&MetadataView=Full&MetadataType=0&lbnode=mdlb3	[206]
Imperious Surface Cover	Global	http://www.landcover.org/data/isa/	[207]
Global Soil Texture and Derived Water-Holding Capacities	Global	https://data.globalchange.gov/dataset/nasa-ornlldaac-548 https://doi.org/10.3334/ORNLLDAAC/548	[208]
Global 1-Degree Vegetation and Soil Types	Global	https://rda.ucar.edu/datasets/ds767.0/	[209]
Global Soil Types, 1-Degree Grid (Zobler)	Global	https://data.nasa.gov/dataset/Global-Soil-Types-1-Degree-Grid-Zobler-/2wbf-79dx	NA
Global Soil Regions	Global	https://sdgs-amerigeoss.opendata.arcgis.com/datasets/204d94c9b1374de9a21574c9efa31164_2	NA
Global assessment of soil phosphorus retention potential	Global	https://doi.org/10.1594/PANGAEA.858549	[210]
Global Soil Biodiversity Atlas Maps	Global	https://ec.europa.eu/jrc/en	NA
Harmonized Soil Carbon Database	Global	https://climatedataguide.ucar.edu/climate-data/harmonized-soil-carbon-database	NA
Soil Geographic Databases	Global	https://www.isric.org/explore/soil-geographic-databases	NA
Using greenhouse gas fluxes to define soil functional types	Global	https://datadryad.org/resource/doi:10.5061/dryad.kq7h7	[211]
Global Gridded Surfaces of Selected Soil Characteristics (IGBP-DIS)	Global	https://doi.org/10.3334/ORNLLDAAC/569	NA
Global Soil Wetness Project (GSWP)	Global	http://grads.iges.org:80/gswp/	NA
Global and regional phosphorus budgets in agricultural systems and their implications for phosphorus-use efficiency	Global	https://doi.org/10.1594/PANGAEA.875296	[212]
SoilGrids (250m and 1km)	Global	http://soilgrids.org	[213]

4.2. Soil Moisture by RS

Soil moisture is part of the hydrological cycle, even if it only accounts for 0.001% of the global water storage, it still has a crucial effect on compositional, structural, and functional biodiversity [101,214,215]. Volume distribution and temporal dynamics of moisture within the soil are key drivers of biodiversity. Part of the soil water (the so-called plant available soil water) is accessible to plants for metabolic processes. The temporal and spatial dynamics of soil moisture reflecting the interplay between evaporation, transpiration, infiltration, and the replenishment of groundwater are imperative to understand water movements in the soil and the water cycle at local to global scales [216].

A reliable and adequate description of the spatial and temporal heterogeneity of soil moisture is one of the most critical challenges in the monitoring and modelling of water and energy fluxes, nutrient transport, and matter turnover within soil landscape systems. In order to generate reliable predictions about these processes from models, sufficient knowledge needs to be gained about the soil heterogeneity and moisture patterns at larger scales [217]. Furthermore, soil moisture is a key variable controlling biosphere–pedosphere/process–pattern interactions, hydrological, and biological processes, not to mention climate and other ecosystem processes including the dynamics in biodiversity [218].

Vereecken et al. [101] found that soil moisture was the most important driver, accounting for 65% of the variation in ecosystem multi-functionality. Moeslund et al. [219] found that soil moisture drives plant diversity patterns within grasslands. They calculated relative ecological indicator values for soil moisture and found pronounced differences in the responses of grassland types to grazing depending on the moisture regimes with an increasing effect of grazing from the dry towards the wet grassland types [219]. Especially in extreme ecosystems, e.g., the dry valleys of Antarctica, spatial soil moisture and soil carbon patterns dominate the distribution of soil organisms [220]. Established patterns of soil biological communities due to changes in soil moisture and temperature also vary over seasonal

or larger time scales and alter the resource supply for the growth of plants. Droughts, for example, change the relationship between biodiversity and ecosystem functioning [221]. Moreover, projected increasing climate-induced drought severity suggests that changing tree and forest biogeography could substantially lag habitat shifts that are already underway [222]. One interesting example is that of nematodes (roundworms) that can enter anhydrobiosis and become inactive when the soil is dry. Therefore, their activity is closely related to levels of soil moisture, and the proportion of anhydrobiotic nematodes increases with the distance from stream sediments to drier soils [223].

Soil moisture measurement techniques have been recently reviewed by Babaeian et al. [50]. In general, there are two different approaches that use RS techniques to understand soil characteristics, their hydrological traits and eventually the spatial and temporal dynamics of soil moisture: (i) Direct measurements for areas where the soil has no or limited vegetation (using active and passive microwave sensors as well as optical RS data, Figure 7) and (ii) indirect measurements where vegetation covers the soil, using vegetation traits as a proxy of the soil and soil moisture traits. Optical RS data are preferred for indirect measurements of soil moisture patterns. In general, spaceborne RS of soil moisture is very advanced at global scales [51] with high accuracy [224] and a large variety of applications [225]. For local scales, adequate spatio-temporal resolutions are less common and tend to be the domain of airborne observations or proximal sensing, like cosmic ray neutron sensing [226] or ground penetrating RADAR [227,228].

4.2.1. Soil Moisture Characteristics using Active and Passive Microwave RS Approaches

Surface soil moisture estimation using microwave RS is based on the different dielectric properties (ϵ) of dry soil ($\epsilon \sim 4$) and liquid water ($\epsilon \sim 80$) [229]. However, extracting the part of the microwave signal that actually originates from the soil water is a challenging task. Not only sensor characteristics such as polarization, incidence angle, wavelength, and spatial as well as temporal resolution, but also surface characteristics such as vegetation cover with its shape, orientation, as well as water content and soil surface roughness have a distinct influence on the microwave signal that is received.

Both active and passive microwave systems are sensitive to the complex dielectric constant of the soil rather than to soil moisture directly. Here, soil dielectric mixing models have been developed for their linkage, e.g., by [230–232]. All models rely on the separate contribution of bound water and free water to compute the complex dielectric constant of the soil. The empirical approach by [230] has the advantage that it does not require information on soil texture, although it only appears to be satisfactory for coarse-textured soils. The semi-empirical approach by [231] is valid for a large range of microwave frequencies (1–18GHz), but is restricted to a certain range of soil textures. The Mironov approach [232] on the other hand is based on the refractive mixing model for moist soils. It is validated for a large range of soil textures and therefore suitable for global-scale applications (cf. SMOS [225] (Figure 7a) and SMAP [233] satellite missions).

4.2.2. Active Microwave Sensors (RADAR, Scatterometers)

Active microwave sensors (RADAR, scatterometers) send microwaves using their antenna devices and are therefore independent of illumination and weather [234]. Due to the active transmission, the strength of the signal is distinctively higher than that of passive microwave sensors (radiometers), which depend on the weak natural emission of the radiation from Earth. Hence, the recorded microwave signal is not directly prone to system noise or exposed to external radiation sources/interferences due to the strength of the active signal compared to passive devices. Moreover, the higher radiation budget of the recorded scattering at the active sensors also allows a shorter integration time and therefore a distinctively higher spatial resolution in terms of meters (in case of synthetic aperture RADAR, SAR) compared to the kilometer range for passive sensors. However, the calibration of the active sensors is much more complex with a transmitting and a receiving antenna part in contrast to passive devices.

Active sensors pick up the backscattered microwave radiation, normally measured in normalized backscattering coefficients or sigma noughts σ^0 (normalized RADAR cross sections), returning from interaction with media on Earth [235]. For soil moisture estimation from natural surfaces, the signal

recorded at the sensor is a mixture of scattering contributions. For bare soil surfaces, it is not only the dielectric constant (soil moisture), but also the soil roughness that influences the scattering of the microwaves depending on their strength [229]. The scattering scenario becomes more complicated with the occurrence of vegetation cover, where plant geometry, density, and moisture are influential factors on the scattering of the microwaves [236]. It is mainly a function of the wavelength as to how deep the microwaves can penetrate natural media. Hence, for soils with vegetation cover, longer wavelengths, such as L-band (23 cm), are preferred. This also enables soil moisture to be retrieved under vegetation cover [237] — at least until a certain density and wetness of the vegetation cover. In order to extract from the recorded backscattering signal, only the scattering component triggered by the moisture of the soil, decomposition methods are essential to invert soil moisture from the corresponding part of the signal. Polarimetry offers an exploitable observation space for the decomposition of RADAR measurements to invert for soil moisture [238–240].

Moreover, there are a plethora of algorithms for estimating soil moisture from active microwave RS, and a non-exhaustive overview is provided below [241–243]. The algorithms can mainly be divided into empirical (including machine-learning) [244–250], semi-empirical [251–254], and physical-based [229,255,256] retrieval techniques [237]. While empirical and semi-empirical algorithms can only be performed successfully in environments, where their empirical relationships were established, physical-based methodologies are generally valid and do not depend on test site characteristics. The inclusion of vegetation scattering comes with the selection of an appropriate model. Here, a range from more simple [257–259] to sophisticated [260,261] scattering models can be applied. However, the possibility of inversion decreases with the degree of complexity of the model due to an increase in variables for vegetation cover with a constant number of observations. Hence, the available observation space (multi-temporal, multi-angular, multi-frequency, multi-polarimetric) determines the complexity and performance of the inversion algorithm for soil moisture (under vegetation cover).

Beyond intensity- and polarimetry-based backscatter as well as machine-learning methods, another active microwave methodology to retrieve soil moisture dynamics in space and time is differential SAR interferometry (DInSAR). Ref. Morrison et al. [262–264] found significant dependence of the interferometric phase on changes in soil moisture. It was not possible to explain this relation by swelling soils and changes in penetration depth. The behavior of the phase points towards changes in volume scattering within the soil, which might also explain moisture-related temporal decorrelation [264].

At the global scale, a prominent active sensor system to estimate soil moisture is the advanced scatterometer on MetOp (ASCAT) [265,266]. Backscatter measurements at six different azimuth angles are used to calculate soil moisture by the change detection algorithm after Naeimi et al. [267]. The angular information is used to characterize the vegetation contribution and its temporal variability to be eliminated before soil moisture inversion. In contrast to this 12.5 km posting product, a 1 km product is available from Sentinel-1 [268] or a combined ASCAT-Sentinel-1 approach [269]. It has to be noted that the data are expressed in relative units (degree of saturation).

4.2.3. Passive Microwave Sensors

Passive microwave sensors (radiometers) record naturally emitted microwave radiation, usually expressed in brightness temperatures (T_b), i.e., the product of emissivity (ϵ) and the physical temperature of the target (T). This implies that the physical temperature of the target needs to be known for soil moisture retrieval. The emissivity of a smooth surface can be predicted by the Fresnel reflection equations. Accordingly, it depends on the incidence angle and the complex dielectric constant of a soil. Rough soils behave differently, because roughness decreases the reflectivity and thus increases emissivity. In theory, with an increased surface area, rough targets can emit more thermal energy. In field applications, the effective soil roughness is probably more related to the distribution of water in the topsoil rather than a pure geometric soil surface roughness as the latter can only occur when the soil is very wet. In addition to the general problematic consideration of the incidence angles within one radiometer footprint, this issue affects the soil moisture retrieval, especially in mountainous areas and needs to be accounted for in the retrieval methodology.

Another factor causing attenuation of the microwave emission is vegetation. Moreover, vegetation adds its contribution to the land surface emission signal [270]. To simulate these effects, a simple approach referred to as the τ - ω model [271], was developed. The τ - ω model is a zero-order solution of the radiative transfer equation [272] and uses only two variables for canopy characterization — the vegetation optical depth (VOD) τ and the single-scattering albedo ω . While the first one parameterizes the attenuation effects, the latter one describes the scattering effects within the canopy [273]. The optical depth is often linearly related to vegetation water content (VWC), [274] and can to a certain extent be derived from leaf area index or multispectral vegetation indices [275]. At L-band, soil moisture retrieval is only possible up to VWC of 5 kg/m² [276]. In addition, to the sole and direct relationships of plant biodiversity with soil moisture patterns, vegetation is additionally involved in soil moisture retrieval. This additional component needs to be separated when soil moisture and biodiversity dependencies should be investigated exclusively.

There are several approaches for soil moisture inversion and most of them are based on the vegetation attenuation concept of Mo et al. [271] e.g., the normalized polarization difference (NPD) algorithm, the single-channel algorithm (SCA), the L-band microwave emission of the biosphere (L-MEB) model, the community microwave emission model (CMEM), the land parameter retrieval model (LPRM), and the University of Montana (UMT) approach [277–279]. It is worth noting that spaceborne brightness temperature products are typically only valid for the top-of-atmosphere (except for the SMAP products). To estimate surface level brightness temperatures before soil moisture inversion, atmosphere attenuation, upward atmosphere emissivity, and the polarization rotation according to the Faraday theory need to be considered.

Global scale soil moisture monitoring is provided by the Japan Aerospace Exploration Agency (JAXA) Global Change Observation Mission-1st Water (GCOM-W1) satellite that hosts the AMSR2 sensor [280]. Together with its precursor AMSR-E, the time series, with a gap of a few months, expands from mid-2002 until present. Further systems are the soil moisture and ocean salinity (SMOS) [281] and soil moisture active and passive (SMAP) missions [233,282], started in 2009 and 2015, respectively.

4.2.4. Combining Active and Passive Microwave Sensors

For the long-term analysis of surface soil moisture within the water and energy feedbacks of the climate system, large time series were generated and developed. The ESA Climate Change Initiative (CCI) combines active and passive microwave observations to obtain a consistent time series from 1978 until mid-2018 [283]. According to their suitability for soil moisture retrieval, C-band scatterometers (ERS-1/2 scatterometer, ASCAT) and multi-frequency radiometers (SMMR, SSM/I, TMI, AMSR-E, Windsat) were merged at the level of retrieved surface soil moisture data (Level 2) to avoid problems arising from different sensor specifications.

With the launch of NASA's missions Aquarius and SMAP, both active and passive microwave remote-sensing observations are combined to improve the spatial resolution [284]. The combination extracts the relative advantages of the two sensing techniques, as there is a tradeoff between resolution and soil moisture sensing sensitivity between active and passive microwave measurements [285]. Fusion methods include temporal change detection methods [286], Bayesian merging approaches [287], statistical disaggregation [285,288,289], and physics-based covariation algorithms [290–292]. Other methods retrieve vegetation variables from active microwave measurements for the utilization of passive microwave soil moisture inversion [293,294]. Unfortunately, the RADAR on the SMAP satellite went out of service on 7 July 2015. Therefore, combined active–passive microwave data were only recorded over the first months of the mission (April–July 2015). Due to the failure of SMAP's L-band RADAR, the substitution with ESA Copernicus Sentinel-1's C-band RADAR is in final preparation [295] and a first 3 km soil moisture product was released in November 2017 [295]. Due to Sentinel-1's varying acquisition geometry and the reduced amount of coincident active-passive overpasses, the standard statistical (time-series) downscaling approach using passive brightness temperatures with active RADAR backscatter is no longer possible and a physics-based downscaling was developed by [295,296] for a dual-frequency downscaling.

Moreover, soil moisture sensing is also a topic of discussion for airborne microwave RS working on resolutions that are valid for habitat research and precision farming and capable of retrieving soil moisture patterns with a high spatial resolution (<100 m). On airborne platforms joint active–passive remote-sensing instrument constellations include PLMR (polarimetric L-band multibeam radiometer) [178,297,298] (Figure 7c) and F-SAR sensors [299,300] (Figure 7d), also referred to as multi-sensor platforms.

With these multi-sensor platforms, [301] analyzed different active–passive fusion methods and their advantages and drawbacks for a central European region. In Australia, the SMAPEX campaigns (e.g., [302]) provided first combined observations of PLMR and PLIS (polarimetric L-band imaging synthetic aperture RADAR). In North America, the PALS (passive and active L- and S-band sensor; [303]) recorded soil moisture from RADAR and radiometer to analyze soil moisture heterogeneity across scales in several campaigns. Table 5 provides an overview of recent satellite missions and airborne systems for soil moisture estimation. With these sensors, soil moisture retrieval is only possible for the top few cm of the soil surface, namely the surface soil moisture. Root zone soil moisture, which to a larger extent effects the biodiversity of a habitat rather than the water content of the top layer, can be estimated by additional methods. Examples are: Direct retrieval by longer wavelengths such as P-band [304], surface soil moisture assimilation into a hydrological model [305–310], or data-driven methods such as neural networks [311] to improve root zone soil moisture estimates. Moreover, indirect methods use the plants as “sensors” of root-zone properties. Wilson [312] can therefore be used to gain knowledge about root zone soil conditions (see also Chapter 4.3.5) and Rudolph [313], for example, presented the link between crop-status patterns in large-scale multispectral satellite imagery with multi-receiver electromagnetic induction (EMI) hydro-geophysical data.

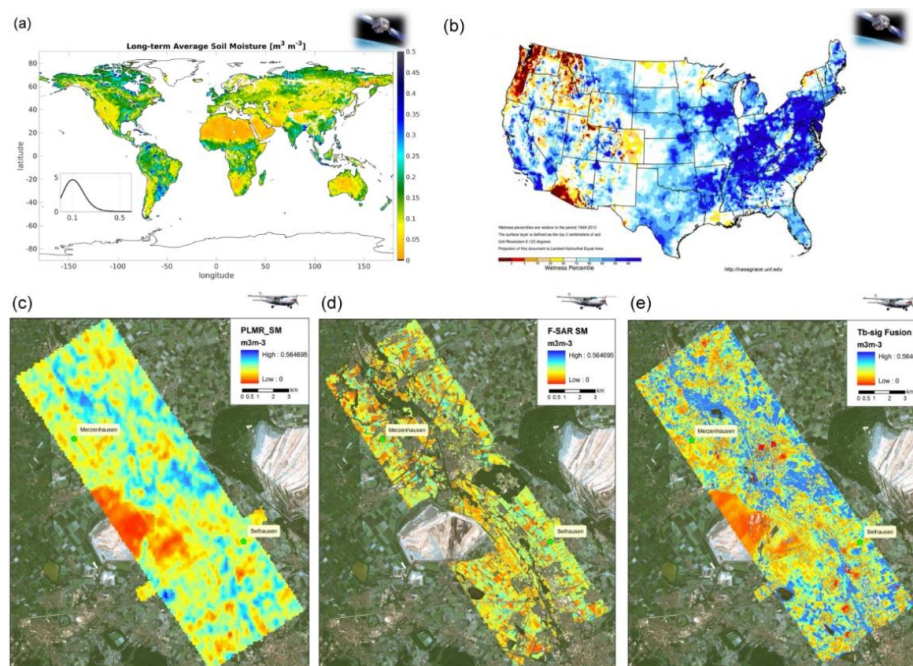


Figure 7. Soil moisture patterns and indicators derived from (a) soil moisture and ocean salinity mission (SMOS; from Piles et al. [314]), (b) NASA’s gravity recovery and climate experiment (GRACE) satellites (https://nasagrace.unl.edu/data/20190506/GRACE_SFSM_20190506.png), (c) low-resolution passive microwave, (d) high-resolution active microwave, and (e) medium-resolution (combined) active-passive microwave (brightness temperature disaggregation) observations of the multi-sensor platform (PLMR and F-SAR) for the agricultural and mining region around Jülich, Germany (modified after Montzka et al. [301]).

4.2.5. Direct and Indirect Measurements by Optical and Thermal Sensors

To obtain and assess the direct approaches to assess spatial and multitemporal surface soil moisture data, in addition to microwave RS techniques, there are also various optical sensors such as MODIS [315], Landsat [316], hyperspectral RS sensors (HyMap, [317]), as well as thermal infrared sensors (Landsat, Sentinel-3, or SEVIRI [318], Table 2). Since soil moisture is subject to a very high spatial-temporal variability, the suitability of optical and thermal sensors to derive soil moisture related information very much depends on the spatial, spectral, and temporal resolution of the RS sensors. Furthermore, soil moisture is a very dynamic parameter along the soil profile, and passive and active RS sensors can sense soil moisture at different depths. In addition, to the sensor characteristics, an extensive acquisition of in-situ data on soil moisture is also required. Such in-situ measurements (previously conducted manually using close-range sensors) are often insufficient due to the tremendous spatial and temporal variability of RS data. To gain access to in-situ data with a high temporal and spatial resolution as well as to soil moisture data from different locations with differentiated land-use-land-cover and soil characteristics, the development and implementation of distributed soil moisture sensor networks is imperative to achieve an improved calibration and validation of air- and spaceborne RS data. Some promising preliminary approaches have already been made in this respect [319].

Soil moisture is difficult to determine in most European regions using the direct approach with active and passive microwave and optical sensors, because the soil is mostly covered with vegetation that varies in height, density, and plant species composition over the entire year [100]. Therefore, vegetation and its biochemical, morphological, physiological, or functional characteristics of plants or spectral plant traits are used as a proxy for determining soil moisture patterns and soil characteristics in space and time [100] (see also Figure 8).

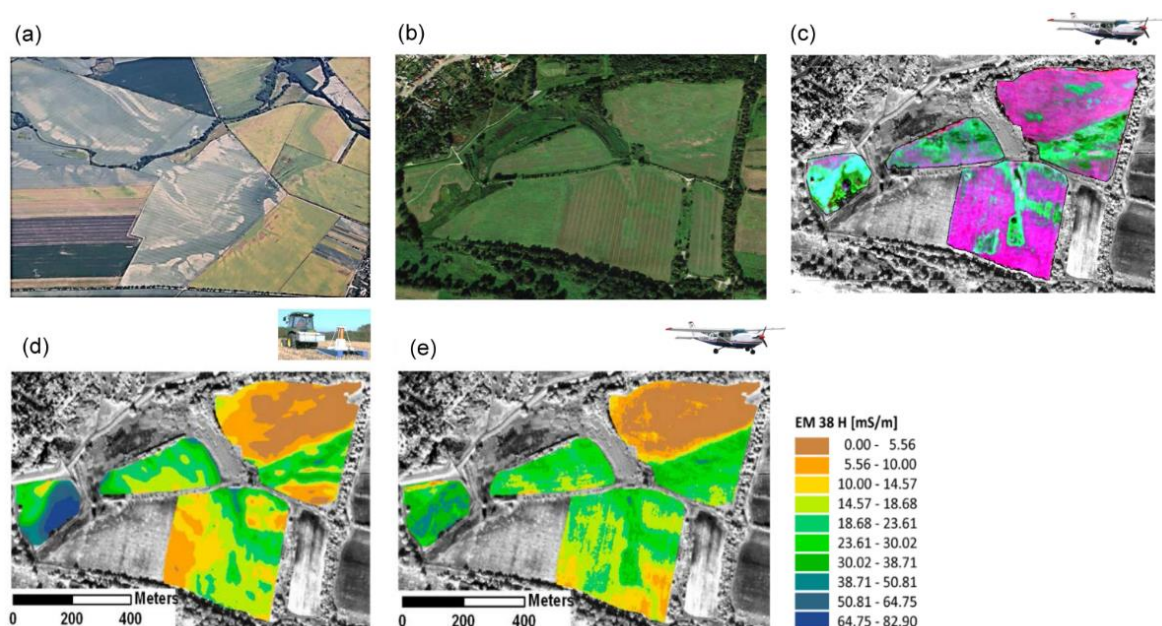


Figure 8. Soil moisture patterns—optical RS. (a) Vegetation patterns as a proxy for soil conditions and soil characteristics, photographs taken near Koethen-Wulfen, (b) study area “Rosslauer Oberluch”, Germany, (c) color Infrared image (CIR) taken from the hyperspectral sensor AISA-EAGLE/HAWK (DUAL), 0.40–2.5 μm spectral resolution, 2 m ground resolution, 461 spectral bands, date of recording 23 September 2010 with a Cessna 207, (d) measured electrical conductivity—EM38DD H with measurement arrangement of gamma-ray spectrometer and EM38DD with a tractor, (e) predicted electrical conductivity—EM38DD H with hyperspectral sensor AISA-EAGLE/HAWK (DUAL) (modified after Lausch et al. [100]).

4.2.6. Airborne Geophysical Sensors of Natural Radiation-Gamma and Cosmic-Ray Neutron Sensors

Natural sources of radioactivity or cosmogenic radiation are increasingly used in environmental sciences for the spatial exploration of soil properties. While the space-borne detection of gamma and albedo-neutron radiation from satellites became a standard method to map the soil water distribution on Mars [320], the Earth's atmosphere allows for the detection of terrestrial radiation only with car-borne or low-flying airborne vehicles. Nevertheless, the much deeper soil penetration and the effortless installation are the main advantages of gamma and neutron sensing compared to optical techniques.

Sources of gamma radiation are radioactive isotopes in the ground, such as potassium-40, thorium-232, and their daughters in the decay chain. Their signal is attenuated by any material, but particularly by the water molecule. The gamma rays of the corresponding energy window can travel up to 30 cm in the ground and 25 m in the air [321]. Hence, gamma radiation can be a proxy for the average soil water content in the upper root zone [227]. However, the distribution of potassium and thorium in the soil is highly variable, and the signal attenuation depends on soil chemistry. The corresponding variability dominates over the relatively subtle dependence on soil moisture [322]. Therefore, spatial estimation of soil texture is the main application of gamma-ray surveys [323–325], while the estimation of soil or snow water relies on known reference data (i.e., background radiation) of the study region [326,327].

Cosmic-ray neutrons are part of the omnipresent background radiation on Earth. In contrast to electro-magnetic signals, neutrons do not interact with the electric fields of atoms, allowing them to penetrate deeply into materials [328]. In the soil, neutrons collide with atomic nuclei and reflect back to the atmosphere. Since neutrons are extraordinarily sensitive to the lightweight nucleus of the hydrogen atom, the reflected (or albedo) component of neutrons above ground depends inversely on the soil water content [329]. Consequently, neutrons are also sensitive to other sources of hydrogen, such as biomass and snow [330,331]. However, the target geometry does not play a role at all, such as terrain roughness and or leaf orientation, which can be an issue for electro-magnetic/optical remote sensing.

The neutrons penetrate the soil down to 15 cm (for wet) or 70 cm (for dry soils) and thereby sample the highly relevant “root zone” [328]. In air, neutrons can travel hundreds of meters before detection and thereby act as a proxy for the average water content within 10–20 hectares. This so-called footprint area increases with increasing terrestrial altitude and also with the detector height above ground. Due to their random-walk nature, neutrons enter the detector mostly isotropically, where the collisions with the detector gas induce countable electrical pulses [332]. Due to the isotropic nature and the fact that neutrons are almost insensitive to most materials other than hydrogen, the detector can be mounted effortlessly on or in a vehicle irrespective of configuration, orientation, viewing angle, or window.

In the last couple of years, soil moisture measurements with cosmic-ray neutrons have been conducted using stationary sensors or car-borne sensors (“rovers”), which are, however, limited to accessible terrain [240,333,334]. Very recent developments by Schrön [335] pioneered the application of airborne neutron sensing. First campaigns made use of a gyrocopter and in-situ data in areas of various land use types including agricultural fields, urban areas, forests, flood plains, and lakes (Figure 9b). The study indicated that neutrons are sensitive to soil water variability in heights of up to 200 m above ground. Both gamma and neutron methods rely on a high signal-to-noise ratio, which increases with detector volume and decreases with height above ground. Hence, ongoing developments are aiming for airborne technologies with high payload and low flying altitude. The proof of concept indicated a high potential of airborne neutron sensing, which could become a valuable addition — or even an alternative — to conventional remote-sensing methods. Moreover, cosmic-ray neutron data can also be used to ground-truth remote-sensing products [336,337], or in synergy with airborne PolSAR to correct the cosmic-ray soil moisture product for the influence of biomass [240].

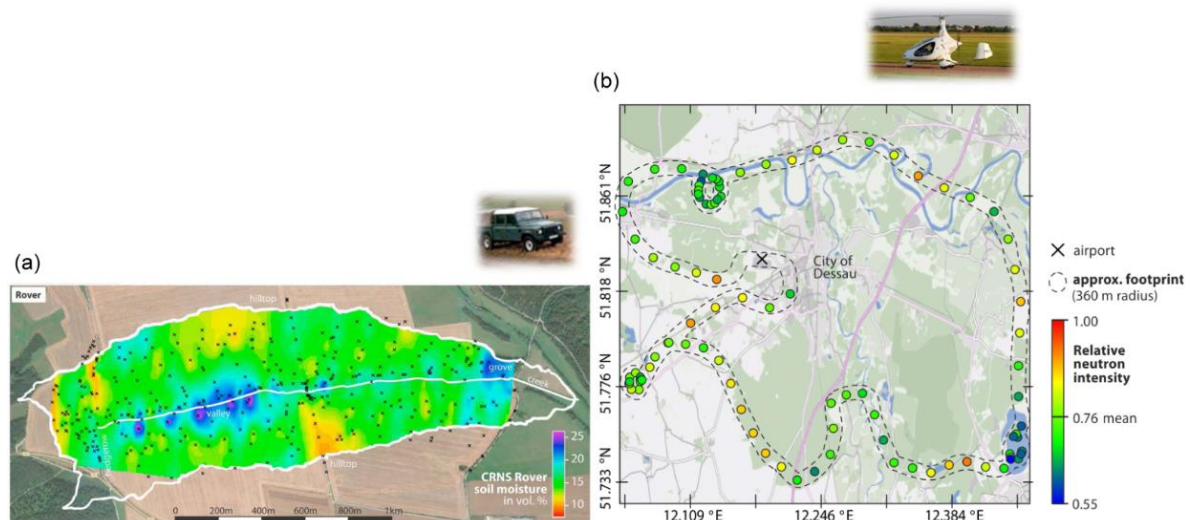


Figure 9. (a) Soil moisture estimation by the cosmic-ray neutron sensor (CRNS) rover in the Schäferfald agricultural field (from Schrön et al. [334]). (b) Measurement campaign in the Elbe-Mulde region around the City of Dessau (Germany) using detectors for cosmic-ray neutron albedo mounted on a gyrocopter. The aircraft operated at heights around 200 m above ground and circulated multiple times at certain points of interest (the floodplain, an agricultural field, the lake). Apparent measurement locations show collected neutron data over the course of 1 min. The footprint area in which 86% of measured neutrons were soil contact is indicated as a dashed rope (modified after Schrön [335]).

Table 5. RS-aided derived traits of soil moisture.

Mission/Sensor/Platform	Name	Spectral Resolution Spectral Bands/Frequency	Reference
UAV ¹			
Airborne ²			
Spaceborne ³			
Soil moisture estimation for bare soil to sparse vegetation conditions			
Active and passive microwave sensors			
SMAP ³	Radiometer	1.41 GHz	[233]
	RADAR	1.26 GHz	[233]
SMOS ³	MIRAS	1.4 GHz	[276,314,338,339]
ALOS-2 ³	PALSAR-2	1.3 GHz	[340]
GCOM ³	AMSR2	6.9 GHz	[341]
Coriolis ³	Windsat	6.8 GHz	[342]
MetOp ³	ASCAT	5.3 GHz	[343]
RADARSAT2 ³	SAR	5.3 GHz	[344]
RISAT ³	Compact-SAR	5.35 GHz	[345]
Sentinel-1 ³	SAR	5.3 GHz	[346]
TerraSAR-X/TanDEM-X ³	SAR	9.63 GHz	[347–349]
PLMR ²	L-band microwave radiometer	2.4 GHz	[178,275,297,298,350–352]
PALS ²	Radiometer	1.41 and 2.69 GHz	[353]
	RADAR	1.26 and 3.15 GHz	
PLIS ²	RADAR	1.26 GHz	[302]
FSAR ²	RADAR	9.60 GHz, 5.30 GHz, 3.25 GHz, 1.325 GHz, and 0.435 GHz	[299] Horn et al., 2018
Other geophysical methods-passive radiation techniques			
Cosmic-ray neutron sensing ²	Natural neutron radiation	1–1000 eV	[335]
Gamma-ray surveys ²	Natural gamma radiation	⁴⁰ K, ²⁰⁸ Tl (0.4–3.0 MeV)	[326]

Table 5. Cont.

Mission/Sensor/Platform UAV ¹ Airborne ² Spaceborne ³	Name	Spectral Resolution Spectral Bands/Frequency	Reference
Optical remote sensing sensors			
Terra/Aqua MODIS ³	Multispectral/TIR	0.41–14.40 μm/ 36	[315,354]
Landsat 5 TM ³ Landsat 7 ETM+ ³	Multispectral/TIR	0.45–2.3 μm/6 10.4–12.5 μm/1	[316,355]
Landsat 8 OLI/TIRS ³	Multispectral/TIR	0.43–2.3 μm/8 10.6–12.51 μm/2	[356]
Terra ASTER ³	Multispectral/TIR	0.52–9.2 μm/9 8.12–11.65 μm/5	[357]
Meteosat II SEVIRI ³	Multispectral/TIR	0.48–7.6μm/8 8.5–13.9 μm/5	[318]
Sentinel-2 MSI ³	Multispectral	0.40–3.0 μm/13	[358]
APEX ²	Hyperspectral	0.38–2.50 μm /~125	[126]
HyMAP ²	Hyperspectral	0.45–2.48 μm/~125	[123,317,359]
DAIS-7915 ²	Hyperspectral	0.40–2.50 μm/72	[130]
AHS ²	Hyperspectral	0.43–12.7 μm/~ 80	[357]
Cubert UHD 185 ¹	Hyperspectral	0.45–0.95 μm/~125	[136]
Soil moisture and soil characteristics estimation using plant proxy information			
Landsat 4 MSS ³ , Landsat 5 TM ³ ; Landsat 7 ETM+ ³ , Landsat 8 OLI/TIRS ³ , Sentinel-1 ³ , Sentinel-2 MSI ³	Multispectral/TIR/SAR		[360]
RapidEye REIS ³	Multispectral	0.40–1.3 μm/5	[144]
AisaDUAL ²	Hyperspectral	0.40–2.45 μm /~200–400	[100]

* SMAP RADAR stopped operation on 7 July 2015. Sensor is used on the RS platform: UAV¹ - unmanned aerial vehicles (UAV); airborne² – airborne RS platform; spaceborne³ – spaceborne RS platform.

The RS-aided derivation of geotraits of soil moisture is shown in Table 5. Figure 10 shows the enormous number of current and future space-based RS missions and satellites for monitoring soil moisture with information about the mission status, according to the CEOS database [205].

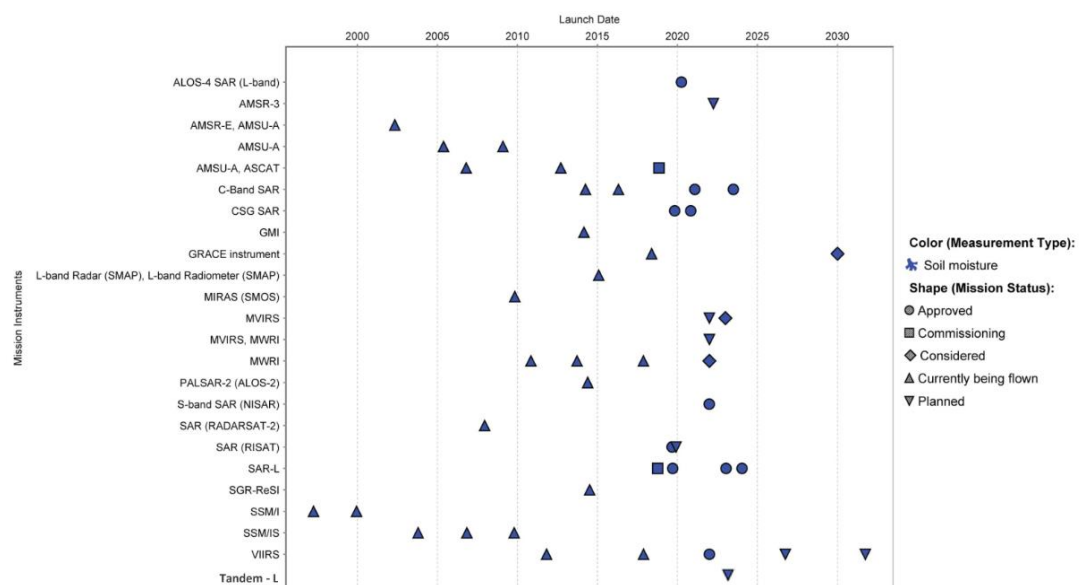


Figure 10. Current and future RS missions instruments for monitoring soil moisture with information about the mission status, extracted from the CEOS database [205].

A selection of RS-aided data products for deriving soil moisture by RS is shown in Table 6.

Table 6. Selection of RS-aided data products of soil moisture estimation with RS.

Data Products	Scale	Link	References
NASA-Soil Moisture Products	Global/ Regional	https://lpvs.gsfc.nasa.gov/SM/SM_home.html	NA
International Soil Moisture Network		https://ismn.geo.tuwien.ac.at/en/	[361]
Rapid Mapping (on demand): Drought	Affected Countries	https://emergency.copernicus.eu/mapping/list-of-activations-rapid	NA
European Drought Observatory (EDO) Combined Drought Indicator	Europe	https://www.eea.europa.eu/policy-documents/european-drought-observatory-edo http://edo.jrc.ec.europa.eu/edov2/php/index.php?id=1000	NA
Global Drought Observatory (GDO) Global Drought	Global	http://edo.jrc.ec.europa.eu/gdo/php/index.php?id=2000	NA
NASA-USDA SMAP Global Soil Moisture Data	Global	https://developers.google.com/earth-engine/datasets/catalog/NASA_USDA_HSL_SMAP_soil_moisture	NA
NOAA Soil Moisture Products System (SMOPS) Daily Blended Products	Global	https://data.nodc.noaa.gov/cgi-bin/iso?id=gov.noaa.ncdc:C00994	NA
SMAP/Sentinel-1 L2 Radiometer/RADAR 3 km	Global	https://nsidc.org/data/SPL2SMAP_S/versions/2	[362]
SMAP Enhanced L3 Radiometer Global Daily 9 km	Global	https://nsidc.org/data/SPL3SMP_E/versions/2	[363]
SMOS Level 3 daily soil moisture and brightness temperature maps	Global	https://www.catds.fr/sipad/	[364]
Metop ASCAT SSM time series	Global	http://hsaf.meteoam.it	[266]
Global Land Data Assimilation System (GLDAS)	Global	https://grace.jpl.nasa.gov/data/get-data/land-water-content/	[365]
GRACE-Platform NASA's Gravity Recovery and Climate Experiment (GRACE) satellites	Global/ Regional	https://grace.jpl.nasa.gov/data/get-data/ https://nasagrace.unl.edu/Default.aspx	[366]

4.2.7. Surface and Soil Moisture Characterization by Land Surface Temperature RS Approach

Land surface temperature (LST) is one of the most important state variables representing the coupled interaction of the surface energy and water balance and represents a valuable source of information for ecological and hydrological modeling from the local to the global scale [367–369]. The knowledge of LST provides crucial understanding of spatio-temporal variations of the surface equilibrium state [370] and is helpful in exploring and modelling plant–environment interactions [371]. LST is highly influenced by the radiative, thermal, and hydraulic properties of the soil–plant–atmosphere system and has therefore been recognized as one of the high-priority variables of the International Geosphere and Biosphere Program (IGBP) [372].

LST is used in various research contexts such as urban ecology like monitoring plant and human health during heat waves [373], for the description of the hydrological cycle, in climate research, or in studies of vegetation dynamics [374,375]. Furthermore, LST is often used to estimate evapotranspiration [369,376–378], which is a variable that is highly controlled by atmospheric conditions, but also by stomata conductance, the plant available, the soil moisture, and processes of the surface–subsurface interactions [379]. In this sense, the monitoring of LST with high spatial and temporal resolution can provide valuable information about the water and energy exchange between the soil–plant–atmosphere continuum as well as related photosynthetic activities of the vegetation. Differences in the spatio-temporal behavior of LST can therefore be related to different plant species distributions, to differences related to the local energy, water, or nutrient conditions [380], and can even be used to improve the classification of soil texture data [181]. LST is also strongly influenced by the patterns and heterogeneity of vegetation and land surface characteristics such as soil, topography, and vegetation [381]. Therefore, the recording of surface characteristics and their heterogeneity by using RS is important for being able to adequately describe, explain, and predict LST distribution.

While LST is easily measured by thermometers at the point scale, RS thermal infrared data (TIR) are needed to derive LST routinely at high temporal and spatial resolutions over large spatial extents. However, the derivation of LST from TIR data is a difficult task for the following reasons: The

radiance measurements on board the satellites not only depend on LST, but also surface emissivity and atmospheric conditions [382]. Therefore, besides cloud detection and radiometric calibration, corrections for emissivity and atmospheric effects have to be carried out. A large number of studies have addressed these issues and many of them are described in the review by Li et al. [370].

To quantify the landscape surface energy balance, there are various in-situ measurements of surface fluxes at the canopy level. Such in-situ measurements are very valuable, but they are only representative for small areas. It is therefore difficult and costly to investigate the detailed spatial pattern of energy fluxes over entire areas. TIR data can therefore be used to derive the LST of different surfaces. Hitherto, a range of airborne and satellite sensors were developed to record TIR image data i.e., Landsat TM/ETM+, MODIS, ASTER, and new satellites such as the HypsIRI that are under development

Given a large number of influences on LST, airborne platforms [21] and UAV [383,384] are in use for the retrieval of LST. RS platforms and sensors currently providing TIR data differ in the spatial, spectral, and temporal resolution of LST data and are the only way to measure LST from the local to the global scale with high spatial and temporal resolution (see also Figure 11 and Table 7).

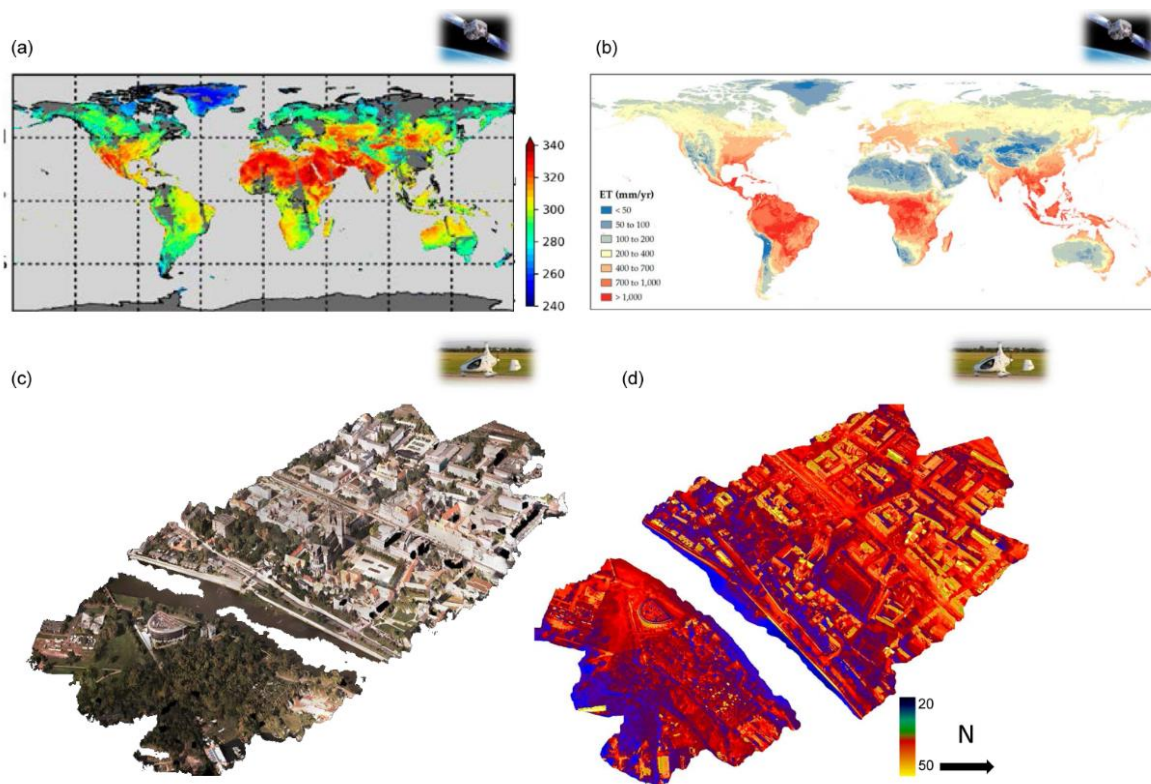


Figure 11. Land surface temperature and related traits: (a) Daytime land surface temperature (LST) composite. Derived from Aqua MODIS RS data for 1 June 2010 (from Ghent et al. [385]), (b) daily global evapotranspiration using Menman–Ponteith equation and remotely sensed land surface temperature (Raouf and Beighley, [386]). (c) Near 3D-True-Ortho-RGB image of Magdeburg (City Centre) RGB image, (d) 3D-TIR image based on the Aerial Oblique System [AOS-Tx8] with 8 cameras (4 cameras FLIR A65 SC, 4 RGB cameras Baumer VC XG-53c) rendered as a 3D TIR image of Magdeburg. (c,d) were taken by Prof. Lutz Bannehr, Department of Architecture, Facility Management and Geoinformation, Institute for Geoinformation and Surveying, Dessau, Germany.

Table 7. RS-aided derivation traits of land surface temperature estimation and soil moisture characterization by thermal infrared (TIR) RS approaches.

Mission/Sensor/ Platform UAV ¹ Airborne ² Spaceborne ³	Sensor Type	Spectral Resolution Spectral Bands/Frequency	Spatial Resolution [m]	References
Land surface temperature (LST)				
Terra/Aqua MODIS ³	Multispectral/TIR	0.41–14.40 μm /36	250/500/1000	[21,387,388]
Landsat 5 TM ³ Landsat 7 ETM+ ³	Multispectral/TIR	0.45–2.3 μm /6 10.4–12.5 μm /1	L5:30/120 L7:30/60	[389,390]
Landsat 8 OLI/TIRS ³	Multispectral/TIR	0.43–2.3 μm /8 10.6–12.51 μm /2	30/100	[356,391]
NOAA/MetOp AVHRR ³	Multispectral/TIR	0.58–3.93 μm /4 10.3–12.5 μm /2	1100	[392,393]
Terra ASTER ³	Multispectral/TIR	0.52–9.2 μm /9 8.12–11.65 μm /5	30/90	[388,394]
Sentinel-3 OLCI/SLSTR ³	Multispectral/TIR	0.4–1.02 μm /21 0.55–12.0 μm /9	300/1000	[395]
MSG (Meteosat Second Generation) SEVERI/GERB ³	Multispectral/TIR	3.4–12.0 μm /8	3000	[396,397]
GEOS 17 (Geostationary Operational Environmental Satellites) ABI ³	Multispectral/TIR	0.45–2.27 μm /6 3.8–13.56 μm /10	4000	[21,398]
AHS ²	Hyperspectral	0.43–12.7 μm /~80	~ 2	[399]
Heitronics IR Pyrometer ²	Pyrometer	9.6 and 11.5 μm	16 m (Radius)	[21]
Q300, QuestUAV, UK ¹	TIR	7.5–13 μm	~ 0.13 m	[383]
ThermalCapture 2.0 640 thermal camera (TeAx, Wilnsdorf, Germany) ¹	TIR	7.5–13.5 μm	NA	[384]
RGB-compact digital camera (Samsung ES80)/Optris Pi 400 ¹	RGB/TIR	7.5–13 μm	1–5 cm	[377]
Land surface emissivity (LSE)				
Meteosat II/SEVIRI ³	Multispectral/TIR	0.48–7.6 μm /8 8.5–13.9 μm /5	NA	[318]
Telops HYPER-CAM ²	Hyperspectral TIR	1.5–5.5 μm 8–11.5 μm	NA	[400,401]
RGB-compact digital camera (Samsung ES80)/Optris Pi 400 ¹	RGB/TIR	7.13 μm	1–5 cm	[377]
Evapotranspiration				
MODIS Aqua SST ³	Multispectral/TIR	3.66–4.08 μm /4 10.78–12.27 μm /2	1000	[385]
Terra ASTER ³	Multispectral/TIR	0.52–9.2 μm /9 8.12–11.65 μm /5	30/90	[402]
Landsat 5 TM ³	Multispectral/TIR	0.45–12.5 μm /8	L5:30/120	[403]
Landsat 7 ETM+ ³	Multispectral/TIR	0.45–12.5 μm /8	30/60	[404]
Q300, QuestUAV, UK ¹	TIR	7.5–13 μm	~0.13	[383]
Optris Pi Lightweight kit, Optris GmbH, Germany ¹	RGB/TIR	7.5–13 μm	1–5 cm	[377]
RGB-Samsung ES80)/Optris Pi 400 ¹	RGB/TIR	7.5–13 μm	1–5 cm	[377]
Heat fluxes				
RGB-Samsung ES80)/Optris Pi 400 ¹	RGB/TIR	7.5–13 μm	1–5 cm	[377]

Sensor is used on the RS platform: UAV ¹ - unmanned aerial vehicles (UAV); airborne ² – airborne RS platform; spaceborne ³ – spaceborne RS platform.

The RS-aided derivation of traits of LST and related traits is shown in Table 7. Figure 12 shows the enormous number of current and future space-based RS missions and satellites for monitoring LST with information about the mission status, according to the CEOS database [205].

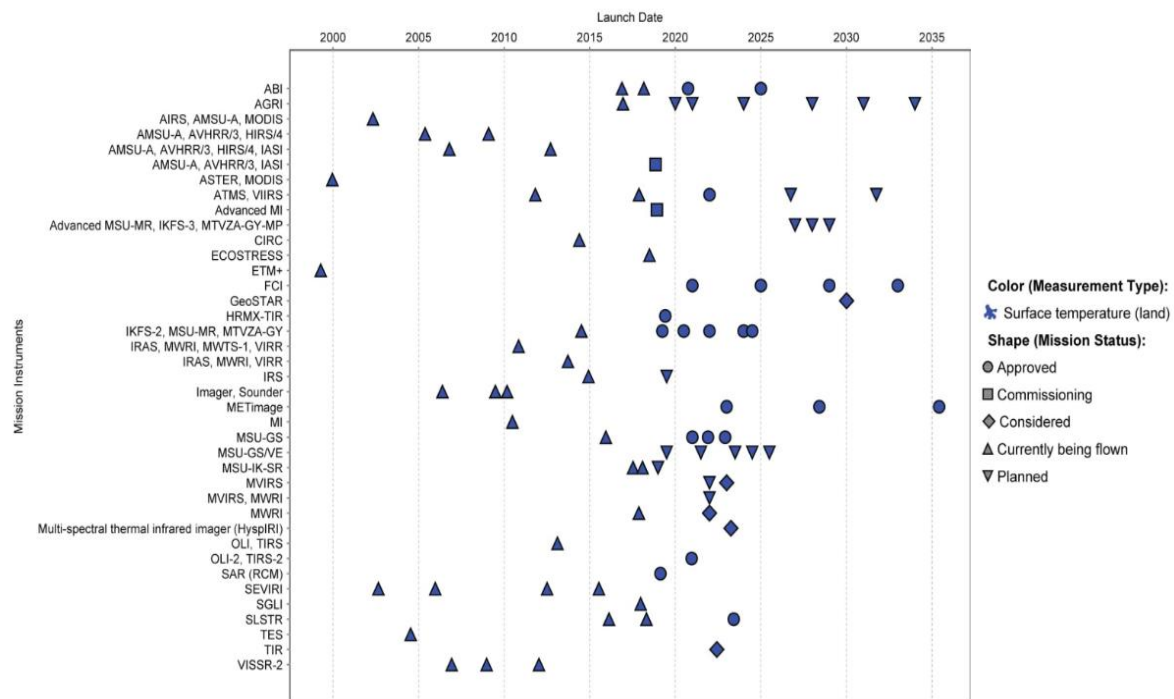


Figure 12. Current and future spaceborne RS missions and satellites for monitoring land surface temperature with information about the mission status, information by the CEOS database [205].

A selection of RS-aided data products for deriving LST from RS is shown in Table 8.

Table 8. Selection of RS-aided data products of land surface temperature and related variables.

Data Products	Scale	Link	References
NASA-Land Surface Temperature & Emissivity Products	Global/Regional	https://lpvs.gsfc.nasa.gov/LSTE/LSTE_home.html	NA
Landsat and Surface Temperature Land Surface Temperature True Land Surface Albedo	Global	http://rslab.gr/downloads.html http://rslab.gr/downloads_LandsatLST.html	[405]
GLS Surface Reflectance	Global	http://www.landcover.org/data/gls_SR/	[406]
Downward Shortwave Surface Radiation (DSSR)	Global	http://www.landcover.org/data/dssr/	[407]
Tropospheric Emission Monitoring Internet Service	Global	http://www.temis.nl/index.php	NA
Land-Surface Temperature	Global	https://land.copernicus.eu/product-portfolio/overview	NA
Surface Albedo	Global	https://land.copernicus.eu/product-portfolio/overview	NA
Lake Surface Water Temperature	Global	https://grace.jpl.nasa.gov/data/get-data/land-water-content/ https://ldas.gsfc.nasa.gov/	NA
Global Land Data Assimilation System (GLDAS)	Global	https://grace.jpl.nasa.gov/data/get-data/land-water-content/ https://ldas.gsfc.nasa.gov/	[365]

5. Conclusions and Further Requirements in Monitoring Geodiversity

In order to understand the complexity, processes, disturbances, and resilience of biodiversity, it is imperative to gain a deep understanding of the status, stress-induced changes, disturbances, and resource limitations for geodiversity and traits as well as their interactions and feedbacks with above-and below-ground biodiversity.

Geodiversity and its five essential characteristics, a novel concept for the first time defined in this paper, and the definitions of traits and trait variations were introduced. Geodiversity and its traits (geotraits) can be recorded by in-situ and RS-techniques. In-situ techniques are accurate, largely point-based, but are more time-consuming and can only be repeated with considerable personnel and financial means. RS techniques on the other hand are a cost-effective alternative that are becoming

increasingly more accessible, comprehensive, and repeatable, while providing the opportunity for a standardized recording of continuous geodiversity and trait variables. Geo-traits exist on all spatio-temporal scales and can thus be monitored by RS sensors on different platforms.

This paper presents the state-of-the-art in monitoring geodiversity and its traits using air- and spaceborne RS of soil characteristics including soil moisture. RADAR, LiDAR, thermal sensors, multispectral, hyperspectral, and microwave RS technologies that record soil characteristics including soil moisture are presented. Furthermore, the paper discusses future satellites and existing data products that are suitable for monitoring geodiversity and its traits.

As a physical-based system, RS can monitor geodiversity and its traits (depending on the RS characteristics and composition and configuration of traits [1,3]) by using the spectral traits (ST) as well as the spectral traits variations (STV) approach. Consequently, the RS approach is then referred to as the remote sensing–spectral traits/spectral trait variations–concept–RS-ST/STV-C.

Unlike in-situ techniques, RS approaches can only record specific geo-traits/trait combinations and trait variations due to the different RS characteristics (spectral, radiometric, geometric, directional, and temporal). This paper provides an overview of those traits and trait variations that can be recorded by air- and spaceborne RS techniques (see Figure 13).

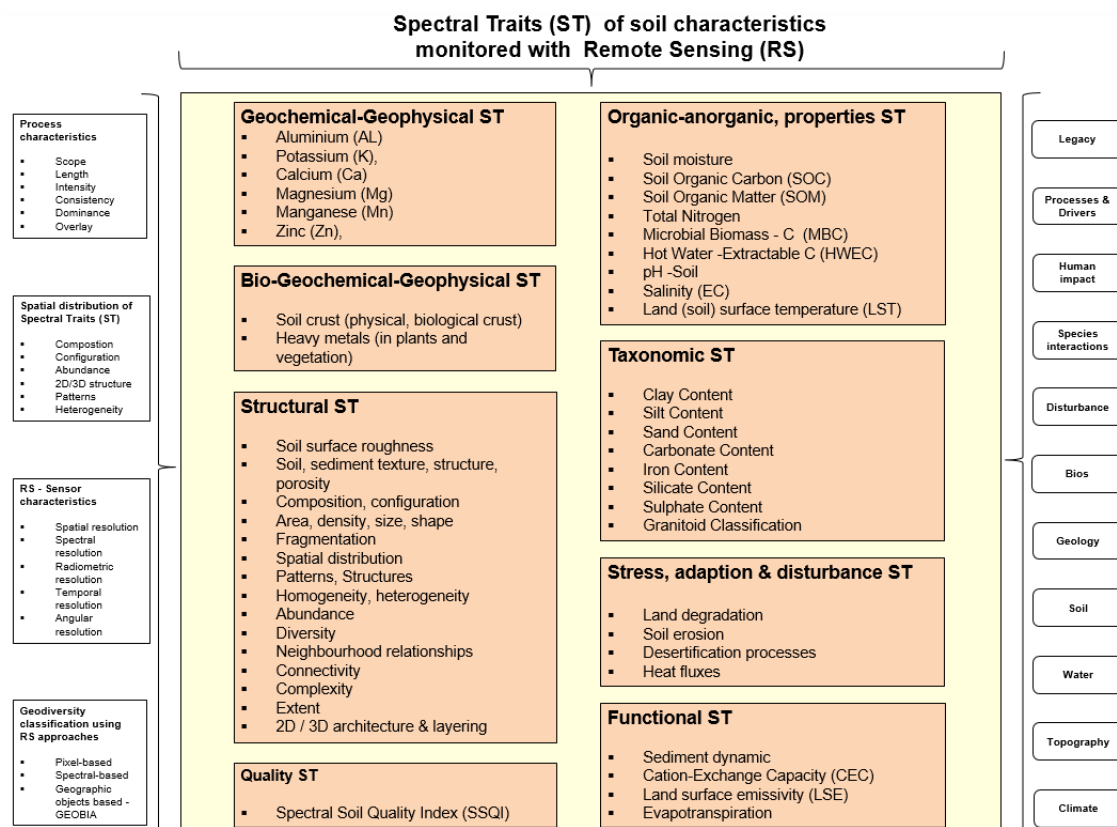


Figure 13. Spectral traits for monitoring soil characteristics and their traits with remote sensing and its constraints (modified after Lausch et al. [1,3]).

There are limitations to monitoring soil characteristics and soil moisture, because they are influenced by the growth of vegetation. In the paper we illustrate how indirect techniques can be used on vegetation as a sensor, proxy, and indicator to monitor the status, stress, or resource limitations of soil characteristics and soil moisture.

No single monitoring technique, RS sensor, RS-approach, sensor platform, scale, or model approach is sufficient on its own to monitor and model the complexity of biodiversity, the abiotic systems, and the interactions between abiotic and biotic processes and functions in order to assess the

resilience of biodiversity and ecosystem health. As a result, the RS sensors and techniques illustrated here need to be incorporated into a single network to establish a multi-source-ecosystem health monitoring network (MUSO-EH-MN) based on Data Science, the Semantic Web (Web 4.0), and Linked Open Data approaches [57,408–410].

Furthermore, the monitoring of geodiversity and their geotraits is the basis for a better understanding of ecosystem integrity [411].

Author Contributions: A.L. was responsible for the main part of this review, writing and production of some tables and figures. M.V., S.C., A.K., M.M. (Markus Möller), C.M. (Christian Mielke), H.G., C.T., C.R., O.R., C.M. (Carsten Montzka), A.J., D.H., M.M. (Mohsen Makki), C.S. (Christian Schweitzer), J.B. (Jussi Baade), C.S. (Christiane Schullius), and C.G. contributed their knowledge to the section on soil characteristics; T.J., C.M. (Carsten Montzka), and M.S. wrote the section on soil moisture; K.S. and R.K. developed the topic land surface temperature: L.B., J.M.H., S.J., D.S., A.L., M.P., and M.E.S. have operated airborne platforms for many years and were thus able to provide decisive examples and figures for the review paper. E.B., J.B. (Jan Bumberger), P.D., H.M., R.W., U.W. (Ulrike Werban), U.W. (Ute Wollschläger), U.W. (Ute Weber), C.S. (Claudia Schütze), P.S., and S.Z. gave important inputs for close-range and in-situ methods for the recording of soil characteristics. In proofreading and conceptual implementation, the following support is particularly important S.C.T. (Sina C. Truckenbrodt), F.S., A.K.S., and M.E.S. All co-authors provided extensive reviews of the paper and revised all requirements, checked, and contributed to the final text, tables, and figures.

Funding: This research received no external funding.

Acknowledgments: We particularly thank the researchers for the Hyperspectral Equipment of the Helmholtz Centre for Environmental Research—UFZ and TERENO funded by the Helmholtz Association and the Federal Ministry of Education and Research. This work was supported by funding from the Helmholtz Association in the framework of MOSES (Modular Observation Solutions for Earth Systems). At the same time we truly appreciate the support that we received from the project ‘GEOEssential — Essential Variables workflows for resource efficiency and environmental management’. The authors also thank the reviewers for their very valuable comments and recommendations. The authors gratefully acknowledge the German Helmholtz Association for support of the activities. This study (Soil Moisture retrieval—Figure 7c–e) was conducted under the funding of the HGF Alliance HA-310 ‘Remote Sensing and Earth System Dynamics’. UM is grateful to the Helmholtz funded virtual institute DESERVE. Airborne Research Australia is substantially supported by the Hackett Foundation, Adelaide. One of the ARA ECO-Dimonas was donated by the late Dr. Don and Joyce Schultz of Glen Osmond, South Australia.

Conflicts of Interest: The authors declare no conflict of interest.

References

1. Lausch, A.; Bannehr, L.; Beckmann, M.; Boehm, C.; Feilhauer, H.; Hacker, J.M.; Heurich, M.; Jung, A.; Klenke, R.; Neumann, C.; et al. Linking Earth Observation and taxonomic, structural and functional biodiversity: Local to ecosystem perspectives. *Ecol. Indic.* **2016**, *70*, 317–339. [[CrossRef](#)]
2. Lausch, A.; Olaf, B.; Stefan, K.; Leitao, P.; Jung, A.; Rocchini, D.; Schaepman, M.E.; Skidmore, A.K.; Tischendorf, L.; Knapp, S. Understanding and assessing vegetation health by in-situ species and remote sensing approaches. *Methods Ecol. Evol.* **2018**, *9*, 1799–1809. [[CrossRef](#)]
3. Lausch, A.; Erasmi, S.; King, D.; Magdon, P.; Heurich, M. Understanding Forest Health with Remote Sensing—Part I—A Review of Spectral Traits, Processes and Remote-Sensing Characteristics. *Remote Sens.* **2016**, *8*, 1029. [[CrossRef](#)]
4. Schrodt, F.; Bailey, J.J.; Kissling, W.D.; Rijdsdijk, K.F.; Seijmonsbergen, A.C.; van Ree, D.; Hjort, J.; Lawley, R.S.; Williams, C.N.; Anderson, M.G.; et al. Opinion: To advance sustainable stewardship, we must document not only biodiversity but geodiversity. *Proc. Natl. Acad. Sci.* **2019**, *116*, 16155–16158. [[CrossRef](#)] [[PubMed](#)]
5. Sala, O.E.; Chapin, F.S.; Armesto, J.J.; Berlow, E.; Bloomfield, J.; Dirzo, R.; Huber-Sanwald, E.; Huenneke, L.F.; Jackson, R.B.; Kinzig, A.; et al. Biodiversity: Global biodiversity scenarios for the year 2100. *Science* **2005**, *287*, 1770–1775. [[CrossRef](#)] [[PubMed](#)]
6. Bardgett, R.D.; Wardle, D.A. *Aboveground-Belowground Linkages: Biotic Interactions, Ecosystem Processes, and Global Change*; Oxford University Press: Oxford, UK, 2010; ISBN 0199546886.
7. De Deyn, G.B.; Van Der Putten, W.H. Linking aboveground and belowground diversity. *Trends Ecol. Evol.* **2005**, *20*, 625–633. [[CrossRef](#)] [[PubMed](#)]
8. Eisenhauer, N. Aboveground-belowground interactions drive the relationship between plant diversity and ecosystem function. *Res. Ideas Outcomes* **2018**, *4*, e23688. [[CrossRef](#)]

9. Wardle, D.A. Ecological Linkages Between Aboveground and Belowground Biota. *Science* **2004**, *304*, 1629–1633. [[CrossRef](#)]
10. Atkinson, N.J.; Urwin, P.E. The interaction of plant biotic and abiotic stresses: From in *Posidonia oceanica* cadmium induces changes in DNA genes to the field. *J. Exp. Bot.* **2012**, *63*, 3523–3544. [[CrossRef](#)]
11. Van der Ploeg, M.J.; Baartman, J.E.M.; Robinson, D.A. BIOPHYSICAL LANDSCAPE INTERACTIONS: BRIDGING DISCIPLINES AND SCALE WITH CONNECTIVITY. *Land Degrad. Dev.* **2017**, *29*, 1167–1175. [[CrossRef](#)]
12. Balzotti, C.S.; Asner, G.P. Biotic and Abiotic Controls Over Canopy Function and Structure in Humid Hawaiian Forests. *Ecosystems* **2018**, *21*, 331–348. [[CrossRef](#)]
13. De Vries, F.T.; Manning, P.; Tallowin, J.R.B.; Mortimer, S.R.; Pilgrim, E.S.; Harrison, K.A.; Hobbs, P.J.; Quirk, H.; Shipley, B.; Cornelissen, J.H.C.; et al. Abiotic drivers and plant traits explain landscape-scale patterns in soil microbial communities. *Ecol. Lett.* **2012**, *15*, 1230–1239. [[CrossRef](#)]
14. Porazinska, D.L.; Bardgett, R.D.; Blaauw, M.B.; Hunt, H.W.; Parsons, A.N.; Seastedt, T.R.; Wall, D.H. Relationships at the Aboveground-Belowground Interface: Plants, Soil Biota, and Soil Processes. *Ecol. Monogr.* **2018**, *73*, 377–395. [[CrossRef](#)]
15. Nielsen, U.N.; Ayres, E.; Wall, D.H.; Bardgett, R. Soil biodiversity and carbon cycling: A review and synthesis of studies examining diversity-function. *Eur. J. Soil Sci.* **2011**, *62*, 105–116. [[CrossRef](#)]
16. Freschet, G.T.; Violle, C.; Bourget, M.Y.; Scherer-Lorenzen, M.; Fort, F. Allocation, morphology, physiology, architecture: The multiple facets of plant above- and below-ground responses to resource stress. *New Phytol.* **2018**, *219*, 1338–1352. [[CrossRef](#)] [[PubMed](#)]
17. Freschet, G.T.; Swart, E.M.; Cornelissen, J.H.C. Integrated plant phenotypic responses to contrasting above- and below-ground resources: Key roles of specific leaf area and root mass fraction. *New Phytol.* **2015**, *206*, 1247–1260. [[CrossRef](#)] [[PubMed](#)]
18. Ríos-Casanova, L.; Valiente-Banuet, A.; Rico-Gray, V. Original article Ant diversity and its relationship with vegetation and soil factors in an alluvial fan of the Tehuacán Valley, Mexico. *Acta Oecol.* **2006**, *29*, 316–323. [[CrossRef](#)]
19. Orwin, K.H.; Buckland, S.M.; Johnson, D.; Turner, B.L.; Smart, S.; Oakley, S.; Bardgett, R.D. Linkages of plant traits to soil properties and the functioning of temperate grassland. *J. Ecol.* **2010**, *98*, 1074–1083. [[CrossRef](#)]
20. Mueller, K.E.; Hobbie, S.E.; Chorover, J.; Reich, P.B.; Hale, C.M.; Jagodzina, A.M. Effects of litter traits, soil biota, and soil chemistry on soil carbon stocks at a common garden with 14 tree species. *Biogeochemistry* **2015**, *123*, 313–327. [[CrossRef](#)]
21. Krishnan, P.; Kochendorfer, J.; Dumas, E.J.; Guillevic, P.C.; Baker, C.B.; Meyers, T.P.; Martos, B. Comparison of in-situ, aircraft, and satellite land surface temperature measurements over a NOAA Climate Reference Network site. *Remote Sens. Environ.* **2015**, *165*, 249–264. [[CrossRef](#)]
22. Biggs, J.; von Fumetti, S.; Kelly-Quinn, M. The importance of small waterbodies for biodiversity and ecosystem services: Implications for policy makers. *Hydrobiologia* **2017**, *793*, 3–39. [[CrossRef](#)]
23. Ordoñez, J.C.; Van Bodegom, P.M.; Witte, J.M.; Wright, I.J.; Reich, P.B.; Aerts, R. A global study of relationships between leaf traits, climate and soil measures of nutrient fertility. *Glob. Ecol. Biogeogr.* **2009**, *18*, 137–149. [[CrossRef](#)]
24. Williams, J.W.; Jackson, S.T. Novel climates, no-analog communities, and ecological surprises. *Front. Ecol. Environ.* **2007**, *5*, 475–482. [[CrossRef](#)]
25. Grime, J.P. Vegetation classification by reference to strategies. *Nature* **1974**, *250*, 26–31. [[CrossRef](#)]
26. Díaz, S.; Kattge, J.; Cornelissen, J.H.C.; Wright, I.J.; Lavorel, S.; Dray, S.; Reu, B.; Kleyer, M.; Wirth, C.; Prentice, I.C.; et al. The global spectrum of plant form and function. *Nature* **2015**, *529*, 1–17. [[CrossRef](#)] [[PubMed](#)]
27. Wright, I.J.; Reich, P.B.; Westoby, M.; Ackerly, D.D.; Baruch, Z.; Bongers, F.; Cavender-Bares, J.; Chapin, T.; Cornelissen, J.H.C.; Diemer, M.; et al. The worldwide leaf economics spectrum. *Nature* **2004**, *428*, 821–827. [[CrossRef](#)] [[PubMed](#)]
28. Beckmann, M.; Gerstner, K.; Akin-Fajiyiye, M.; Ceaşu, S.; Kambach, S.; Kinlock, N.L.; Phillips, H.R.P.; Verhagen, W.; Gurevitch, J.; Klotz, S.; et al. Conventional land-use intensification reduces species richness and increases production: A global meta-analysis. *Glob. Chang. Biol.* **2019**, *25*, 1941–1956. [[CrossRef](#)] [[PubMed](#)]

29. Knapp, S.; Dinsmore, L.; Fissore, C.; Hobbie, S.E.; Jakobsdottir, I.; Kattge, J.; King, J.Y.; Klotz, S.; McFadden, J.P.; Cavender-Bares, J. Phylogenetic and functional characteristics of household yard floras and their changes along an urbanization gradient. *Ecology* **2012**, *93*, 83–98. [[CrossRef](#)]
30. Lavorel, S.; McIntyre, S.; Landsberg, J.; Forbes, T.D.A. Plant functional classifications: From general groups to specific groups based on response to disturbance. *Trends Ecol. Evol.* **1997**, *12*, 474–478. [[CrossRef](#)]
31. Kattenborn, T.; Fassnacht, F.E.; Schmidlein, S. Differentiating plant functional types using reflectance: Which traits make the difference? *Remote Sens. Ecol. Conserv.* **2018**, *5*, 5–19. [[CrossRef](#)]
32. Walther, G.; Post, E.; Convey, P.; Menzel, A.; Parmesan, C.; Beebee, T.J.C.; Fromentin, J.-M.; Hoegh-Guldberg, O.; Bairlein, F. Ecological responses to recent climate change. *Nature* **2002**, *416*, 389–395. [[CrossRef](#)]
33. Franklin, J.; Serra-Diaz, J.M.; Syphard, A.D.; Regan, H.M. Global change and terrestrial plant community dynamics. *Proc. Natl. Acad. Sci. USA* **2016**, *113*, 3725–3734. [[CrossRef](#)] [[PubMed](#)]
34. Thakur, M.P.; Tilman, D.; Purschke, O.; Ciobanu, M.; Cowles, J.; Isbell, F.; Wragg, P.D.; Eisenhauer, N. Climate warming promotes species diversity, but with greater taxonomic redundancy, in complex environments. *Sci. Adv.* **2017**, *3*, 1–10. [[CrossRef](#)] [[PubMed](#)]
35. Marcott, S.A.; Shakun, J.D.; Clark, P.U.; Mix, A.C. A Reconstruction of Regional temperatures. *Science* **2013**, *339*, 1198–1201. [[CrossRef](#)] [[PubMed](#)]
36. Kraemer, B.M.; Mehner, T.; Adrian, R. Reconciling the opposing effects of warming on phytoplankton biomass in 188 large lakes. *Sci. Rep.* **2017**, *7*, 10762. [[CrossRef](#)] [[PubMed](#)]
37. Reilly, C.M.O.; Sharma, S.; Gray, D.K.; Hampton, S.E.; Read, J.S.; Rowley, R.J.; Schneider, P.; Lenters, J.D.; McIntyre, P.B.; Kraemer, B.M.; et al. Rapid and highly variable warming of lake surface waters around the globe. *Geophys. Res. Lett.* **2015**, *42*, 10773–10781. [[CrossRef](#)]
38. Veloz, S.D.; Williams, J.W.; Blois, J.L.; He, F.; Otto-Bliesner, B.; Liu, Z. No-analog climates and shifting realized niches during the late quaternary: Implications for 21st-century predictions by species distribution models. *Glob. Chang. Biol.* **2012**, *18*, 1698–1713. [[CrossRef](#)]
39. Fei, S.; Desprez, J.M.; Potter, K.M.; Jo, I.; Knott, J.A.; Oswalt, C.M. Divergence of species responses to climate change. *Sci. Adv.* **2017**. [[CrossRef](#)] [[PubMed](#)]
40. Lawler, J.J.; Ackerly, D.D.; Albano, C.M.; Anderson, M.G.; Dobrowski, S.Z.; Gill, J.L.; Heller, N.E.; Pressey, R.L.; Sanderson, E.W.; Weiss, S.B. The theory behind, and the challenges of, conserving nature's stage in a time of rapid change. *Conserv. Biol.* **2015**, *29*, 618–629. [[CrossRef](#)] [[PubMed](#)]
41. Smith, S.J.; Edmonds, J.; Hartin, C.A.; Mundra, A.; Calvin, K. Near-term acceleration in the rate of temperature change. *Nat. Clim. Chang.* **2015**, *5*, 333–336. [[CrossRef](#)]
42. Newbold, T.; Hudson, L.N.; Hill, S.L.L.; Contu, S.; Lysenko, I.; Senior, R.A.; Börger, L.; Bennett, D.J.; Choimes, A.; Collen, B.; et al. Global effects of land use on local terrestrial biodiversity. *Nature* **2015**, *520*, 45–50. [[CrossRef](#)]
43. Gossner, M.M.; Lewinsohn, T.M.; Kahl, T.; Grassein, F.; Boch, S.; Prati, D.; Birkhofer, K.; Renner, S.C.; Sikorski, J.; Wubet, T.; et al. Land-use intensification causes multitrophic homogenization of grassland communities. *Nature* **2016**, *540*, 266–269. [[CrossRef](#)] [[PubMed](#)]
44. Haase, D.; Güneralp, B.; Dahiya, B.; Bai, X.; Elmqvist, T. Global Urbanization: Perspectives and Trends. In *Urban Planet*; Elmqvist, T., Bai, X., Frantzeskaki, N., Griffith, C., Maddox, D., McPhearson, T., Parnell, S., Romero-Lankao, P., Simon, D., Watkins, M., Eds.; Cambridge University Press: London, UK, 2018; pp. 19–45. ISBN 9781316647554. [[CrossRef](#)]
45. Beier, P.; Brost, B. Uso de elementos territoriales para planificar para el cambio climático: Conservando las arenas, no los actores. *Conserv. Biol.* **2010**, *24*, 701–710. [[CrossRef](#)] [[PubMed](#)]
46. Pressey, R.L.; Cabeza, M.; Watts, M.E.; Cowling, R.M.; Wilson, K.A. Conservation planning in a changing world. *Trends Ecol. Evol.* **2007**, *22*, 583–592. [[CrossRef](#)] [[PubMed](#)]
47. Cameron, E.K.; Martins, I.S.; Lavelle, P.; Mathieu, J.; Tedersoo, L.; Bahram, M.; Gottschall, F.; Guerra, C.A.; Hines, J.; Patoine, G.; et al. Global mismatches in aboveground and belowground biodiversity. *Conserv. Biol.* **2019**, *33*, 1187–1192. [[CrossRef](#)]
48. Mulder, V.L.; de Bruin, S.; Schaepman, M.E.; Mayr, T.R. The use of remote sensing in soil and terrain mapping—A review. *Geoderma* **2011**, *162*, 1–19. [[CrossRef](#)]
49. Wulf, H.; Mulder, T.; Schaepman, M.E.; Keller, A.; Jörg, P.C. *Remote Sensing of Soils*; Remote Sensing Laboratories, University of Zurich: Zürich, Germany, 2015.

50. Babaeian, E.; Sadeghi, M.; Jones, S.B.; Montzka, C.; Vereecken, H. Ground, Proximal and Satellite Remote Sensing of Soil Moisture. *Rev. Geophys.* **2019**, *57*, 530–616. [[CrossRef](#)]
51. Mohanty, B.P.; Cosh, M.H.; Lakshmi, V.; Montzka, C. Soil Moisture Remote Sensing: State-of-the-Science. *Vadose Zone J.* **2017**, *16*, 1–9. [[CrossRef](#)]
52. Haase, D. Effects of urbanisation on the water balance—A long-term trajectory. *Environ. Impact Assess. Rev.* **2009**, *29*, 211–219. [[CrossRef](#)]
53. Dörnhöfer, K.; Oppelt, N. Remote sensing for lake research and monitoring—Recent advances. *Ecol. Indic.* **2016**, *64*, 105–122. [[CrossRef](#)]
54. Haase, D. Reflections about blue ecosystem services in cities. *Sustain. Water Qual. Ecol.* **2015**, *5*, 77–83. [[CrossRef](#)]
55. Woodcock, C.E.; Allen, R.; Anderson, M.; Belward, A.; Bindschadler, R.; Cohen, W.; Gao, F.; Goward, S.N.; Helder, D.; Helmer, E.; et al. Free Access to Landsat Imagery. *Science* **2008**, *320*, 1011–1012. [[CrossRef](#)]
56. Zhu, Z.; Wulder, M.A.; Roy, D.P.; Woodcock, C.E.; Hansen, M.C.; Radeloff, V.C.; Healey, S.P.; Schaaf, C.; Hostert, P.; Strobl, P.; et al. Benefits of the free and open Landsat data policy. *Remote Sens. Environ.* **2019**, *224*, 382–385. [[CrossRef](#)]
57. Lausch, A.; Borg, E.; Bumberger, J.; Dietrich, P.; Heurich, M.; Huth, A.; Jung, A.; Klenke, R.; Knapp, S.; Mollenhauer, H.; et al. Understanding Forest Health with Remote Sensing, Part III: Requirements for a Scalable Multi-Source Forest Health Monitoring Network Based on Data Science Approaches. *Remote Sens.* **2018**, *10*, 1120. [[CrossRef](#)]
58. Wulder, M.A.; White, J.C.; Loveland, T.R.; Woodcock, C.E.; Belward, A.S.; Cohen, W.B.; Fosnight, E.A.; Shaw, J.; Masek, J.G.; Roy, D.P. The global Landsat archive: Status, consolidation, and direction. *Remote Sens. Environ.* **2015**, *185*, 271–283. [[CrossRef](#)]
59. Turner, W.; Rondinini, C.; Pettorelli, N.; Mora, B.; Leidner, A.K.; Szantoi, Z.; Buchanan, G.; Dech, S.; Dwyer, J.; Herold, M.; et al. Free and open-access satellite data are key to biodiversity conservation. *Biol. Conserv.* **2015**, *182*, 173–176. [[CrossRef](#)]
60. Lausch, A.; Blaschke, T.; Haase, D.; Herzog, F.; Syrbe, R.-U.; Tischendorf, L.; Walz, U. Understanding and quantifying landscape structure—A review on relevant process characteristics, data models and landscape metrics. *Ecol. Model.* **2015**, *295*, 31–41. [[CrossRef](#)]
61. Gray, M. Other nature: Geodiversity and geosystem services. *Environ. Conserv.* **2011**, *38*, 271–274. [[CrossRef](#)]
62. Hjort, J.; Heikkinen, R.K.; Luoto, M. Inclusion of explicit measures of geodiversity improve biodiversity models in a boreal landscape. *Biodivers. Conserv.* **2012**, *21*, 3487–3506. [[CrossRef](#)]
63. National Research Council. *Basic Research Opportunities in Earth Science*; National Academies Press: Washington, DC, USA, 2001; ISBN 978-0-309-07133-8.
64. Record, S.; Dahlin, K.; Zarnetske, P.; Read, Q.; Malone, S.L.; Gaddis, K.; Grady, J.M.; Costanza, J.; Hobi, M.; Latimer, A.; et al. Remote sensing of geodiversity and biodiversity. In *The Nature of Biodiversity: Prospects for Remote Detection of Genetic, Phylogenetic, Functional and Ecosystem Components and Importance in Managing*; Cavender-Bares, J., Gamon, J., Townsend, P., Eds.; Springer: Berlin, Germany, 2019.
65. Sollins, P. Factors Influencing Species Composition in Tropical Lowland Rain Forest: Does Soil Matter? *Ecology* **1998**, *79*, 23–30. [[CrossRef](#)]
66. Mulder, V.L.; de Bruin, S.; Weyermann, J.; Kokaly, R.F.; Schaepman, M.E. Characterizing regional soil mineral composition using spectroscopy and geostatistics. *Remote Sens. Environ.* **2013**, *139*, 415–429. [[CrossRef](#)]
67. Clark, R.N.; Swayze, G.A.; Livo, K.E.; Kokaly, R.F.; Sutley, S.J.; Dalton, J.B.; McDougal, R.R.; Gent, C.A. Imaging spectroscopy: Earth and planetary remote sensing with the USGS Tetracorder and expert systems. *J. Geophys. Res.* **2003**, *108*. [[CrossRef](#)]
68. Gomez, C.; Adeline, K.; Bacha, S.; Driessen, B.; Gorretta, N.; Lagacherie, P.; Roger, J.M.; Briottet, X. Remote Sensing of Environment Sensitivity of clay content prediction to spectral configuration of VNIR/SWIR imaging data, from multispectral to hyperspectral scenarios. *Remote Sens. Environ.* **2018**, *204*, 18–30. [[CrossRef](#)]
69. Middleton, E.M.; Ungar, S.G.; Mandl, D.J.; Ong, L.; Frye, S.W.; Campbell, P.E.; Landis, D.R.; Young, J.P.; Pollack, N.H. The Earth Observing One (EO-1) Satellite Mission: Over a Decade in Space. *IEEE J. Sel. Top. Appl. Earth Obs. Remote Sens.* **2013**, *6*, 243–256. [[CrossRef](#)]

70. Mielke, C.; Boesche, N.K.; Rogass, C.; Segl, K.; Gauert, C.; Kaufmann, H. Potential applications of the Sentinel-2 multispectral sensor and the EnMap hyperspectral sensor in mineral exploration. *EARSel EProceedings* **2014**, *13*, 93–102.
71. Kokaly, R.F. Spectroscopic remote sensing for material identification, vegetation characterization, and mapping. In Proceedings of the SPIE 8390, Algorithms and Technologies for Multispectral, Hyperspectral and Ultraspectral Imagery XVIII, Baltimore, MD, USA, 23–27 April 2012; Volume 8390, p. 839014-12.
72. Irons, J.R.; Dwyer, J.L.; Barsi, J.A. The next Landsat satellite: The Landsat Data Continuity Mission. *Remote Sens. Environ.* **2012**, *122*, 11–21. [[CrossRef](#)]
73. Drusch, M.; Del Bello, U.; Carlier, S.; Colin, O.; Fernandez, V.; Gascon, F.; Hoersch, B.; Isola, C.; Laberinti, P.; Martimort, P.; et al. Sentinel-2: ESA's Optical High-Resolution Mission for GMES Operational Services. *Remote Sens. Environ.* **2012**, *120*, 25–36. [[CrossRef](#)]
74. Townsend, T.E. Discrimination of iron alteration minerals in visible and near-infrared reflectance data. *J. Geophys. Res. Solid Earth* **1987**, *92*, 1441–1454. [[CrossRef](#)]
75. Milewski, R.; Chabrillat, S.; Behling, R. Analyses of Recent Sediment Surface Dynamic of a Namibian Kalahari Salt Pan Based on Multitemporal Landsat and Hyperspectral Hyperion Data. *Remote Sens.* **2017**, *9*, 170. [[CrossRef](#)]
76. Van der Meer, F.D.; van der Werff, H.M.A.; van Ruitenbeek, F.J.A. Potential of ESA's Sentinel-2 for geological applications. *Remote Sens. Environ.* **2014**, *148*, 124–133. [[CrossRef](#)]
77. Abrams, M. The Advanced Spaceborne Thermal Emission and Reflection Radiometer (ASTER): Data products for the high spatial resolution imager on NASA's Terra platform. *Int. J. Remote Sens.* **2000**, *21*, 847–859. [[CrossRef](#)]
78. Van Der Meer, F.D.; Van Der Werff, H.M.A.; Van Ruitenbeek, F.J.A.; Hecker, C.A.; Bakker, W.H.; Noomen, M.F.; Van Der Meijde, M.; Carranza, E.J.M.; De Smeth, J.B.; Woldai, T. Multi and hyperspectral geologic remote sensing: A review. *Int. J. Appl. Earth Obs. Geoinf.* **2012**, *14*, 112–128. [[CrossRef](#)]
79. Rowan, L.C.; Mars, J.C. Lithologic mapping in the Mountain Pass, California area using Advanced Spaceborne Thermal Emission and Reflection Radiometer (ASTER) data. *Remote Sens. Environ.* **2003**, *84*, 350–366. [[CrossRef](#)]
80. Katra, I.; Lancaster, N. Surface-sediment dynamics in a dust source from spaceborne multispectral thermal infrared data. *Remote Sens. Environ.* **2008**, *112*, 3212–3221. [[CrossRef](#)]
81. Hunt, G.R. Spectral Signatures of Particulate Minerals in the visible and near infrared. *Geophysics* **1977**, *42*, 501–513. [[CrossRef](#)]
82. Zaini, N.; van der Meer, F.; van der Werff, H. Effect of grain size and mineral mixing on carbonate absorption features in the SWIR and TIR wavelength regions. *Remote Sens.* **2012**, *4*, 987–1003. [[CrossRef](#)]
83. Lane, M.D.; Christensen, P.R. Thermal infrared emission spectroscopy of anhydrous carbonates. *J. Geophys. Res.* **1997**, *102*, 25581–25592. [[CrossRef](#)]
84. Eisele, A.; Lau, I.; Hewson, R.; Carter, D.; Wheaton, B.; Ong, C.; Cudahy, T.J.; Chabrillat, S.; Kaufmann, H. Applicability of the Thermal Infrared Spectral Region for the Prediction of Soil Properties across Semi-Arid Agricultural Landscapes. *Remote Sens.* **2012**, *4*, 3265–3286. [[CrossRef](#)]
85. Eisele, A.; Chabrillat, S.; Hecker, C.; Hewson, R.; Lau, I.C.; Rogass, C.; Segl, K.; John, T.; Udelhoven, T.; Hostert, P.; et al. Remote Sensing of Environment Advantages using the thermal infrared (TIR) to detect and quantify semi-arid soil properties. *Remote Sens. Environ.* **2015**, *163*, 296–311. [[CrossRef](#)]
86. Kirkland, L.; Herr, K.; Keim, E.; Adams, P.; Salisbury, J.; Hackwell, J.; Treiman, A. First use of an airborne thermal infrared hyperspectral scanner for compositional mapping. *Remote Sens. Environ.* **2002**, *80*, 447–459. [[CrossRef](#)]
87. Vaughan, R.G.; Hook, S.J.; Calvin, W.M.; Taranik, J.V. Surface mineral mapping at Steamboat Springs, Nevada, USA, with multi-wavelength thermal infrared images. *Remote Sens. Environ.* **2005**, *99*, 140–158. [[CrossRef](#)]
88. Adar, S.; Shkolnisky, Y.; Notesco, G.; Ben-Dor, E. Using visible spectral information to predict long-wave infrared spectral emissivity: A case study over the sokolov area of the czech republic with an airborne hyperspectral scanner sensor. *Remote Sens.* **2013**, *5*, 5757–5782. [[CrossRef](#)]
89. Notesco, G.; Ogen, Y.; Ben-Dor, E. Mineral classification of makhtesh ramon in israel using hyperspectral longwave infrared (LWIR) remote-sensing data. *Remote Sens.* **2015**, *7*, 12282–12296. [[CrossRef](#)]

90. Notesco, G.; Ogen, Y.; Ben-Dor, E. Integration of hyperspectral shortwave and longwave infrared remote-sensing data for mineral mapping of Makhtesh Ramon in Israel. *Remote Sens.* **2016**, *8*, 318. [[CrossRef](#)]
91. Weksler, S.; Rozenstein, O.; Ben-dor, E. Mapping Surface Quartz Content in Sand Dunes Covered by Biological Soil Crusts Using Airborne Hyperspectral Images in the Longwave. *Minerals* **2018**, *8*, 318. [[CrossRef](#)]
92. Black, M.; Riley, T.R.; Ferrier, G.; Fleming, A.H.; Fretwell, P.T. Automated lithological mapping using airborne hyperspectral thermal infrared data: A case study from Anchorage Island, Antarctica. *Remote Sens. Environ.* **2016**, *176*, 225–241. [[CrossRef](#)]
93. Conforti, P.; Gagnon, M.; Tremblay, P.; Chamberland, M. Long-wave infrared surface reflectance spectra retrieved from Telops Hyper-Cam imagery. In Proceedings of the SPIE 9088, Algorithms and Technologies for Multispectral, Hyperspectral, and Ultraspectral Imagery XX, 90880U, Baltimore, MD, USA, 13 June 2014; Volume 9088. [[CrossRef](#)]
94. Van Der Meer, F. Classification of remotely-sensed imagery using an indicator kriging approach: Application to the problem of calcite-dolomite mineral mapping. *Int. J. Remote Sens.* **1996**, *17*, 1233–1249. [[CrossRef](#)]
95. Vaughan, R.G.; Calvin, W.M.; Taranik, J.V. SEBASS hyperspectral thermal infrared data: Surface emissivity measurement and mineral mapping. *Remote Sens. Environ.* **2003**, *85*, 48–63. [[CrossRef](#)]
96. Sabins, F.F. Remote sensing for mineral exploration. *Ore Geol. Rev.* **1999**, *14*, 157–183. [[CrossRef](#)]
97. Rajesh, H.M. Application of remote sensing and GIS in mineral resource mapping an overview. *J. Mineral. Pedrol. Sci.* **2004**, *99*, 83–103. [[CrossRef](#)]
98. Mielke, C.; Boesche, N.K.; Rogass, C.; Kaufmann, H.; Gauert, C.; de Wit, M. Spaceborne Mine Waste Mineralogy Monitoring in South Africa, Applications for Modern Push-Broom Missions: Hyperion/OLI and EnMAP/Sentinel-2. *Remote Sens.* **2014**, *6*, 6790–6816. [[CrossRef](#)]
99. Gholizadeh, H.; Gamon, J.A.; Zyguelbaum, A.I.; Wang, R.; Schweiger, A.K.; Cavender-Bares, J. Remote sensing of biodiversity: Soil correction and datadimension reduction methods improve assessment of α -diversity (species richness) in prairie ecosystems. *Remote Sens. Environ.* **2018**, *206*, 240–253. [[CrossRef](#)]
100. Lausch, A.; Zacharias, S.; Dierke, C.; Pause, M.; Kühn, I.; Doktor, D.; Dietrich, P.; Werban, U. Analysis of vegetation and soil pattern using hyperspectral remote sensing, EMI and Gamma ray measurements. *Vadose Zone J.* **2013**, *12*. [[CrossRef](#)]
101. Vereecken, H.; Schnepf, A.; Hopmans, J.W.; Javaux, M.; Or, D.; Roose, T.; Vanderborght, J.; Young, M.H.; Amelung, W.; Aitkenhead, M.; et al. Modeling Soil Processes: Review, Key Challenges, and New Perspectives. *Vadose Zone J.* **2016**, *15*. [[CrossRef](#)]
102. Minasny, B.; McBratney, A.B. Digital soil mapping: A brief history and some lessons. *Geoderma* **2016**, *264*, 301–311. [[CrossRef](#)]
103. Grunwald, S.; Vasques, G.M.; Rivero, R.G. *Fusion of Soil and Remote Sensing Data to Model Soil Properties*, 1st ed.; Sparks, D.L., Ed.; Elsevier: Amsterdam, The Netherlands, 2015.
104. Escribano, P.; Schmid, T.; Chabrilat, S.; Rodríguez-Caballero, E.; García, M. Optical Remote Sensing for Soil Mapping and Monitoring. In *Soil Mapping and Process Modeling for Sustainable Land Use Management*; Elsevier: Amsterdam, The Netherlands, 2017; pp. 87–125.
105. Maynard, J.J.; Levi, M.R. Hyper-temporal remote sensing for digital soil mapping: Characterizing soil-vegetation response to climatic variability. *Geoderma* **2017**, *285*, 94–109. [[CrossRef](#)]
106. Anderson, K.; Croft, H. Remote sensing of soil surface properties. *Prog. Phys. Geogr.* **2009**, *33*, 457–473. [[CrossRef](#)]
107. Babaeian, E.; Homae, M.; Montzka, C.; Vereecken, H.; Norouzi, A.A. Towards Retrieving Soil Hydraulic Properties by Hyperspectral Remote Sensing. *Vadose Zone J.* **2015**, *14*. [[CrossRef](#)]
108. Riedel, F.; Denk, M.; Müller, I.; Barth, N.; Gläßer, C. Prediction of soil parameters using the spectral range between 350 and 15,000 nm: A case study based on the Permanent Soil Monitoring Program in Saxony, Germany. *Geoderma* **2018**, *315*, 188–198. [[CrossRef](#)]
109. Chabrilat, S.; Schmid, T.; Milewski, R.; Escribano, P.; Garcia, M.; Ben-Dor, E.; Guillaso, S.; Pelayo, M.; Reyes, A.; Sobejano-Paz, V.; et al. Mapping crop variability related to soil quality and crop stress within rainfed Mediterranean agroecosystems using hyperspectral data. In Proceedings of the 10th Workshop on Hyperspectral Image and Signal Processing: Evolution in Remote Sensing (WHISPERS), Amsterdam, The Netherlands, 26–28 September 2018.

110. Galvão, L.S.; Pizarro, M.A.; Epiphanyo, J.C.N. Variations in reflectance of tropical soils: Spectral-chemical composition relationships from AVIRIS data. *Remote Sens. Environ.* **2001**, *75*, 245–255. [[CrossRef](#)]
111. Ben-Dor, E.; Bania, A. Near-Infrared Analysis as a Rapid Method to Simultaneously Evaluate Several Soil Properties. *Soil Sci. Soc. Am. J.* **1995**, *59*, 364–372. [[CrossRef](#)]
112. Nocita, M.; Stevens, A.; van Wesemael, B.; Aitkenhead, M.; Bachmann, M.; Barthes, B.; Dor, E.B.; Brown, D.J.; Clairotte, M.; Csorba, A.; et al. Chapter Four—Soil Spectroscopy: An Alternative to Wet Chemistry for Soil Monitoring. *Adv. Agron.* **2015**, *132*, 139–159.
113. Castaldi, F.; Chabrillat, S.; Jones, A.; Vreys, K.; Bomans, B.; Van Wesemael, B. Soil Organic Carbon Estimation in Croplands by Hyperspectral Remote APEX Data Using the LUCAS Topsoil Database. *Remote Sens.* **2018**, *10*, 153. [[CrossRef](#)]
114. Vasques, G.M.; Grunwald, S.; Sickman, J.O. Comparison of multivariate methods for inferential modeling of soil carbon using visible/near-infrared spectra. *Geoderma* **2008**, *146*, 14–25. [[CrossRef](#)]
115. Gomez, C.; Lagacherie, P.; Coulouma, G. Continuum removal versus PLSR method for clay and calcium carbonate content estimation from laboratory and airborne hyperspectral measurements. *Geoderma* **2008**, *148*, 141–148. [[CrossRef](#)]
116. Chabrillat, S.; Eisele, A.; Guillaso, S.; Rogaß, C.; Ben-Dor, E.; Kaufmann, H. HYSOMA: An easy-to-use software interface for soil mapping applications of hyperspectral imagery. In Proceedings of the 7th EARSeL SIG Imaging Spectroscopy workshop, Edinburgh, UK, April 2011.
117. Gomez, C.; Lagacherie, P.; Coulouma, G. Regional predictions of eight common soil properties and their spatial structures from hyperspectral Vis-NIR data. *Geoderma* **2012**, *189–190*, 176–185. [[CrossRef](#)]
118. Stevens, A.; Udelhoven, T.; Denis, A.; Tychon, B.; Liroy, R.; Hoffmann, L.; van Wesemael, B.; Van Wesemael, B. Measuring soil organic carbon in croplands at regional scale using airborne imaging spectroscopy. *Geoderma* **2010**, *158*, 32–45. [[CrossRef](#)]
119. Lausch, A.; Pause, M.; Merbach, I.; Zacharias, S.; Doktor, D.; Volk, M.; Seppelt, R. A new multiscale approach for monitoring vegetation using remote sensing-based indicators in laboratory, field, and landscape. *Environ. Monit. Assess.* **2013**, *185*, 1215–1235. [[CrossRef](#)] [[PubMed](#)]
120. Toure, S. Detection of Carbon Stock Change in Agricultural Soils Using Spectroscopic Techniques. *Soil Sci. Soc.* **2006**, *70*, 844–850.
121. Chabrillat, S.; Ben-Dor, E.; Cierniewski, J.; Gomez, C.; Schmid, T.; van Wesemael, B. Imaging Spectroscopy for Soil Mapping and Monitoring. *Surv. Geophys.* **2019**, *40*, 361–399. [[CrossRef](#)]
122. Ouerghemmi, W.; Gomez, C.; Naceur, S.; Lagacherie, P. Geoderma Applying blind source separation on hyperspectral data for clay content estimation over partially vegetated surfaces. *Geoderma* **2011**, *163*, 227–237. [[CrossRef](#)]
123. Gerighausen, H.; Menz, G.; Kaufmann, H. Spatially explicit estimation of clay and organic carbon content in agricultural soils using multi-annual imaging spectroscopy data. *Appl. Environ. Soil Sci.* **2012**, *2012*, 868090. [[CrossRef](#)]
124. D’Elia, G.; Holsten, F. Kognitiv terapi har visat god effekt pa panikangest. *Lakartidningen* **1998**, *95*, 4869–4872. [[PubMed](#)]
125. Ouerghemmi, W.; Gomez, C.; Naceur, S.; Lagacherie, P. Remote Sensing of Environment Semi-blind source separation for the estimation of the clay content over semi-vegetated areas using VNIR/SWIR hyperspectral airborne data. *Remote Sens. Environ.* **2016**, *181*, 251–263. [[CrossRef](#)]
126. Diek, S.; Chabrillat, S.; Nocita, M.; Schaepman, M.E.; De Jong, R. Minimizing soil moisture variations in multi-temporal airborne imaging spectrometer data for digital soil mapping. *Geoderma* **2019**, *337*, 607–621. [[CrossRef](#)]
127. Bayer, A.D.; Bachmann, M.; Rogge, D.; Müller, A.; Kaufmann, H. Combining Field and Imaging Spectroscopy to Map Soil Organic Carbon in a Semiarid Environment. *IEEE J. Sel. Top. Appl. Earth Obs. Remote Sens.* **2016**, *9*, 3997–4010. [[CrossRef](#)]
128. Yu, H.; Kong, B.; Wang, G.; Du, R.; Qie, G. Prediction of soil properties using a hyperspectral remote sensing method. *Arch. Agron. Soil Sci.* **2017**, *64*, 546–559. [[CrossRef](#)]
129. Götze, C.; Beyer, F.; Gläßer, C. Pioneer vegetation as an indicator of the geochemical parameters in abandoned mine sites using hyperspectral airborne data. *Environ. Earth Sci.* **2016**, *75*, 613. [[CrossRef](#)]

130. Ben-Dor, E.; Patkin, K.; Banin, A.; Karnieli, A. Mapping of several soil properties using DAIS-7915 hyperspectral scanner data—A case study over clayey soils in Israel. *Int. J. Remote Sens.* **2002**, *23*, 1043–1062. [[CrossRef](#)]
131. Selige, T.; Böhmer, J.; Schmidhalter, U. High resolution topsoil mapping using hyperspectral image and field data in multivariate regression modeling porcedures. *Geoderma* **2006**, *136*, 235–244. [[CrossRef](#)]
132. Vohland, M.; Ludwig, M.; Thiele-Bruhn, S.; Ludwig, B. Quantification of soil properties with hyperspectral data: Selecting spectral variables with different methods to improve accuracies and analyze prediction mechanisms. *Remote Sens.* **2017**, *9*, 1103. [[CrossRef](#)]
133. Estimations, T. Regionalization of Uncovered Agricultural Soils Based on Organic Carbon and Soil Texture Estimations. *Remote Sens.* **2016**, *8*, 927.
134. Stumpf, F.; Keller, A.; Schmidt, K.; Mayr, A.; Gubler, A.; Schaepman, M. Spatio-temporal land use dynamics and soil organic carbon in Swiss agroecosystems. *Agric. Ecosyst. Environ.* **2018**, *258*, 129–142. [[CrossRef](#)]
135. Paz-Kagan, T.; Zaady, E.; Salbach, C.; Schmidt, A.; Lausch, A.; Zacharias, S.; Notesco, G.; Ben Dor, E.; Karnieli, A. Developing a Spectral Soil Quality Index (SSQI) Map using Imaging Spectroscopy. *Remote Sens.* **2015**, *7*, 15748–15781. [[CrossRef](#)]
136. Jung, A.; Vohland, M.; Thiele-Bruhn, S. Use of A Portable Camera for Proximal Soil Sensing with Hyperspectral Image Data. *Remote Sens.* **2015**, *7*, 11434–11448. [[CrossRef](#)]
137. Ben-dor, E.; Levin, N.; Singer, A.; Karnieli, A.; Braun, O.; Kidron, G.J. Quantitative mapping of the soil rubification process on sand dunes using an airborne hyperspectral sensor. *Geoderma* **2006**, *131*, 1–21. [[CrossRef](#)]
138. Schmid, T.; Rodriguez-Rastrero, M.; Escibano, P.; Palacios-Orueta, A.; Ben-Dor, E.; Plaza, A.; Milewski, R.; Huesca, M.; Bracken, A.; Cicuendez, V.; et al. Characterization of Soil Erosion Indicators Using Hyperspectral Data from a Mediterranean Rainfed Cultivated Region. *IEEE J. Sel. Top. Appl. Earth Obs. Remote Sens.* **2016**, *9*, 845–860. [[CrossRef](#)]
139. Ben-Dor, E.; Goldshleger, N.; Benyamini, Y.; Agassi, M.; Blumberg, D.G. The Spectral Reflectance Properties of Soil Structural Crusts in the 1.2- to 2.5- μm Spectral Region. *Soil Sci. Soc. Am. J.* **2003**, *67*, 289–299. [[CrossRef](#)]
140. Escibano, P.; Palacios-orueta, A.; Oyonarte, C.; Chabrilat, S. Spectral properties and sources of variability of ecosystem components in a Mediterranean semiarid environment. *J. Arid Environ.* **2010**, *74*, 1041–1051. [[CrossRef](#)]
141. McBratney, A.B.; Mendonça Santos, M.L.; Minasny, B. On digital Soil Mapping. *Geoderma* **2003**, *117*, 3–52. [[CrossRef](#)]
142. Roy, D.P.; Ju, J.; Kline, K.; Scaramuzza, P.L.; Kovalsky, V.; Hansen, M.; Loveland, T.R.; Vermote, E.; Zhang, C. Web-enabled Landsat Data (WELD): Landsat ETM+ composited mosaics of the conterminous United States. *Remote Sens. Environ.* **2010**, *114*, 35–49. [[CrossRef](#)]
143. Möller, M.; Gerstmann, H.; Gao, F.; Dahms, T.C.; Förster, M. Coupling of phenological information and simulated vegetation index time series: Limitations and potentials for the assessment and monitoring of soil erosion risk. *CATENA* **2017**, *150*, 192–205. [[CrossRef](#)]
144. Blasch, G.; Spengler, D.; Hohmann, C.; Neumann, C.; Itzerott, S.; Kaufmann, H. Multitemporal soil pattern analysis with multispectral remote sensing data at the field-scale. *Comput. Electron. Agric.* **2015**, *113*, 1–13. [[CrossRef](#)]
145. Rogge, D.; Bauer, A.; Zeidler, J.; Mueller, A.; Esch, T.; Heiden, U. Building an exposed soil composite processor (SCMaP) for mapping spatial and temporal characteristics of soils with Landsat imagery (1984–2014). *Remote Sens. Environ.* **2018**, *205*, 1–17. [[CrossRef](#)]
146. Diek, S.; Fornallaz, F.; Schaepman, M.E.; De Jong, R. Barest Pixel Composite for Agricultural Areas Using Landsat Time Series. *Remote Sens.* **2017**, *9*, 1245. [[CrossRef](#)]
147. Blasch, G.; Spengler, D.; Itzerott, S.; Wessolek, G. Organic matter modeling at the landscape scale based on multitemporal soil pattern analysis using rapideye data. *Remote Sens.* **2015**, *7*, 11125–11150. [[CrossRef](#)]
148. Demattê, J.A.M.; Alves, M.R.; da Silva Terra, F.; Bosquilia, R.W.D.; Fongaro, C.T.; da Silva Barros, P.P. Is It Possible to Classify Topsoil Texture Using a Sensor Located 800 km Away from the Surface? *Rev. Bras. Ciência Solo* **2016**, *40*. [[CrossRef](#)]
149. Möller, M.; Koschitzki, T.; Hartmann, K.J.; Jahn, R. Plausibility test of conceptual soil maps using relief parameters. *Catena* **2012**, *88*, 57–67. [[CrossRef](#)]

150. Möller, M.; Volk, M. Effective map scales for soil transport processes and related process domains—Statistical and spatial characterization of their scale-specific inaccuracies. *Geoderma* **2015**, *247–248*, 151–160. [[CrossRef](#)]
151. Gomez, C.; Drost, A.P.A.; Roger, J. Analysis of the uncertainties affecting predictions of clay contents from VNIR/SWIR hyperspectral data. *Remote Sens. Environ.* **2015**, *156*, 58–70. [[CrossRef](#)]
152. Sullivan, D.G.; Shaw, J.N.; Rickman, D. IKONOS imagery to estimate surface soil property variability in two Alabama physiographies. *Soil Sci. Soc. Am. J.* **2005**, *69*, 1789–1798. [[CrossRef](#)]
153. Detar, W.R.; Chesson, J.H.; Penner, J.V.; Ojala, J.C. Detection of soil properties with airborne hyperspectral measurements of bare fields. *Trans. ASABE* **2008**, *51*, 463–470. [[CrossRef](#)]
154. Chabrillat, S.; Goetz, A.F.H.; Krosley, L.; Olsen, H.W. Use of hyperspectral images in the identification and mapping of expansive clay soils and the role of spatial resolution. *Remote Sens. Environ.* **2002**, *82*, 431–445. [[CrossRef](#)]
155. Steinberg, A.; Chabrillat, S.; Stevens, A.; Segl, K.; Foerster, S. Prediction of Common Surface Soil Properties Based on Vis-NIR Airborne and Simulated EnMAP Imaging Spectroscopy Data: Prediction Accuracy and Influence of Spatial Resolution. *Remote Sens.* **2016**, *8*, 7. [[CrossRef](#)]
156. Gomez, C.; Viscarra Rossel, R.A.; McBratney, A.B. Soil organic carbon prediction by hyperspectral remote sensing and field vis-NIR spectroscopy: An Australian case study. *Geoderma* **2008**, *146*, 403–411. [[CrossRef](#)]
157. Ducasse, E.; Hohmann, A.; Adeline, K.; Bourguignon, A.; Déliot, P.; Briottet, X.; Rig, D.R.P.; Guillemin, C.; Cedex, O. Unmixing of mineralogical clay intimate mixtures with laboratory hyperspectral images. In Proceedings of the IGARSS 2018—2018 IEEE International Geoscience and Remote Sensing Symposium, Valencia, Spain, 22–27 July 2018; IEEE: Piscataway, NJ, USA, 2018; pp. 7491–7494.
158. Hively, W.D.; Mccarty, G.W.; Reeves, J.B., III; Lang, M.W.; Oesterling, R.A.; Delwiche, S.R. Use of Airborne Hyperspectral Imagery to Map Soil Properties in Tilled Agricultural Fields. *Appl. Environ. Soil Sci.* **2011**, *2011*, 358193. [[CrossRef](#)]
159. Castaldi, F.; Palombo, A.; Santini, F.; Pascucci, S.; Pignatti, S.; Casa, R. Evaluation of the potential of the current and forthcoming multispectral and hyperspectral imagers to estimate soil texture and organic carbon. *Remote Sens. Environ.* **2016**, *179*, 54–65. [[CrossRef](#)]
160. Lagacherie, P.; Baret, F.; Feret, J.B.; Madeira Netto, J.; Robbez-Masson, J.M. Estimation of soil clay and calcium carbonate using laboratory, field and airborne hyperspectral measurements. *Remote Sens. Environ.* **2008**, *112*, 825–835. [[CrossRef](#)]
161. Bartholomeus, H.; Epema, G.; Schaepman, M. Determining iron content in Mediterranean soils in partly vegetated areas, using spectral reflectance and imaging spectroscopy. *Int. J. Appl. Earth Obs. Geoinf.* **2007**, *9*, 194–203. [[CrossRef](#)]
162. Choe, E.; Van Der Meer, F.; Van Ruitenbeek, F.; Van Der Werff, H.; de Smeth, B.; Kim, K.-W. Mapping of heavy metal pollution in stream sediments using combined geochemistry, field spectroscopy, and hyperspectral remote sensing: A case study of the Rodalquilar mining area, SE Spain. *Remote Sens. Environ.* **2008**, *112*, 3222–3233. [[CrossRef](#)]
163. Nawar, S.; Buddenbaum, H.; Hill, J. Digital Mapping of Soil Properties Using Multivariate Statistical Analysis and ASTER Data in an Arid Region. *Remote Sens.* **2015**, *7*, 1181–1205. [[CrossRef](#)]
164. Castaldi, F.; Hueni, A.; Chabrillat, S.; Ward, K.; Buttafuoco, G.; Bomans, B.; Vreys, K.; Brell, M.; Van Wesemael, B. Evaluating the capability of the Sentinel 2 data for soil organic carbon prediction in croplands. *ISPRS J. Photogramm. Remote Sens.* **2019**, *147*, 267–282. [[CrossRef](#)]
165. Schwanghart, W.; Jarmer, T. Linking spatial patterns of soil organic carbon to topography—A case study from south-eastern Spain. *Geomorphology* **2011**, *126*, 252–263. [[CrossRef](#)]
166. Zewdu, S.; Suryabhagavan, K.V.; Balakrishnan, M. Geo-spatial approach for soil salinity mapping in Sege Irrigation Farm, South Ethiopia. *J. Saudi Soc. Agric. Sci.* **2017**, *16*, 16–24. [[CrossRef](#)]
167. Wu, W.; Zucca, C.; Muhameed, A.S.; Al-Shafie, W.M.; Fadhil, A.M.; Al-Quraishi, A.M.F.; Nangia, V.; Zhu, M.; Liu, G. Soil salinity prediction and mapping by machine learning regression in Central Mesopotamia, Iraq. *Land Degrad. Dev.* **2018**, *29*, 4005–4014. [[CrossRef](#)]
168. Meng, L.; Zhou, S.; Zhang, H.; Bi, X. Estimating soil salinity in different landscapes of the Yellow River Delta through Landsat OLI/TIRS and ETM + Data. *J. Coast. Conserv.* **2016**, *20*, 271–279. [[CrossRef](#)]
169. Bannari, A.; El-battay, A.; Bannari, R.; Rhinane, H. Sentinel-MSI VNIR and SWIR Bands Sensitivity Analysis for Soil Salinity Discrimination in an Arid Landscape. *Remote Sens.* **2018**, *10*, 855. [[CrossRef](#)]

170. Kobayashi, C.; Lau, I.C.; Wheaton, B.; Bourke, L.; Kakuta, S. Mapping of soil salinity using an airborne hyperspectral sensor in Western Australia. In Proceedings of the 2015 IEEE International Geoscience and Remote Sensing Symposium (IGARSS), Milan, Italy, 26–31 July 2015; Volume 5, pp. 2684–2687.
171. Metternicht, G.I.; Zinck, J.A. Remote sensing of soil salinity: Potentials and constraints. *Remote Sens. Environ.* **2003**, *85*, 1–20. [[CrossRef](#)]
172. Chen, J.; Yuan, M.; Wang, L.; Shimazaki, H.; Tamura, M. A new index for mapping lichen-dominated biological soil crusts in desert areas. *Remote Sens. Environ.* **2005**, *96*, 165–175. [[CrossRef](#)]
173. Ben-dor, E.; Chabrilat, S.; Dematté, J.A.M.; Taylor, G.R.; Hill, J.; Whiting, M.L.; Sommer, S. Using Imaging Spectroscopy to study soil properties. *Remote Sens. Environ.* **2009**, *113*, S38–S55. [[CrossRef](#)]
174. Rozenstein, O.; Karnieli, A. Identification and characterization of Biological Soil Crusts in a sand dune desert environment across Israel-Egypt border using LWIR emittance spectroscopy. *J. Arid Environ.* **2015**, *112*, 75–86. [[CrossRef](#)]
175. Alavipanah, S.K.; Sensing, R. Remote sensing application in evaluation of soil characteristics in desert areas. *Nat. Environ. Chang.* **2016**, *2*, 1–24.
176. Maleki, M.; Amini, J.; Notarnicola, C. Soil Roughness Retrieval from TerraSar-X Data Using Neural Network and Fractal Method. *Adv. Space Res.* **2019**, *64*, 1117–1129. [[CrossRef](#)]
177. Baghdadi, N.; El Hajj, M.; Choker, M.; Zribi, M.; Bazzi, H.; Vaudour, E.; Gilliot, J.M.; Bousbih, S.; Mwampongo, D.E.; Tetis, U.M.R.; et al. Potential of sentinel-1 for estimating the soil roughness over agricultural soils. In Proceedings of the IGARSS 2018—2018 IEEE International Geoscience and Remote Sensing Symposium, Valencia, Spain, 22–27 July 2018; pp. 7516–7519.
178. Pause, M.; Lausch, A.; Bernhardt, M.; Hacker, J.; Schulz, K. Improving Soil Moisture Retrieval from Airborne L-band Radiometer Data by Considering Spatially Varying Roughness. *Can. J. Remote Sens.* **2014**, *40*, 15–25. [[CrossRef](#)]
179. Turner, R.; Panciera, R.; Tanase, M.A.; Lowell, K.; Hacker, J.M.; Walker, J.P. Estimation of soil surface roughness of agricultural soils using airborne LiDAR. *Remote Sens. Environ.* **2014**, *140*, 107–117. [[CrossRef](#)]
180. Eltner, A.; Maas, H.; Faust, D. Geoderma Soil micro-topography change detection at hillslopes in fragile Mediterranean landscapes. *Geoderma* **2018**, *313*, 217–232. [[CrossRef](#)]
181. Müller, B.; Bernhardt, M.; Jackisch, C.; Schulz, K. Estimating spatially distributed soil texture using time series of thermal remote sensing—A case study in central Europe. *Hydrol. Earth Syst. Sci.* **2016**, *20*, 3765–3775. [[CrossRef](#)]
182. Gomez, C.; Ultra-carrió, R.; Bacha, S.; Lagacherie, P.; Briottet, X. Evaluating the sensitivity of clay content prediction to atmospheric effects and degradation of image spatial resolution using Hyperspectral VNIR/SWIR imagery. *Remote Sens. Environ.* **2015**, *164*, 1–15. [[CrossRef](#)]
183. Fassoni-andrade, A.C.; Cauduro, R.; De Paiva, D. Mapping spatial-temporal sediment dynamics of river-floodplains in the Amazon. *Remote Sens. Environ.* **2019**, *221*, 94–107. [[CrossRef](#)]
184. Mariano, D.A.; Carlos, A.C.; Wardlow, B.D.; Anderson, M.C.; Schiltmeyer, A.V.; Tadesse, T.; Svoboda, M.D. Use of remote sensing indicators to assess effects of drought and human-induced land degradation on ecosystem health in Northeastern Brazil. *Remote Sens. Environ.* **2018**, *213*, 129–143. [[CrossRef](#)]
185. Metternicht, G.I. Evaluating the information content of JERS-1 SAR and Landsat TM data for discrimination of soil erosion features. *ISPRS J. Photogramm. Remote Sens.* **1998**, *53*, 143–153. [[CrossRef](#)]
186. Phinzi, K.; Ngetar, N.S. Mapping Soil Erosion in a Quaternary Catchment in Eastern Cape Using Geographic Information System and Remote Sensing. *S. Afr. J. Geomat.* **2017**, *6*, 11–29. [[CrossRef](#)]
187. Eltner, A.; Baumgart, P.; Maas, H.; Faust, D. Multi-temporal UAV data for automatic measurement of rill and interrill erosion on loess soil. *EARTH Surf. Process. Landf.* **2015**, *40*, 741–755. [[CrossRef](#)]
188. Christian, B.A.; Dhinwa, P.S. Long term monitoring and assessment of desertification processes using medium & high resolution satellite data. *Appl. Geogr.* **2018**, *97*, 10–24.
189. Staenz, K.; Mueller, A.; Heiden, U. Overview of terrestrial imaging spectroscopy missions. In Proceedings of the 2013 IEEE International Geoscience and Remote Sensing Symposium—IGARSS, Melbourne, Australia, 21–26 July 2013; pp. 3502–3505.
190. Barnsley, M.J.; Settle, J.J.; Cutter, M.A.; Lobb, D.R.; Teston, F. The PROBA/CHRIS mission: A low-cost smallsat for hyperspectral multiangle observations of the earth surface and atmosphere. *IEEE Trans. Geosci. Remote Sens.* **2004**, *42*, 1512–1520. [[CrossRef](#)]

191. Zhang, B.; Chen, Z.; Li, J.; Gao, L. Image quality evaluation on Chinese first earth observation hyperspectral satellite. *Int. Geosci. Remote Sens. Symp.* **2009**, *1*, I-188–I-191.
192. Kiran Kumar, A.S.; Chowdhury, A.R. Hyper-Spectral Imager in visible and near-infrared band for lunar compositional mapping. *J. Earth Syst. Sci.* **2005**, *114*, 721–724. [[CrossRef](#)]
193. Lewis, M.D.; Gould, R.W.; Arnone, R.A.; Lyon, P.E.; Martinolich, P.M.; Vaughan, R.; Lawson, A.; Scardino, T.; Hou, W.; Snyder, W.; et al. The Hyperspectral Imager for the Coastal Ocean (HICO): Sensor and data processing overview. In Proceedings of the IEEE Oceans, Biloxi, MS, USA, 26–29 October 2009.
194. OSCAR (Observing Systems Capability Analysis and Review Tool. Available online: <http://www.wmo-sat.info/oscar/satellites/view/526> (accessed on 24 March 2019).
195. Lopinto, E.; Ananasso, C. The Prisma Hyperspectral Mission. In Proceedings of the 33rd EARSeL Symposium, Towards Horizon 2020: Earth Observation and Social Perspectives, Matera, Italy, 3–6 June 2013.
196. Iwasaki, A.; Ohgi, N.; Tanii, J.; Kawashima, T.; Inada, H. Hyperspectral Imager Suite (HISUI)-Japanese hyper-multi spectral radiometer. In Proceedings of the 2011 IEEE International Geoscience and Remote Sensing Symposium (IGARSS), Vancouver, BC, Canada, 24–29 July 2011; pp. 1025–1028.
197. Kaufmann, H.; Segl, K.; Chabrillat, S.; Hofer, S.; Stuffer, T.; Mueller, A.; Richter, R.; Schreier, G.; Haydn, R.; Bach, H. EnMAP a hyperspectral sensor for environmental mapping and analysis. In Proceedings of the IEEE International Conference on Geoscience and Remote Sensing Symposium, IGARSS, Denver, CO, USA, 31 July–4 August 2006; IEEE: Piscataway, NJ, USA, 2006; pp. 1617–1619.
198. Rascher, U. FLEX—Fluorescence Explorer: A remote sensing approach to quantify spatio-temporal variations of photosynthetic efficiency from space. *Photosynth. Res.* **2007**, *91*, 1387–1390.
199. Kraft, S.; Del Bello, U.; Bouvet, M.; Drusch, M. Flex: Esa’s Earth Explorer 8 Candidate Mission. In Proceedings of the 2012 IEEE International Geoscience and Remote Sensing Symposium, Munich, Germany, 22–27 July 2012; pp. 7125–7128.
200. Briottet, X.; Marion, R.; Carrere, V.; Jacquemoud, S.; Bourguignon, A.; Chami, M.; Dumont, M.; Minghelli-Roman, A.; Weber, C.; Lefevre-Fonollosa, M.-J.; et al. HYPXIM: HYPXIM: A second generation high spatial resolution hyperspectral satellite for dual applications. In Proceedings of the 5th Workshop on Hyperspectral Image and Signal Processing: Evolution in Remote Sensing (WHISPERS), Gainesville, FL, USA, 26–28 June 2013.
201. Nieke, J.; Rast, M. Towards the Copernicus Hyperspectral Imaging Mission for The Environment (CHIME). In Proceedings of the European Space Agency/ESTEC, Keplerlaan 1, PO Box 299, 2200 AG Noordwijk ZH, The European Space Agency/ESRIN, via Galileo Galilei, Frascati, Rome, Italy, 29 November 2018.
202. Rast, M.; Nieke, J.; Ananasso, C.; Bach, H.; Ben Dor, E.; Chabrillat, S.; Colombo, R.; Feret, J.-B.; Giardino, C.; Green, R.O.; et al. The Copernicus Hyperspectral Imaging Mission for the Environment (CHIME). In Proceedings of the Living Planet Symposium, Milan, Italy, 13–17 May 2019.
203. Ben-Dor, E.; Kafri, A.; Varacalli, G. An Italian–Israeli hyperspectral orbital mission—Update. In Proceedings of the International Geoscience and Remote Sensing Symposium, Quebec, QC, Canada, 13–18 July 2014.
204. Malenovský, Z.; Rott, H.; Cihlar, J.; Schaepman, M.E.; García-Santos, G.; Fernandes, R.; Berger, M. Sentinels for science: Potential of Sentinel-1, -2, and -3 missions for scientific observations of ocean, cryosphere, and land. *Remote Sens. Environ.* **2012**, *120*, 91–101. [[CrossRef](#)]
205. The CEOS Database. Available online: <http://database.eohandbook.com/index.aspx> (accessed on 1 January 2019).
206. Doolittle, J.A.; Minzenmayer, F.E.; Waltman, S.W.; Benham, E.C.; Tuttle, J.W.; Peaslee, S.D. Ground-penetrating radar soil suitability map of the conterminous United States. *Geoderma* **2007**, *141*, 416–421. [[CrossRef](#)]
207. Sexton, J.O.; Song, X.P.; Huang, C.; Channan, S.; Baker, M.E.; Townshend, J.R. Urban growth of the Washington, D.C.-Baltimore, MD metropolitan region from 1984 to 2010 by annual, Landsat-based estimates of impervious cover. *Remote Sens. Environ.* **2013**, *129*, 42–53. [[CrossRef](#)]
208. Webb, R.; Rosenzweig, C.E.; Levine, E.R. *Global Soil Texture and Derived Water-Holding Capacities* (Webb et al.); ORNL DAAC: Oak Ridge, TN, USA, 2000. [[CrossRef](#)]
209. Wilson, M.F.; Henderson-Sellers, A.; Global 1-Degree Vegetation and Soil Types. Research Data Archive at the National Center for Atmospheric Research, Computational and Information Systems Laboratory. 1985. Available online: <http://rda.ucar.edu/datasets/ds767.0/> (accessed on 10 February 2019).
210. Batjes, N.H. *Global Assessment of Soil Phosphorus Retention Potential*; PANGAEA; World Data Centre for Soils: Wageningen, The Netherlands, 2016. [[CrossRef](#)]

211. Petrakis, S.; Barba, J.; Bond-Lamberty, J.; Vargas, R. *Data from: Using Greenhouse Gas Fluxes to Define Soil Functional Types*; Springer International Publishing: Basel, Switzerland, 2017. [[CrossRef](#)]
212. Huang, Y.H.; Jiang, D.; Zhuang, D.F.; Fu, J.Y. Evaluation of Hyperspectral Indices for Chlorophyll-a Concentration Estimation in Tangxun Lake (Wuhan, China). *Int. J. Environ. Res. Public Health* **2010**, *7*, 2437–2451. [[CrossRef](#)] [[PubMed](#)]
213. Hengl, T.; De Jesus, J.M.; MacMillan, R.A.; Batjes, N.H.; Heuvelink, G.B.M.; Ribeiro, E.; Samuel-Rosa, A.; Kempen, B.; Leenaars, J.G.B.; Walsh, M.G.; et al. SoilGrids1km—Global soil information based on automated mapping. *PLoS ONE* **2014**, *9*, e114788. [[CrossRef](#)] [[PubMed](#)]
214. Turner, W.; Spector, S.; Gardiner, N.; Fladeland, M.; Sterling, E.; Steininger, M. Remote sensing for biodiversity science and conservation. *Trends Ecol. Evol.* **2003**, *18*, 306–314. [[CrossRef](#)]
215. McColl, K.A.; Alemohammad, S.H.; Akbar, R.; Konings, A.G.; Yueh, S.; Entekhabi, D. The global distribution and dynamics of surface soil moisture. *Nat. Geosci.* **2017**, *10*, 100–104. [[CrossRef](#)]
216. Seneviratne, S.I.; Corti, T.; Davin, E.L.; Hirschi, M.; Jaeger, E.B.; Lehner, I.; Orlowsky, B.; Teuling, A.J. Earth-Science Reviews Investigating soil moisture—Climate interactions in a changing climate: A review. *Earth Sci. Rev.* **2010**, *99*, 125–161. [[CrossRef](#)]
217. Rabot, E.; Wiesmeier, M.; Schlüter, S.; Vogel, H.J. Soil structure as an indicator of soil functions: A review. *Br. Med. J.* **2018**, *314*, 122–137. [[CrossRef](#)]
218. Vereecken, H.; Huisman, J.A.; Bogen, H.; Vanderborght, J.; Vrugt, J.A.; Hopmans, J.W. On the value of soil moisture measurements in vadose zone hydrology: A review. *WATER Resour. Res.* **2008**, *44*, 1–21. [[CrossRef](#)]
219. Moeslund, J.E.; Arge, L.; Bøcher, P.K.; Dalgaard, T.; Ejrnæs, R.; Odgaard, M.V.; Svenning, J.-C. Topographically controlled soil moisture drives plant diversity patterns within grasslands. *Biodivers. Conserv.* **2013**, *22*, 2151–2166. [[CrossRef](#)]
220. Bardgett, R.D.; Van Der Putten, W.H. Belowground biodiversity and ecosystem functioning. *Nature* **2014**, *515*, 505–511. [[CrossRef](#)]
221. Grossiord, C.; Granier, A.; Gessler, A.; Jucker, T.; Bonal, D. Does Drought Influence the Relationship Between Biodiversity and Ecosystem Functioning in Boreal Forests? *Ecosystems* **2014**, *17*, 394–404. [[CrossRef](#)]
222. Clark, J.S.; Iverson, L.; Woodall, C.W.; Allen, C.D.; Bell, D.M.; Bragg, D.C.; D’Amato, A.W.; Davis, F.W.; Hersh, M.H.; Ibanez, I.; et al. The impacts of increasing drought on forest dynamics, structure, and biodiversity in the United States. *Glob. Chang. Biol.* **2016**, *22*, 2329–2352. [[CrossRef](#)] [[PubMed](#)]
223. Wall, D.H.; Virginia, R.A. Controls on soil biodiversity: Insights from extreme environments. *Appl. Soil Ecol.* **1999**, *13*, 137–150. [[CrossRef](#)]
224. Colliander, A.; Jackson, T.J.; Bindlish, R.; Chan, S.; Das, N.; Kim, S.B.; Cosh, M.H.; Dunbar, R.S.; Dang, L.; Pashaian, L.; et al. Validation of SMAP surface soil moisture products with core validation sites. *Remote Sens. Environ.* **2017**, *191*, 215–231. [[CrossRef](#)]
225. Rodríguez-Fernández, N.; Al Bitar, A.; Colliander, A.; Zhao, T. Soil Moisture Remote Sensing across Scales. *Remote Sens.* **2019**, *11*, 190. [[CrossRef](#)]
226. Zreda, M.; Shuttleworth, W.J.; Zeng, X.; Zweck, C.; Desilets, D.; Franz, T.; Rosolem, R. Sciences COSMOS: The COsmic-ray Soil Moisture Observing System. *Hydrol. Earth Syst. Sci.* **2012**, *16*, 4079–4099. [[CrossRef](#)]
227. Strati, V.; Albéri, M.; Anconelli, S.; Baldoncini, M.; Bittelli, M.; Bottardi, C.; Chiarelli, E.; Fabbri, B.; Guidi, V.; Raptis, K.; et al. Modelling Soil Water Content in a Tomato Field: Proximal Gamma Ray Spectroscopy and Soil-Crop System Models. *Agriculture* **2018**, *8*, 60. [[CrossRef](#)]
228. Huisman, J.A.; Hubbard, S.S.; Redman, J.D.; Annan, A.P. Measuring Soil Water Content with Ground Penetrating Radar: A Review. *Soil Sci. Soc. Am.* **2003**, *2*, 476–491. [[CrossRef](#)]
229. Ulaby, F.T.; Moore, R.K.; Fung, A.K. *Microwave Remote Sensing: Active and Passive Volume II: Radar Remote Sensing and Surface Scattering and Emission Theory*; Artech House Publishers: London, UK, 1986; Volume 2, ISBN 10: 0890061912.
230. Topp, G.C.; Davis, J.L.; Annan, A.P. Electromagnetic Determination of Soil Water Content: Measurements in Coaxial Transmission Lines. *Water Resour. Res.* **1980**, *16*, 574–582. [[CrossRef](#)]
231. Dobson, M.C.; Ulaby, F.T.; Hallikainen, M.T.; El-Rayes, M.A. Microwave Dielectric Behavior of Wet Soil-Part II: Dielectric Mixing Models. *IEEE Trans. Geosci. Remote Sens.* **1985**, *23*, 35–46. [[CrossRef](#)]
232. Mironov, V.L.; Kosolapova, L.G.; Fomin, S.V. Physically and Mineralogically Based Spectroscopic Dielectric Model for Moist Soils. *IEEE Trans. Geosci. Remote Sens.* **2009**, *47*, 2059–2070. [[CrossRef](#)]

233. Entekhabi, D.; Njoku, E.G.; O'Neill, P.E.; Kellogg, K.H.; Crow, W.T.; Edelstein, W.N.; Entin, J.K.; Goodman, S.D.; Jackson, T.J.; Johnson, J.; et al. The soil moisture active passive (SMAP) mission. *Proc. IEEE* **2010**, *98*, 704–716. [[CrossRef](#)]
234. Moreira, A.; Prats, P.; Younis, M.; Krieger, G.; Hajnsek, I.; Papathanassiou, K. A Tutorial on Synthetic Aperture Radar. *IEEE Geosci. Remote Sens. Mag.* **2013**, *1*, 6–43. [[CrossRef](#)]
235. Henderson, F.M.; Lewis, A.J. *Principles and Applications of Imaging Radar (Manual of Remote Sensing, Volume 2)*; WILEY: New York, NY, USA, 1998; Volume 2, ISBN 13: 978-0-471-29406-1.
236. Ulaby, F.T.; Dubois, P.C.; Van Zyl, J. Radar mapping of surface soil moisture. *J. Hydrol.* **1996**, *184*, 57–84. [[CrossRef](#)]
237. Jagdhuber, T. Soil Parameter Retrieval under Vegetation Cover Using SAR Polarimetry. Ph.D. Thesis, University of Potsdam, Institute of Earth and Environmental Sciences Section of Geoecology, Potsdam, Brandenburg, Germany, 2012.
238. Jagdhuber, T.; Hajnsek, I.; Bronstert, A.; Papathanassiou, K.P. Soil Moisture Estimation under Low Vegetation Cover Using a Multi-Angular Polarimetric Decomposition. *IEEE Trans. Geosci. Remote Sens.* **2013**, *51*, 2201–2215. [[CrossRef](#)]
239. Jagdhuber, T.; Hajnsek, I.; Papathanassiou, K.P. An Iterative Generalized Hybrid Decomposition for Soil Moisture Retrieval under Vegetation Cover Using Fully Polarimetric SAR. *IEEE J. Sel. Top. Appl. Earth Obs. Remote Sens.* **2015**, *8*, 3911–3922. [[CrossRef](#)]
240. Fersch, B.; Jagdhuber, T.; Schrön, M.; Völsch, I.; Jäger, M. Synergies for Soil Moisture Retrieval across Scales from Airborne Polarimetric SAR, Cosmic Ray Neutron Roving, and an In Situ Sensor Network. *Water Resour. Res.* **2018**, *54*, 9364–9383. [[CrossRef](#)]
241. Barrett, B.W.; Dwyer, E.; Whelan, P. Soil moisture retrieval from active spaceborne microwave observations: An evaluation of current techniques. *Remote Sens.* **2009**, *1*, 210–242. [[CrossRef](#)]
242. Ahmad, A.; Zhang, Y.; Nichols, S. Review and evaluation of remote sensing methods for soil-moisture estimation. *J. Photonics Energy* **2011**, *2*, 028001.
243. Ali, I.; Greifeneder, F.; Stamenkovic, J.; Neumann, M.; Notarnicola, C. Review of machine learning approaches for biomass and soil moisture retrievals from remote sensing data. *Remote Sens.* **2015**, *7*, 16398–16421. [[CrossRef](#)]
244. Bruckler, L.; Witono, H.; Stengel, P. Near surface soil moisture estimation from microwave measurements. *Remote Sens. Environ.* **1988**, *26*, 101–121. [[CrossRef](#)]
245. Wagner, W.; Lemoine, G.; Rott, H. A method for estimating soil moisture from ERS Scatterometer and soil data. *Remote Sens. Environ.* **1999**, *70*, 191–207. [[CrossRef](#)]
246. Le Hégarat-masclé, S.; Zribi, M.; Alem, F.; Weisse, A.; Loumagne, C. Soil Moisture Estimation from ERS/SAR Data: Toward an Operational Methodology. *Estuaries* **2002**, *40*, 2647–2658. [[CrossRef](#)]
247. Satalino, G.; Mattia, F.; Davidson, M.W.J.; Le Toan, T.; Pasquariello, G.; Borgeaud, M. On current limits of soil moisture retrieval from ERS-SAR data. *IEEE Trans. Geosci. Remote Sens.* **2002**, *40*, 2438–2447. [[CrossRef](#)]
248. Zribi, M.; Le Hégarat-Masclé, S.; Otlé, C.; Kammoun, B.; Guerin, C. Surface soil moisture estimation from the synergistic use of the (multi-incidence and multi-resolution) active microwave ERS Wind Scatterometer and SAR data. *Remote Sens. Environ.* **2003**, *86*, 30–41. [[CrossRef](#)]
249. Baghdadi, N.; Holah, N.; Zribi, M. Soil moisture estimation using multi-incidence and multi-polarization ASAR data. *Int. J. Remote Sens.* **2006**, *27*, 1907–1920. [[CrossRef](#)]
250. Pasolli, L.; Notarnicola, C.; Bertoldi, G.; Bruzzone, L.; Remelgado, R.; Greifeneder, F.; Niedrist, G.; Della Chiesa, S.; Tappeiner, U.; Zebisch, M. Estimation of soil moisture in mountain areas using SVR technique applied to multiscale active radar images at C-band. *IEEE J. Sel. Top. Appl. Earth Obs. Remote Sens.* **2015**, *8*, 262–283. [[CrossRef](#)]
251. Dobson, M.C.; Ulaby, F.T. Preliminary Evaluation of the SIRB Response to Soil Moisture, Surface Roughness, and Crop Canopy Cover. *IEEE Trans. Geosci. Remote Sens.* **1986**, *24*, 517–526. [[CrossRef](#)]
252. Dubois, P.C.; Engman, T. Measuring Soil Moisture with Imaging Radars. *IEEE Trans. Geosci. Remote Sens.* **1995**, *33*, 915–926. [[CrossRef](#)]
253. Bindlish, R.; Jackson, T.J.; Van Der Velde, R. High resolution soil moisture mapping using AIRSAR observations during SMEX02. In Proceedings of the International Geoscience and Remote Sensing Symposium (IGARSS), Denver, CO, USA, 31 July–4 August 2006; pp. 2324–2327.

254. Mattia, F.; Satalino, G.; Dente, L.; Pasquariello, G. Using a priori information to improve soil moisture retrieval from ENVISAT ASAR AP data in semiarid regions. *IEEE Trans. Geosci. Remote Sens.* **2006**, *44*, 900–911. [[CrossRef](#)]
255. Tsang, L.; Kong, J.A.; Ding, K.-H. *Scattering of Electromagnetic Waves: Theories and Applications*; Wiley-Interscience: New York, NY, USA, 2000; Volume 1, ISBN 0471387991.
256. Elfouhaily, T.M.; Guérin, C.-A. A critical survey of approximate scattering wave theories from random rough surfaces. *Waves Random Media* **2004**, *14*, R1–R40. [[CrossRef](#)]
257. Attema, E.P.W.; Ulaby, F.T. Vegetation modeled as a water cloud. *Radio Sci.* **1978**, *13*, 357–364. [[CrossRef](#)]
258. Bracaglia, M.; Ferrazzoli, P.; Guerriero, L. A fully polarimetric multiple scattering model for crops. *Remote Sens. Environ.* **1995**, *54*, 170–179. [[CrossRef](#)]
259. Ulaby, F.T.; Tavakoli, A.; Senior, T.B. Microwave Propagation Constant for a Vegetation Canopy with Vertical Stalks. *IEEE Trans. Geosci. Remote Sens.* **1987**, *25*, 714–725. [[CrossRef](#)]
260. Picard, G.; Le Toan, T.; Mattia, F. Understanding C-band radar backscatter from wheat canopy using a multiple-scattering coherent model. *IEEE Trans. Geosci. Remote Sens.* **2003**, *41*, 1583–1591. [[CrossRef](#)]
261. Ulaby, F.T.; Sarabandi, K.; McDonald, K.; Whitt, M.; Craig Dobson, M. Michigan microwave canopy scattering model. *Int. J. Remote Sens.* **1990**, *11*, 1223–1253. [[CrossRef](#)]
262. Morrison, K.; Bennett, J.C.; Nolan, M.; Menon, R. Laboratory measurement of the dinstar response to spatiotemporal variations in soil moisture. *IEEE Trans. Geosci. Remote Sens.* **2011**, *49*, 3815–3823. [[CrossRef](#)]
263. De Zan, F.; Parizzi, A.; Prats-Iraola, P.; López-Dekker, P. A SAR interferometric model for soil moisture. *IEEE Trans. Geosci. Remote Sens.* **2014**, *52*, 418–425. [[CrossRef](#)]
264. Zwieback, S.; Hensley, S.; Hajnsek, I. Assessment of soil moisture effects on L-band radar interferometry. *Remote Sens. Environ.* **2015**, *164*, 77–89. [[CrossRef](#)]
265. Brocca, L.; Crow, W.T.; Ciabatta, L.; Massari, C.; De Rosnay, P.; Enekel, M.; Hahn, S.; Amarnath, G.; Camici, S.; Tarpanelli, A.; et al. A Review of the Applications of ASCAT Soil Moisture Products. *IEEE J. Sel. Top. Appl. Earth Obs. Remote Sens.* **2017**, *10*, 2285–2306. [[CrossRef](#)]
266. Wagner, W.; Hahn, S.; Kidd, R.; Melzer, T.; Bartalis, Z.; De Rosnay, P.; Jann, A.; Hasenauer, S.; Figa-saldan, J.; Kubu, G.; et al. The ASCAT Soil Moisture Product: A Review of its Specifications, Validation Results, and Emerging Applications. *Meteorol. Z.* **2013**, *22*, 5–33. [[CrossRef](#)]
267. Naeimi, V.; Scipal, K.; Bartalis, Z.; Hasenauer, S.; Wagner, W.; Member, S. An Improved Soil Moisture Retrieval Algorithm for ERS and METOP Scatterometer Observations. *IEEE Trans. Geosci. Remote Sens.* **2009**, *47*, 1999–2013. [[CrossRef](#)]
268. Attema, E.; Borgellini, P.; Edwards, P.; Levirini, G.; Lokos, S.; Moeller, L.; Rosich-Tell, B.; Secchi, P.; Torres, R.; Davidson, M.; et al. *Sentinel-1—The Radar Mission for GMES Land and Sea Services*; Bull-Eur Space, ESA Bulletin: Paris, France, 2007; No. 131; pp. 10–17. ISSN 0376-4265.
269. Bauer-Marschallinger, B.; Paulik, C.; Hochstöger, S.; Mistelbauer, T.; Modanesi, S.; Ciabatta, L.; Massari, C.; Brocca, L.; Wagner, W. Soil moisture from fusion of scatterometer and SAR: Closing the scale gap with temporal filtering. *Remote Sens.* **2018**, *10*, 1030. [[CrossRef](#)]
270. Wigneron, J.-P. Soil moisture retrieval algorithms in the framework of the SMOS mission: Current status and requirements for the EuroSTARRS Campaign. In Proceedings of the First Results Workshop on Eurostarrs, Wise, Losac Campaigns, Toulouse, France, 4–6 November 2002; pp. 199–202.
271. Mo, T.; Choudhury, B.J.; Schmugge, T.J.; Wang, J.R.; Jackson, T.J. A model for microwave emission from vegetation-covered fields. *J. Geophys. Res.* **1982**, *87*, 11229–11237. [[CrossRef](#)]
272. Ulaby, F.T.; Long, D.G. *Microwave Radar and Radiometric Remote Sensing*; The University of Michigan Press: Ann Arbor, MI, USA, 2013; ISBN 978-0-47211-935-6.
273. Brunfeldt, D.R.; Ulaby, F.T. Measured microwave emission and scattering in vegetation canopies. *IEEE Trans. Geosci. Remote Sens.* **1984**, *22*, 520–524. [[CrossRef](#)]
274. Njoku, E.G.; Entekhabi, D. Passive microwave remote sensing of soil moisture. *J. Hydrol.* **1996**, *184*, 101–129. [[CrossRef](#)]
275. Hasan, S.; Montzka, C.; Rüdiger, C.; Ali, M.; Bogena, H.R.; Vereecken, H. Soil moisture retrieval from airborne L-band passive microwave using high resolution multispectral data. *ISPRS J. Photogramm. Remote Sens.* **2014**, *91*, 59–71. [[CrossRef](#)]

276. Kerr, Y.H.Y.H.; Waldteufel, P.; Wigneron, J.-P.J.P.; Martinuzzi, J.M.; Font, J.; Berger, M. Soil moisture retrieval from space: The Soil Moisture and Ocean Salinity (SMOS) mission. *IEEE Trans. Geosci. Remote Sens.* **2001**, *39*, 1729–1735. [[CrossRef](#)]
277. Mladenova, I.E.; Jackson, T.J.; Njoku, E.; Bindlish, R.; Chan, S.; Cosh, M.H.; Holmes, T.R.H.; de Jeu, R.A.M.; Jones, L.; Kimball, J.; et al. Remote monitoring of soil moisture using passive microwave-based techniques—Theoretical basis and overview of selected algorithms for AMSR-E. *Remote Sens. Environ.* **2014**, *144*, 197–213. [[CrossRef](#)]
278. Wigneron, J.P.; Kerr, Y.; Waldteufel, P.; Saleh, K.; Escorihuela, M.J.; Richaume, P.; Ferrazzoli, P.; de Rosnay, P.; Gurney, R.; Calvet, J.C.; et al. L-band Microwave Emission of the Biosphere (L-MEB) Model: Description and calibration against experimental data sets over crop fields. *Remote Sens. Environ.* **2007**, *107*, 639–655. [[CrossRef](#)]
279. Drusch, M.; Holmes, T.; de Rosnay, P.; Balsamo, G. Comparing ERA-40-Based L-Band Brightness Temperatures with Skylab Observations: A Calibration/Validation Study Using the Community Microwave Emission Model. *J. Hydrometeorol.* **2009**, *10*, 213–226. [[CrossRef](#)]
280. Parinussa, R.M.; Holmes, T.R.H.; Wanders, N.; Dorigo, W.A.; De Jeu, R.A.M. A Preliminary Study toward Consistent Soil Moisture from AMSR2. *J. Hydrometeorol.* **2014**, *16*, 932–947. [[CrossRef](#)]
281. Kerr, B.Y.H.; Waldteufel, P.; Wigneron, J.-P.; Delwart, S.; Cabot, F.; Boutin, J.; Escorihuela, M.-J.; Font, J.; Reul, N.; Gruhier, C.; et al. The SMOS Mission: New Tool for Monitoring Key Elements of the Global Water Cycle. *Proc. IEEE* **2010**, *98*, 666–687. [[CrossRef](#)]
282. Entekhabi, D.; Njoku, E.; O'Neill, P.; Spencer, M.; Jackson, T.; Entin, J.; Im, E.; Kellogg, K. The Soil Moisture Active/Passive Mission (SMAP). In Proceedings of the IGARSS 2008 - 2008 IEEE International Geoscience and Remote Sensing Symposium, Boston, MA, USA, 7–11 July 2008; pp. III-1–III-4. [[CrossRef](#)]
283. Liu, Y.Y.; Dorigo, W.A.; Parinussa, R.M.; De Jeu, R.A.M.; Wagner, W.; McCabe, M.F.; Evans, J.P.; Van Dijk, A.I.J.M. Trend-preserving blending of passive and active microwave soil moisture retrievals. *Remote Sens. Environ.* **2012**, *123*, 280–297. [[CrossRef](#)]
284. Entekhabi, D.; Narendra, D.; Njoku, E.; Yueh, S.; Johnson, J.; Shi, J. *Soil Moisture Active Passive (SMAP) Algorithm Theoretical Basis Document SMAP L2 & L3 Radar Soil Moisture (Active) Data Products*, 2014.
285. Das, N.N.; Entekhabi, D.; Member, S.; Njoku, E.G. An algorithm for merging SMAP radiometer and radar data for high-resolution soil-moisture retrieval. *IEEE Trans. Geosci. Remote Sens.* **2011**, *49*, 1504–1512. [[CrossRef](#)]
286. Piles, M.; Camps, A.; Vall-Llossera, M.; Talone, M. Spatial-resolution enhancement of SMOS data: A deconvolution-based approach. *IEEE Trans. Geosci. Remote Sens.* **2009**, *47*, 2182–2192. [[CrossRef](#)]
287. Zhan, X.; Houser, P.R.; Walker, J.P.; Crow, W.T.; Nasa, A.; Science, S. A Method for Retrieving High-Resolution Surface Soil Moisture from Hydros L-Band Radiometer and Radar Observations. *IEEE Trans. Geosci. Remote Sens.* **2006**, *44*, 1534–1544. [[CrossRef](#)]
288. Das, N.N.; Entekhabi, D.; Njoku, E.G.; Shi, J.J.C.; Johnson, J.T.; Colliander, A. Tests of the SMAP combined radar and radiometer algorithm using airborne field campaign observations and simulated data. *IEEE Trans. Geosci. Remote Sens.* **2014**, *52*, 2018–2028. [[CrossRef](#)]
289. Montzka, C.; Rötzer, K.; Bogen, H.R.; Sanchez, N.; Vereecken, H. A New Soil Moisture Downscaling Approach for SMAP, SMOS, and ASCAT by Predicting Sub-Grid Variability. *Remote Sens.* **2018**, *10*, 427. [[CrossRef](#)]
290. Jagdhuber, T.; Konings, A.G.; McColl, K.A.; Alemohammad, S.H.; Das, N.N.; Montzka, C.; Link, M.; Akbar, R.; Entekhabi, D. Physics-Based Modeling of Active and Passive Microwave Covariations over Vegetated Surfaces. *IEEE Trans. Geosci. Remote Sens.* **2018**, *57*, 788–802. [[CrossRef](#)]
291. Jagdhuber, T.; Entekhabi, D.; Das, N.N.; Link, M.; Montzka, C.; Kim, S.; Yueh, S. Microwave Covariation Modelling and Retrieval for the Dual-Frequency Active-Passive Combination of Sentinel-1 and SMAP. In Proceedings of the IGARSS 2017, Fort Worth, TX, USA, 23–28 July 2017.
292. Jagdhuber, T.; Baur, M.; Akbar, R.; Das, N.N.; Link, M.; He, L.; Entekhabi, D. Estimation of active-passive microwave covariation using SMAP and Sentinel-1 data. *Remote Sens. Environ.* **2019**, *225*, 458–468. [[CrossRef](#)]
293. Piles, M.; McColl, K.A.; Entekhabi, D.; Das, N.; Pablos, M. Sensitivity of Aquarius Active and Passive Measurements Temporal Covariability to Land Surface Characteristics. *IEEE Trans. Geosci. Remote Sens.* **2015**, *53*, 4700–4711. [[CrossRef](#)]

294. Rötzer, K.; Montzka, C.; Entekhabi, D.; Konings, A.G.; McColl, K.A.; Piles, M.; Vereecken, H. Relationship between Vegetation Microwave Optical Depth and Cross-Polarized Backscatter from multi-Year Aquarius Observations. *IEEE J. Sel. Top. Appl. Earth Obs. Remote Sens.* **2017**, *10*, 4493–4503. [[CrossRef](#)]
295. Das, N.N.; Entekhabi, D.; Kim, S.; Yueh, S.; Dunbar, R.S.; Colliander, A. *SMAP/Sentinel-1 L2 Radiometer/Radar 30-Second Scene 3 km EASE-Grid Soil Moisture, Version 1*; NASA National Snow and Ice Data Center Distributed Active Archive Center: Boulder, CO, USA, 2017. [[CrossRef](#)]
296. Jagdhuber, T.; Entekhabi, D.; Das, N.N.; Baur, M.; Kim, S.; Yueh, S.; Link, M. Physically-based covariation modelling and retrieval for mono-(LL) and multi-frequency (LC) active-passive microwave data from SMAP and Sentinel-1. In Proceedings of the 3rd Satellite Soil Moisture Validation and Application Workshop, New York, NY, USA, 21–22 September 2016.
297. Pause, M.; Schulz, K.; Zacharias, S.; Lausch, A. Near-surface soil moisture estimation by combining airborne L-band brightness temperature observations and imaging hyperspectral data at the field scale. *J. Appl. Remote Sens.* **2012**, *6*, 063516.
298. Montzka, C.; Grant, J.P.; Moradkhani, H.; Franssen, H.-J.H.; Weihermüller, L.; Drusch, M.; Vereecken, H. Estimation of Radiative Transfer Parameters from L-Band Passive Microwave Brightness Temperatures Using Advanced Data Assimilation. *Vadose Zone J.* **2013**, *12*. [[CrossRef](#)]
299. Reigber, A.; Scheiber, R.; Jager, M.; Prats-Iraola, P.; Hajnsek, I.; Jagdhuber, T.; Papathanassiou, K.P.; Nannini, M.; Aguilera, E.; Baumgartner, S.; et al. Very-high-resolution airborne synthetic aperture radar imaging: Signal processing and applications. *Proc. IEEE* **2013**, *101*, 759–783. [[CrossRef](#)]
300. Horn, R.; Jaeger, M.; Keller, M.; Limbach, M.; Nottensteiner, A.; Reigber, A.; Scheiber, R. F-SAR—Recent Upgrades and Campaign Activities. In Proceedings of the 18th International Radar Symposium IRS 2017, Prague, Czech Republic, 28–30 June 2017; pp. 2–11.
301. Montzka, C.; Jagdhuber, T.; Horn, R.; Bogena, H.R.; Hajnsek, I.; Reigber, A.; Vereecken, H. Investigation of SMAP fusion algorithms with airborne active and passive L-Band microwave remote sensing. *IEEE Trans. Geosci. Remote Sens.* **2016**, *54*, 3878–3889. [[CrossRef](#)]
302. Panciera, R.; Walker, J.P.; Jackson, T.J.; Gray, D.A.; Tanase, M.A.; Ryu, D.; Monerris, A.; Yardley, H.; Rüdiger, C.; Wu, X.; et al. (SMAPEX): Toward Soil Moisture Retrieval from the SMAP Mission. *IEEE Trans. Geosci. Remote Sens.* **2014**, *52*, 490–507. [[CrossRef](#)]
303. Bindlish, R.; Jackson, T.; Sun, R.; Cosh, M.; Yueh, S.; Dinardo, S. Combined passive and active microwave observations of soil moisture during CLASIC. *IEEE Geosci. Remote Sens. Lett.* **2009**, *6*, 644–648. [[CrossRef](#)]
304. Konings, A.G.; Entekhabi, D.; Moghaddam, M.; Saatchi, S.S. The Effect of a Variable Soil Moisture Profile on P-band Backscatter Estimation. *IEEE Trans. Geosci. Remote Sens.* **2014**, *52*, 6315–6325. [[CrossRef](#)]
305. Kumar, S.V.; Peters-Lidard, C.D.; Mocko, D.; Reichle, R.; Liu, Y.; Arsenault, K.R.; Xia, Y.; Ek, M.; Riggs, G.; Livneh, B.; et al. Assimilation of Remotely Sensed Soil Moisture and Snow Depth Retrievals for Drought Estimation. *J. Hydrometeorol.* **2014**, *15*, 2446–2469. [[CrossRef](#)]
306. Montzka, C.; Moradkhani, H.; Weihermüller, L.; Franssen, H.J.H.; Canty, M.; Vereecken, H. Hydraulic parameter estimation by remotely-sensed top soil moisture observations with the particle filter. *J. Hydrol.* **2011**, *399*, 410–421. [[CrossRef](#)]
307. Dumedah, G.; Walker, J.P. Intercomparison of the JULES and CABLE land surface models through assimilation of remotely sensed soil moisture in southeast Australia. *Adv. Water Resour.* **2014**, *74*, 231–244. [[CrossRef](#)]
308. Ridler, M.-E.; Madsen, H.; Stisen, S.; Bircher, S.; Fensholt, R. Assimilation of SMOS-derived soil moisture in a fully integrated hydrological and soil-vegetation-atmosphere transfermodel in Western Denmark. *Water Resour. Res.* **2014**, *50*, 8962–8981. [[CrossRef](#)]
309. Han, X.; Franssen, H.-J.H.; Montzka, C.; Vereecken, H. Soilmoisture and soil properties estimation in the Community Land Model with synthetic brightness temperature observations. *Water Resour. Res.* **2015**, *51*, 8757–8772.
310. Rains, D.; Han, X.; Lievens, H.; Montzka, C.; Verhoest, N.E.C. SMOS brightness temperature assimilation into the Community Land Model. *Hydrol. Earth Syst. Sci. Discuss.* **2017**, *21*, 5929–5951. [[CrossRef](#)]
311. Kornelsen, K.C.; Coulibaly, P. Advances in soil moisture retrieval from synthetic aperture radar and hydrological applications. *J. Hydrol.* **2013**, *476*, 460–489. [[CrossRef](#)]
312. Wilson, S.M. Use of vegetation-based methods for soil quality assessment in Scottish forestry: A review. *Scott. For.* **2009**, *63*, 20–29.

313. Rudolph, S.; van der Kruk, J.; von Hebel, C.; Ali, M.; Herbst, M.; Montzka, C.; Pätzold, S.; Robinson, D.A.; Vereecken, H.; Weihermüller, L. Linking satellite derived LAI patterns with subsoil heterogeneity using large-scale ground-based electromagnetic induction measurements. *Geoderma* **2015**, *241–242*, 262–271. [[CrossRef](#)]
314. Piles, M.; Ballabrera-Poy, J.; Muñoz-Sabater, J. Dominant Features of Global Surface Soil Moisture Variability Observed by the SMOS Satellite. *Remote Sens.* **2019**, *11*, 95. [[CrossRef](#)]
315. Huo, A.; Zhang, J.; Cheng, Y.; Yi, X.; Qiao, L.; Su, F.; Du, Y.; Mao, H. Assessing the effect of scaling methods on retrieval of soil moisture based on MODIS images in arid regions. *Toxicol. Environ. Chem.* **2016**, *98*, 410–418. [[CrossRef](#)]
316. Li, B.; Ti, C.; Zhao, Y.; Yan, X. Estimating soil moisture with Landsat data and its application in extracting the spatial distribution of winter flooded paddies. *Remote Sens.* **2016**, *8*, 38. [[CrossRef](#)]
317. Haubrock, S.-N.; Chabrillat, S.; Kuhnert, M.; Hostert, P.; Kaufmann, H. Surface soil moisture quantification and validation based on hyperspectral data and field measurements. *J. Appl. Remote Sens.* **2008**, *2*, 023552. [[CrossRef](#)]
318. Rozenstein, O.; Agam, N.; Serio, C.; Masiello, G.; Venafrà, S.; Achal, S.; Puckrin, E.; Karnieli, A. Diurnal emissivity dynamics in bare versus biocrusted sand dunes. *Sci. Total Environ.* **2015**, *506–507*, 422–429. [[CrossRef](#)]
319. Martini, E.; Wollschläger, U.; Kögler, S.; Behrens, T.; Dietrich, P.; Reinstorf, F.; Schmidt, K.; Weiler, M.; Werban, U. Spatial and Temporal Dynamics of Hillslope-Scale Soil Moisture Patterns: Characteristic States and Transition Mechanisms. *Vadose Zone J.* **2013**, *14*. [[CrossRef](#)]
320. Mitrofanov, I. Maps of Subsurface Hydrogen from the High Energy Neutron Detector, Mars Odyssey. *Science* **2002**, *297*, 78–81. [[CrossRef](#)] [[PubMed](#)]
321. Baldoncini, M.; Albéri, M.; Bottardi, C.; Chiarelli, E.; Raptis, K.G.C.; Strati, V.; Mantovani, F. Investigating the potentialities of Monte Carlo simulation for assessing soil water content via proximal gamma-ray spectroscopy. *J. Environ. Radioact.* **2018**, *192*, 105–116. [[CrossRef](#)] [[PubMed](#)]
322. Dierke, C.; Werban, U. Relationships between gamma-ray data and soil properties at an agricultural test site. *Geoderma* **2013**, *199*, 90–98. [[CrossRef](#)]
323. Siemon, B.; Costabel, S.; Voß, W.; Meyer, U.; Deus, N.; Elbracht, J.; Günther, T.; Wiederhold, H. Airborne and ground geophysical mapping of coastal clays in Eastern Friesland, Germany. *Geophysics* **2015**, *80*, WB21–WB34. [[CrossRef](#)]
324. Priori, S.; Bianconi, N.; Fantappiè, M.; Pellegrini, S.; Ferrigno, G.; Guaitoli, F.; Costantini, E.A. EQA—Environmental quality/Qualité de l’Environnement/Qualità ambientale, 11 (2013) 29–38. *EQA Int. J. Environ. Qual.* **2013**, *11*, 29–38.
325. Guastaldi, E.; Baldoncini, M.; Bezzon, G.; Broggin, C.; Buso, G.; Cacioli, A.; Carmignani, L.; Callegari, I.; Colonna, T.; Dule, K.; et al. A multivariate spatial interpolation of airborne γ -ray data using the geological constraints. *Remote Sens. Environ.* **2013**, *137*, 1–11. [[CrossRef](#)]
326. Carroll, T.R. Airborne soil moisture measurement using natural terrestrial gamma radiation. *Soil Sci.* **1981**, *132*, 358–366. [[CrossRef](#)]
327. Warren, K.J.; Carroll, T.R. Error analysis of airborne gamma radiation soil moisture measurements. *Agric. Meteorol.* **1983**, *28*, 19–30.
328. Köhli, M.; Schrön, M.; Zreda, M.; Schmidt, U.; Dietrich, P.; Zacharias, S. Footprint characteristics revised for field-scale soil moisture monitoring with cosmic-ray neutrons. *Water Resour. Res.* **2015**, *51*, 5772–5790. [[CrossRef](#)]
329. Desilets, D.; Zreda, M.; Ferré, T.P.A. Nature’s neutron probe: Land surface hydrology at an elusive scale with cosmic rays. *Water Resour. Res.* **2010**, *46*, W11505. [[CrossRef](#)]
330. Baatz, R.; Bogena, H.R.; Hendricks Franssen, H.-J.; Huisman, J.A.; Montzka, C.; Vereecken, H. An empirical vegetation correction for soil water content quantification using cosmic ray probes. *Water Resour. Res.* **2015**, *51*, 2030–2046. [[CrossRef](#)]
331. Schattan, P.; Baroni, G.; Oswald, S.E.; Schöber, J.; Fey, C.; Kormann, C.; Huttenlau, M.; Achleitner, S. Continuous monitoring of snowpack dynamics in alpine terrain by aboveground neutron sensing. *Water Resour. Res.* **2017**, *53*, 3615–3634. [[CrossRef](#)]

332. Schrön, M.; Zacharias, S.; Womack, G.; Köhli, M.; Desilets, D.; Oswald, S.E.; Bumberger, J.; Mollenhauer, H.; Kögler, S.; Remmler, P.; et al. Intercomparison of cosmic-ray neutron sensors and water balance monitoring in an urban environment. *Geosci. Instrum. Methods Data Syst.* **2018**, *7*, 83–99. [[CrossRef](#)]
333. Franz, T.E.; Wang, T.; Avery, W.; Finkenbinder, C.; Brocca, L. Combined analysis of soil moisture measurements from roving and fixed cosmic ray neutron probes for multiscale real-time monitoring. *Geophys. Res. Lett.* **2015**, *42*, 3389–3396. [[CrossRef](#)]
334. Schrön, M.; Rosolem, R.; Köhli, M.; Piussi, L.; Schröter, I.; Iwema, J.; Kögler, S.; Oswald, S.E.; Wollschläger, U.; Samaniego, L.; et al. Cosmic-ray Neutron Rover Surveys of Field Soil Moisture and the Influence of Roads. *Water Resour. Res.* **2018**, *54*, 6441–6459. [[CrossRef](#)]
335. Schrön, M. Cosmic-Ray Neutron Sensing and Its Applications to Soil and Land Surface Hydrology. Ph.D. Thesis, University of Potsdam, Potsdam, Germany, 2017. Available online: <https://nbn-resolving.org/urn:nbn:de:kobv:517-opus4-395433> (accessed on 02 October 2019).
336. Chrisman, B.; Zreda, M. Quantifying mesoscale soil moisture with the cosmic-ray rover. *Hydrol. Earth Syst. Sci.* **2013**, *17*, 5097–5108. [[CrossRef](#)]
337. Montzka, C.; Bogena, H.R.; Zreda, M.; Monerris, A.; Morrison, R.; Muddu, S.; Vereecken, H. Validation of Spaceborne and Modelled Surface Soil Moisture Products with Cosmic-Ray Neutron Probes. *Remote Sens.* **2017**, *9*, 103. [[CrossRef](#)]
338. Chakrabarti, S.; Bongiovanni, T.; Judge, J.; Zotarelli, L.; Bayer, C. Assimilation of SMOS soil moisture for quantifying drought impacts on crop yield in agricultural regions. *IEEE J. Sel. Top. Appl. Earth Obs. Remote Sens.* **2014**, *7*, 3867–3879. [[CrossRef](#)]
339. Merlin, O.; Walker, J.P.; Kalma, J.D.; Kim, E.J.; Hacker, J.; Panciera, R.; Young, R.; Summerell, G.; Hornbuckle, J.; Hafeez, M.; et al. The NAFE'06 data set: Towards soil moisture retrieval at intermediate resolution. *Adv. Water Resour.* **2008**, *31*, 1444–1455. [[CrossRef](#)]
340. Kankaku, Y.; Osawa, Y.; Suzuki, S.; Watanabe, T. The Overview of the L-band SAR Onboard ALOS-2. *PIERS Proc. Moscow Russ.* **2009**, *2*, 18–21.
341. Imaoka, K.; Maeda, T.; Kachi, M.; Kasahara, M.; Ito, N.; Nakagawa, K. "Status of AMSR2 Instrument on GCOM-W1". *Proc. SPIE* **2012**, 8528. [[CrossRef](#)]
342. Gaiser, P.W.; St Germain, K.M.; Twarog, E.M.; Poe, G.A.; Purdy, W.; Richardson, D.; Grossman, W.; Jones, W.L.; Spencer, D.; Golba, G.; et al. The windSat spaceborne polarimetric microwave radiometer: Sensor description and early orbit performance. *IEEE Trans. Geosci. Remote Sens.* **2004**, *42*, 2347–2361. [[CrossRef](#)]
343. Bartalis, Z.; Wagner, W.; Naeimi, V.; Hasenauer, S.; Scipal, K.; Bonekamp, H.; Figa, J.; Anderson, C. Initial soil moisture retrievals from the METOP-A Advanced Scatterometer (ASCAT). *Geophys. Res. Lett.* **2007**, *34*, 5–9. [[CrossRef](#)]
344. Morena, L.C.; James, K.V.; Beck, J. Technical Note/Note technique An introduction to the RADARSAT-2 mission. *Can. J. Remote Sens.* **2004**, *30*, 221–234. [[CrossRef](#)]
345. Misra, T.; Rana, S.S.; Desai, N.M.; Dave, Rajeevjyoti, D.B.; Arora, R.K.; Rao, C.V.N.; Bakori, B.V.; Neelakantan, R.; Vachchani, J.G. Synthetic Aperture Radar payload on-board RISAT-1: Configuration, technology and performance. *Curr. Sci.* **2013**, *104*, 446–461.
346. Torres, R.; Snoeij, P.; Geudtner, D.; Bibby, D.; Davidson, M.; Attema, E.; Potin, P.; Rommen, B.; Floury, N.; Brown, M.; et al. GMES Sentinel-1 mission. *Remote Sens. Environ.* **2012**, *120*, 9–24. [[CrossRef](#)]
347. Krieger, G.; Moreira, A.; Fiedler, H.; Hajnsek, I.; Werner, M.; Younis, M.; Zink, M. TanDEM-X: A satellite formation for high-resolution SAR interferometry. *IEEE Trans. Geosci. Remote Sens.* **2007**, *45*, 3317–3340. [[CrossRef](#)]
348. Werninghaus, R.; Buckreuss, S. The TerraSAR-X mission and system design. *IEEE Trans. Geosci. Remote Sens.* **2010**, *48*, 606–614. [[CrossRef](#)]
349. Pasolli, L.; Notarnicola, C.; Bertoldi, G.; Della Chiesa, S.; Niedrist, G.; Bruzzone, L.; Tappeiner, U.; Zebisch, M. Soil moisture monitoring in mountain areas by using high-resolution SAR images: Results from a feasibility study. *Eur. J. Soil Sci.* **2014**, *65*, 852–864. [[CrossRef](#)]
350. Panciera, R.; Walker, J.P.; Kalma, J.D.; Kim, E.J.; Member, S.; Hacker, J.M.; Merlin, O.; Berger, M.; Skou, N.; The, A.; et al. The NAFE' 05/CoSMOS Data Set: Toward SMOS Soil Moisture Retrieval, Downscaling, and Assimilation. *Cosmos* **2008**, *46*, 1–10. [[CrossRef](#)]
351. Jiang, T.; Zhao, K.; Zheng, X.; Chen, S.; Wan, X. Dynamic bp in the L Band and Its Role in Improving the Accuracy of Soil Moisture Retrieval. *Chin. Geogr. Sci.* **2019**, *29*, 283–292. [[CrossRef](#)]

352. Panciera, R.; Walker, J.P.; Kim, E.; Kalma, J.; Merlin, O.; Oxley, L.; Kulasiri, D. Effect of Spatial Scale on Soil Moisture Retrieval from Passive Microwave Sensors. In Proceedings of the Modsim 2007 International Congress on Modelling and Simulation, Christchurch, New Zealand, 10–13 December 2007; pp. 2576–2582.
353. Narayan, U.; Lakshmi, V.; Njoku, E.G. Retrieval of soil moisture from passive and active L/S band sensor (PALS) observations during the Soil Moisture Experiment in 2002 (SMEX02). *Remote Sens. Environ.* **2004**, *92*, 483–496. [[CrossRef](#)]
354. Kim, J.; Hogue, T.S. Improving spatial soil moisture representation through integration of AMSR-E and MODIS products. *IEEE Trans. Geosci. Remote Sens.* **2012**, *50*, 446–460. [[CrossRef](#)]
355. Jarmer, T.; Lavée, H.; Sarah, P.; Hill, J. Using reflectance spectroscopy and landsat data to assess soil inorganic carbon in the Judean Desert (Israel). In *Recent Advances in Remote Sensing and Geoinformation Processing for Land Degradation Assessment*; Röder, A., Hill, J., Eds.; CRC Press: London, UK, 2009; pp. 227–243. ISBN 9780203875445.
356. Zhang, Z.; He, G.; Wang, M.; Long, T.; Wang, G.; Zhang, X.; Jiao, W. Towards an operational method for land surface temperature retrieval from Landsat 8 data. *Remote Sens. Lett.* **2016**, *7*, 279–288. [[CrossRef](#)]
357. Sobrino, J.A.; Franch, B.; Mattar, C.; Jiménez-muñoz, J.C.; Corbari, C. A method to estimate soil moisture from Airborne Hyperspectral Scanner (AHS) and ASTER data: Application to SEN2FLEX and SEN3EXP campaigns. *Remote Sens. Environ.* **2012**, *117*, 415–428. [[CrossRef](#)]
358. Gao, Q.; Zribi, M.; Escorihuela, M.J. Synergetic Use of Sentinel-1 and Sentinel-2 Data for Soil Moisture Mapping at 100 m Resolution. *Sensors* **2017**, *17*, 1966. [[CrossRef](#)] [[PubMed](#)]
359. Fabre, S.; Briottet, X.; Lesaignoux, A.; Avenue, B.P.; Belin, E.; Cedex, F.-T. Estimation of Soil Moisture Content from the Spectral Reflectance of Bare Soils in the 0.4–2.5 μm Domain. *Sensors* **2015**, *15*, 3262–3281. [[CrossRef](#)] [[PubMed](#)]
360. Klinke, R.; Kuechly, H.; Frick, A.; Förster, M.; Schmidt, T.; Holtgrave, A.K.; Kleinschmit, B.; Spengler, D.; Neumann, C. Indicator-Based Soil Moisture Monitoring of Wetlands by Utilizing Sentinel and Landsat Remote Sensing Data. *Photogramm. Remote Sens. Geoinf. Sci.* **2018**, *86*, 71–84. [[CrossRef](#)]
361. Dorigo, W.A.; Wagner, W.; Hohensinn, R.; Hahn, S.; Paulik, C.; Xaver, A.; Gruber, A.; Drusch, M.; Mecklenburg, S.; Van Oevelen, P.; et al. The International Soil Moisture Network: A data hosting facility for global in situ soil moisture measurements. *Hydrol. Earth Syst. Sci.* **2011**, *15*, 1675–1698. [[CrossRef](#)]
362. Das, N.N.; Entekhabi, D.; Dunbar, R.S.; Chaubell, M.J.; Colliander, A.; Yueh, S.; Jagdhuber, T.; Chen, F.; Crow, W.; O'Neill, P.E.; et al. The SMAP and Copernicus Sentinel 1A/B microwave active-passive high resolution surface soil moisture product. *Remote Sens. Environ.* **2019**, *233*, 111380. [[CrossRef](#)]
363. Colliander, A.; Jackson, T.J.; Chan, S.K.; Neill, P.O.; Bindlish, R.; Cosh, M.H.; Caldwell, T.; Walker, J.P.; Berg, A.; McNairn, H.; et al. An assessment of the differences between spatial resolution and grid size for the SMAP enhanced soil moisture product over homogeneous sites. *Remote Sens. Environ.* **2018**, *207*, 65–70. [[CrossRef](#)]
364. Bitar, A.A.; Mialon, A.; Kerr, Y.H.; Cabot, F.; Richaume, P.; Jacqueline, E.; Quesney, A.; Mahmoodi, A.; Tarot, S.; Parrens, M.; et al. The global SMOS Level 3 daily soil moisture and brightness temperature maps. *Earth Syst. Sci. Data* **2017**, *9*, 293–315. [[CrossRef](#)]
365. Rodell, M.; Houser, P.R.; Jambor, U.; Gottschalck, J.; Mitchell, K.; Meng, C.-J.; Arsenault, K.; Cosgrove, B.; Radakovich, J.; Bosilovich, M.; et al. The Global Land Data Assimilation System. *Bull. Am. Meteorol. Soc.* **2004**, *85*, 381–394. [[CrossRef](#)]
366. Houborg, R.; Rodell, M.; Li, B.; Reichle, R.; Zaitchik, B.F. Drought indicators based on model-assimilated Gravity Recovery and Climate Experiment (GRACE) terrestrial water storage observations. *Water Resour. Res.* **2012**, *48*. [[CrossRef](#)]
367. Kustas, W.P.; French, A.N.; Hatfield, J.L.; Jackson, T.J.; Susan Moran, M.; Rango, A.; Ritchie, J.C.; Schmugge, T.J.; Moran, M.S.; Rango, A.; et al. Remote Sensing Research in Hydrometeorology. *Photogramm. Eng. Remote Sens.* **2003**, *69*, 631–646. [[CrossRef](#)]
368. Karnieli, A.; Agam, N.; Pinker, R.T.; Anderson, M.; Imhoff, M.L.; Gutman, G.G.; Panov, N.; Goldberg, A. Use of NDVI and land surface temperature for drought assessment: Merits and limitations. *J. Clim.* **2010**, *23*, 618–633. [[CrossRef](#)]
369. Zink, M. Conditioning a Hydrologic Model Using Patterns of Remotely Sensed Land Surface Temperature. *Water Resour. Res.* **2018**, *54*, 2976–2998. [[CrossRef](#)]
370. Li, Z.-L.; Tang, B.-H.; Wu, H.; Ren, H.; Yan, G.; Wan, Z.; Trigo, I.F.; Sobrino, J.A. Satellite-derived land surface temperature: Current status and perspectives. *Remote Sens. Environ.* **2013**, *131*, 14–37. [[CrossRef](#)]

371. Costa, J.M.; Grant, O.M.; Chaves, M.M. Thermography to explore plant—Environment interactions. *J. Exp. Bot.* **2013**, *64*, 3937–3949. [[CrossRef](#)]
372. Townshend, J.R.; Justice, C.O.; Skole, D.; Malingreau, J.P.; Cihlar, J.; Teillet, P.; Sadowski, F.; Ruttenberg, S. The 1 km resolution global data set: Needs of the international geosphere biosphere programme! *Int. J. Remote Sens.* **1994**, *15*, 3417–3441. [[CrossRef](#)]
373. Weber, N.; Haase, D.; Franck, U. Science of the Total Environment Zooming into temperature conditions in the city of Leipzig: How do urban built and green structures influence earth surface temperatures in the city? *Sci. Total Environ.* **2014**, *496*, 289–298. [[CrossRef](#)] [[PubMed](#)]
374. Kalma, J.D.; McVicar, T.R.; McCabe, M.F. Estimating land surface evaporation: A review of methods using remotely sensed surface temperature data. *Surv. Geophys.* **2008**, *29*, 421–469. [[CrossRef](#)]
375. Hansen, J.; Ruedy, R.; Sato, M.; Lo, K. Global surface temperature change. *Rev. Geophys.* **2010**, *48*. [[CrossRef](#)]
376. Krajewski, W.F.; Anderson, M.C.; Eichinger, W.E.; Entekhabi, D.; Hornbuckle, B.K.; Houser, P.R.; Katul, G.G.; Kustas, W.P.; Norman, J.M.; Peters-Lidard, C.; et al. A remote sensing observatory for hydrologic sciences: A genesis for scaling to continental hydrology. *Water Resour. Res.* **2006**, *42*, 1–13. [[CrossRef](#)]
377. Brenner, C.; Zeeman, M.; Bernhardt, M.; Schulz, K. Estimation of evapotranspiration of temperate grassland based on high-resolution thermal and visible range imagery from unmanned aerial systems. *Int. J. Remote Sens.* **2018**, *39*, 5141–5174. [[CrossRef](#)]
378. Brenner, C.; Thiem, C.E.; Wizemann, H.D.; Bernhardt, M.; Schulz, K. Estimating spatially distributed turbulent heat fluxes from high-resolution thermal imagery acquired with a UAV system. *Int. J. Remote Sens.* **2017**, *38*, 3003–3026. [[CrossRef](#)]
379. Bonan, G.B. Ecological Climatology: Concepts and Applications, 2nd Edition. *Geogr. Res.* **2008**, *48*, 221–222.
380. Müller, B.; Bernhardt, M.; Schulz, K. Identification of catchment functional units by time series of thermal remote sensing images. *Hydrol. Earth Syst. Sci.* **2014**, *18*, 5345–5359. [[CrossRef](#)]
381. Neteler, M. Estimating daily land surface temperatures in mountainous environments by reconstructed MODIS LST data. *Remote Sens.* **2010**, *2*, 333–351. [[CrossRef](#)]
382. Li, Z.-L.; Becker, F. Feasibility of land surface temperature and emissivity determination from AVHRR data. *Remote Sens. Environ.* **1993**, *43*, 67–85. [[CrossRef](#)]
383. Hoffmann, H.; Nieto, H.; Jensen, R.; Guzinski, R.; Zarco-Tejada, P.; Friborg, T. Estimating evaporation with thermal UAV data and two-source energy balance models. *Hydrol. Earth Syst. Sci.* **2016**, *20*, 697–713. [[CrossRef](#)]
384. Malbêteau, Y.; Parkes, S.; Aragon, B.; Rosas, J.; McCabe, M.F. Capturing the diurnal cycle of land surface temperature using an unmanned aerial vehicle. *Remote Sens.* **2018**, *10*, 1407. [[CrossRef](#)]
385. Ghent, D.; Veal, K.; Trent, T.; Remedios, J. A New Approach to Defining Uncertainties for MODIS Land Surface Temperature. *Remote Sens.* **2019**, *11*, 1021. [[CrossRef](#)]
386. Raoufi, R.; Beighley, E. Estimating daily global evapotranspiration using penman-monteith equation and remotely sensed land surface temperature. *Remote Sens.* **2017**, *9*, 1138. [[CrossRef](#)]
387. Coll, C.; Caselles, V.; Galve, J.M.; Valor, E.; Niclòs, R.; Sánchez, J.M.; Rivas, R. Ground measurements for the validation of land surface temperatures derived from AATSR and MODIS data. *Remote Sens. Environ.* **2005**, *97*, 288–300. [[CrossRef](#)]
388. Hook, S.J.; Vaughan, R.G.; Tonooka, H.; Schladow, S.G. Absolute Radiometric in-Flight Validation of Mid Infrared and Thermal Infrared Data from ASTER and MODIS on the Terra Spacecraft Automated Validation Site. *IEEE Trans. Geosci. Remote Sens.* **2007**, *45*, 1798–1807. [[CrossRef](#)]
389. Cristóbal, J.; Jiménez-Muñoz, J.C.; Sobrino, J.A.; Ninyerola, M.; Pons, X. Improvements in land surface temperature retrieval from the Landsat series thermal band using water vapor and air temperature. *J. Geophys. Res. Atmos.* **2009**, *114*, 1–16. [[CrossRef](#)]
390. Jiménez-Muñoz, J.C.; Cristóbal, J.; Sobrino, J.A.; Soria, G.; Ninyerola, M.; Pons, X. Revision of the single-channel algorithm for land surface temperature retrieval from landsat thermal-infrared data. *IEEE Trans. Geosci. Remote Sens.* **2009**, *47*, 339–349. [[CrossRef](#)]
391. Rozenstein, O.; Qin, Z.; Derimian, Y.; Karnieli, A. Derivation of Land Surface Temperature for Landsat-8 TIRS Using a Split Window Algorithm. *Sensors* **2014**, *14*, 5768–5780. [[CrossRef](#)] [[PubMed](#)]
392. Petitcolin, F.; Nerry, F.; Stoll, M.P. Mapping temperature independent spectral indice of emissivity and directional emissivity in AVHRR channels 4 and 5. *Int. J. Remote Sens.* **2002**, *23*, 3473–3491. [[CrossRef](#)]

393. Pinheiro, A.C.T.; Privette, J.L.; Mahoney, R.; Tucker, C.J. Directional effects in a daily AVHRR land surface temperature dataset over Africa. *IEEE Trans. Geosci. Remote Sens.* **2004**, *42*, 1941–1954. [[CrossRef](#)]
394. Coll, C.; Caselles, V.; Valor, E.; Niclòs, R.; Sánchez, J.M.; Galve, J.M.; Mira, M. Temperature and emissivity separation from ASTER data for low spectral contrast surfaces. *Remote Sens. Environ.* **2007**, *110*, 162–175. [[CrossRef](#)]
395. Guzinski, R.; Nieto, H. Evaluating the feasibility of using Sentinel-2 and Sentinel-3 satellites for high-resolution evapotranspiration estimations. *Remote Sens. Environ.* **2019**, *221*, 157–172. [[CrossRef](#)]
396. Qing, S.; Zhang, J.; Cui, T.; Bao, Y. Retrieval of sea surface salinity with MERIS and MODIS data in the Bohai Sea. *Remote Sens. Environ.* **2013**, *136*, 117–125. [[CrossRef](#)]
397. Jiang, G.-M.; Li, Z.-L. Split-window algorithm for land surface temperature estimation from MSG1-SEVIRI data. *Int. J. Remote Sens.* **2008**, *29*, 6067–6074. [[CrossRef](#)]
398. Huang, M.; Lee, P.; Mcnider, R.; Crawford, J.; Buzay, E.; Barrick, J.; Liu, Y.; Krishnan, P. Temporal and spatial variability of daytime land surface temperature in Houston: Comparing DISCOVER-AQ aircraft observations with the WRF model and satellites. *J. Geophys. Res. Atmos.* **2016**, *121*, 185–195. [[CrossRef](#)]
399. Sobrino, J.A.; Jiménez-muñoz, J.C.; Zarco-tejada, P.J.; Sepulcre-cantó, G.; De Miguel, E. Land surface temperature derived from airborne hyperspectral scanner thermal infrared data. *Remote Sens. Environ.* **2006**, *102*, 99–115. [[CrossRef](#)]
400. Adler-Golden, S.; Conforti, P.; Gagnon, M.A.; Tremblay, P.; Chamberland, M. Remote sensing of surface emissivity with the telops Hyper-Cam. In Proceedings of the 2014 6th Workshop on Hyperspectral Image and Signal Processing: Evolution in Remote Sensing (WHISPERS), Lausanne, Switzerland, 24–27 June 2014; pp. 9–12.
401. Gagnon, M.-A.; Tremblay, P.; Savary, S.; Farley, V.; Lagueux, P.; Chamberland, M. Airborne thermal hyperspectral imaging of urban and rural areas. In Proceedings of the 2014 IEEE Geoscience and Remote Sensing Symposium, Quebec, QC, Canada, 13–18 July 2014; IEEE: Piscataway, NJ, USA, 2014; pp. 1369–1372.
402. Galleguillos, M.; Jacob, F.; Prévot, L.; French, A.; Lagacherie, P. Comparison of two temperature differencing methods to estimate daily evapotranspiration over a Mediterranean vineyard watershed from ASTER data. *Remote Sens. Environ.* **2011**, *115*, 1326–1340. [[CrossRef](#)]
403. Anderson, M.C.; Allen, R.G.; Morse, A.; Kustas, W.P. Use of Landsat thermal imagery in monitoring evapotranspiration and managing water resources. *Remote Sens. Environ.* **2012**, *122*, 50–65. [[CrossRef](#)]
404. Dold, C.; Heitman, J.; Giese, G.; Howard, A.; Havlin, J.; Sauer, T. Upscaling Evapotranspiration with Parsimonious Models in a North Carolina Vineyard. *Agronomy* **2019**, *9*, 152. [[CrossRef](#)]
405. Parastatidis, D.; Mitraka, Z.; Chrysoulakis, N.; Abrams, M. Online Global Land Surface Temperature Estimation from Landsat. *Remote Sens.* **2017**, *9*, 1208. [[CrossRef](#)]
406. GLCF; GSFC. *Landsat Surface Reflectance, Landsat TM & ETM+*; Global Land Cover Facility, University of Maryland: College Park, MD, USA, 2011.
407. Liang, S.; Zhang, X. *Global Land Surface Products: Shortwave Radiation Product Data Collection (2008–2010)*; Beijing Normal University: Beijing, China, 2012. [[CrossRef](#)]
408. Kissling, W.D.; Walls, R.; Bowser, A.; Jones, M.O.; Kattge, J.; Agosti, D.; Amengual, J.; Basset, A.; van Bodegom, P.M.; Cornelissen, J.H.C.; et al. Towards global data products of Essential Biodiversity Variables (EBVs) on species traits. *Nat. Ecol. Evol.* **2018**, *2*, 1531–1540. [[CrossRef](#)] [[PubMed](#)]
409. Lausch, A.; Schmidt, A.; Tischendorf, L. Data mining and linked open data—New perspectives for data analysis in environmental research. *Ecol. Model.* **2015**, *295*, 5–17. [[CrossRef](#)]
410. Bereta, K.; Koubarakis, M.; Pantazi, D.A.; Stamoulis, G.; Caumont, H.; Daniels, U.; Dirk, D.; Ubels, S.; Venus, V.; Wahyudi, F. Providing Satellite Data to Mobile Developers Using Semantic Technologies and Linked Data. In Proceedings of the ICSC 2019: IEEE International Conference on Semantic Computing, Newport Beach, CA, USA, 30 January–1 February 2019; pp. 348–351.
411. Haase, P.; Tonkin, J.D.; Stoll, S.; Burkhard, B.; Frenzel, M.; Geijzendorffer, I.R.; Häuser, C.; Klotz, S.; Kühn, I.; McDowell, W.H.; et al. The next generation of site-based long-term ecological monitoring: Linking essential biodiversity variables and ecosystem integrity. *Sci. Total Environ.* **2018**, *613–614*, 1376–1384. [[CrossRef](#)]

